

| 寄 | 贈  |
|---|----|
| 白 | 平成 |
| 形 | 年  |
| 政 | 月  |
| 司 | 日  |
| 氏 |    |

DA

990

1991

(H)

Charge Asymmetry in b-Quark Production  
at CM Energies between 55 and 64 GeV  
in  $e^+e^-$  Annihilation

Masashi Shirakata

Institute of Applied Physics, Tsukuba University

Tsukuba, Ibaraki 305, Japan

December 1991

*Dedicated to the other three kings...*

## Acknowledgement

This thesis was written through the kindness of many people, all of whom must receive my thanks. The successful construction and operation of the experiment is owed to the dedicated effort of all the members of the VENUS collaboration and TRISTAN accelerator group.

I would like to thank my thesis adviser, Professor Yuzo Asano and also Professor Shigeki Mori who taught me interests in high energy physics and gave me this great chance of the TRISTAN experiment.

I would like to thank Professor Fumihiko Takasaki for his useful and kind advice during my entire work at KEK. I wish to thank Dr. Jun-ichi Kanzaki and Dr. Toru Tsuboyama for their useful discussions and suggestions in the analysis of hadronic events. Without them, I could not complete my thesis work. Their assistance, guidance and encouragement concerning the theoretical consideration have always been of great help to me. I would like to acknowledge them from my heart.

I express my gratitude to my fellows at the University, in particular to Dr. Tadashi Koseki and Mr. Makoto Hatanaka for a number of helpful discussions.

Finally, I would like to thank all of my friends for their support and kindness.

## Abstract

The Standard Model predicts measurable electroweak effects at the TRISTAN energy region. Though the direct contribution from weak interaction is still very small, the interference between electromagnetic and weak interactions sufficiently changes the angular distribution of fermion-pair production reaction such as quark-pair production. The cross section and the charge asymmetry of  $b$ -quark pair production has been measured in  $e^+e^-$  annihilations at the center-of-mass energies between 54.0 and 64.0 GeV using the VENUS detector at TRISTAN. The data sample used in this analysis corresponds to an integrated luminosity of  $60.8 \text{ pb}^{-1}$ . The average center-of-mass energy is 58.4 GeV. In order to tag the  $b$ -quark pair production events, muons were identified.

The results obtained in this thesis are:

$$\begin{aligned} R_b &= 0.78 \pm 0.14(\text{stat.}) \pm 0.11(\text{sys.}) \\ A_b &= -0.50 \pm 0.18(\text{stat.}) \pm 0.11(\text{sys.}) \end{aligned}$$

These are consistent with the predictions of the standard electroweak theory, namely 0.58 for the  $R$ -ratio and  $-0.59$  for the charge asymmetry with the assignment of the iso-spin doublet of the third quark generation.

The most probable values for the mixing parameters of  $B^0$ - $\overline{B}^0$  oscillation are fitted to be

$$\begin{aligned} \chi_d &= 0.167 \pm 0.033 \\ \chi_s &= 0.41 \pm 0.27 \\ \chi &= f_d \chi_d + f_s \chi_s = 0.12 \pm 0.03 \end{aligned}$$

where  $f_d = 0.43$  and  $f_s = 0.13$ .  $\chi_d + 0.3\chi_s = 0.159$ , namely a correlation coefficient of 0.159 between  $\chi_d$  and  $\chi_s$ . The results for the parameter  $\chi_s$  give the experimental confirmation of non-zero  $B_s^0$  mixing. The zero  $B_s^0$  mixing could be excluded with 1.5 standard deviations. The measured asymmetry is corrected by using the above results to be  $A_b = -0.66 \pm 0.28$  where the statistical and systematic errors are summed quadratically. This result is still consistent with the prediction of the standard electroweak theory.

# Contents

|          |  |           |
|----------|--|-----------|
| <b>1</b> | <b>Introduction</b>                              | <b>1</b>  |
| 1.1      | Standard Model . . . . .                         | 1         |
| 1.1.1    | Electroweak theory . . . . .                     | 1         |
| 1.1.2    | Quantum chromodynamics . . . . .                 | 3         |
| 1.2      | History of the Theory and Experiments . . . . .  | 4         |
| 1.3      | Standard Model Today . . . . .                   | 5         |
| <b>2</b> | <b>Forward-Backward Asymmetry</b>                | <b>7</b>  |
| 2.1      | Quark-pair Production . . . . .                  | 7         |
| 2.2      | Mechanism of Inclusive Muon Production . . . . . | 10        |
| 2.3      | Radiative Correction . . . . .                   | 13        |
| 2.4      | $B^0$ - $\overline{B}^0$ Mixing . . . . .        | 15        |
| <b>3</b> | <b>Experimental Apparatus</b>                    | <b>19</b> |
| 3.1      | TRISTAN . . . . .                                | 19        |
| 3.1.1    | Injectors . . . . .                              | 19        |
| 3.1.2    | Accumulation ring . . . . .                      | 21        |
| 3.1.3    | Main ring . . . . .                              | 21        |
| 3.2      | VENUS Detector . . . . .                         | 22        |
| 3.2.1    | Central drift chamber . . . . .                  | 24        |
| 3.2.2    | Barrel lead glass calorimeter . . . . .          | 26        |
| 3.2.3    | End-cap liquid argon calorimeter . . . . .       | 29        |
| 3.2.4    | Barrel muon detector . . . . .                   | 30        |
| 3.2.5    | Other detector components . . . . .              | 33        |
| 3.3      | Event Trigger . . . . .                          | 34        |
| 3.4      | Data Acquisition System . . . . .                | 36        |
| <b>4</b> | <b>Multihadronic Final States</b>                | <b>37</b> |
| 4.1      | Event Reconstruction . . . . .                   | 37        |
| 4.1.1    | CDC track reconstruction . . . . .               | 37        |
| 4.1.2    | LG clustering . . . . .                          | 38        |

|       |   |    |
|-------|---|----|
| 4.1.3 | LA clustering . . . . .   | 40 |
| 4.2   | Data Reduction . . . . .  | 40 |
| 4.2.1 | Process 1 . . . . .   | 41 |
| 4.2.2 | Process 2 . . . . .   | 42 |
| 4.2.3 | Multi-hadronic event selection . . . . .                              | 43 |
| 5     | Monte Carlo Simulation . . . . .                                      | 47 |
| 5.1   | Event Generation . . . . .  | 47 |
| 5.2   | Full Detector Simulator VMONT . . . . .                               | 50 |
| 5.3   | Fast Simulator VITMIN . . . . .                                       | 52 |
| 6     | Muon Identification . . . . .   | 55 |
| 6.1   | Identification Procedure . . . . .                                    | 55 |
| 6.1.1 | CDC track extrapolation . . . . .                                     | 55 |
| 6.1.2 | Local tracking . . . . .  | 57 |
| 6.2   | Efficiency and Backgrounds . . . . .                                  | 60 |
| 6.2.1 | Detection efficiency of an isolated muon . . . . .                    | 60 |
| 6.2.2 | Efficiency for muon identification in multi-hadronic events . . . . . | 63 |
| 7     | Procedure of Measurements . . . . .                                   | 65 |
| 7.1   | Jet Reconstruction . . . . .  | 65 |
| 7.2   | $b\bar{b}$ Pair Production Enhancement . . . . .                      | 71 |
| 7.3   | Differential Cross Section . . . . .                                  | 75 |
| 7.4   | Results and Errors . . . . .  | 78 |
| 7.4.1 | Fitting procedure . . . . .   | 78 |
| 7.4.2 | Systematic errors . . . . .   | 79 |
| 8     | $B^0$ - $\overline{B}^0$ Oscillations . . . . .                       | 83 |
| 8.1   | Compilation of Heavy Quark Asymmetries . . . . .                      | 83 |
| 8.2   | Average Mixing Parameter . . . . .                                    | 85 |
| 9     | Conclusion . . . . .  | 89 |

# List of Tables

|     |  |    |
|-----|--|----|
| 1.1 | Characteristics of leptons, quarks and the minimal Higgs. . . . .  | 2  |
| 2.1 | Parameters of the Standard Model. . . . .  | 10 |
| 4.1 | List of events triggered and survived from each selection stage. . . .                                       | 45 |
| 5.1 | Parameter-sets for the JETSET version 6.3. . . . .   | 52 |
| 6.1 | Typical value of extrapolated deviation (cm) due to multiple coulomb<br>scattering. . . . .                  | 56 |
| 6.2 | Typical value of the weight at the local track reconstruction $\sigma_{lo}$ (cm). .                          | 57 |
| 6.3 | Muon selection without the muon detector. . . . .  | 61 |
| 7.1 | List of events survived from the $p_t$ cut. . . . .  | 73 |
| 7.2 | Measured differential cross section for $e^+e^- \rightarrow b\bar{b}$ . . . . .                              | 78 |
| 7.3 | Summary of systematic errors. . . . .  | 80 |
| 7.4 | List of measured $R_b$ and $A_b$ with the various $p_t$ -cut. . . . .  | 81 |
| 8.1 | Measurements of the $b$ -quark asymmetry at PEP, PETRA, TRIS-<br>TAN and LEP. . . . .                        | 84 |
| 8.2 | Measurements of the $b$ -quark asymmetry at PEP, PETRA, TRIS-<br>TAN and LEP with mixing correction. . . . . | 85 |
| 8.3 | Mixing parameters of the $B^0$ - $\overline{B}^0$ oscillation. . . . .                                       | 87 |





# List of Figures

|      |  |    |
|------|--|----|
| 2.1  | Lowest order Feynman diagrams for fermion-pair production; (a) a virtual $\gamma$ exchange and (b) a virtual $Z^0$ exchange. . . . . | 8  |
| 2.2  | Theoretical prediction of $R_f$ and $A_f$ . . . . .  | 11 |
| 2.3  | Diagram of weak charged current decay of a heavy quark in the spectator model. . . . .   | 12 |
| 2.4  | One-loop diagrams of the electroweak interaction; (a) vacuum polarizations, (b) vertex corrections and (c) box diagrams. . . . .     | 14 |
| 2.5  | Photon emission diagrams of the electroweak interaction. . . . .   | 15 |
| 2.6  | Box diagrams for $B^0$ - $\overline{B}^0$ mixing. . . . .  | 17 |
| 3.1  | Site layout of the TRISTAN. . . . .  | 20 |
| 3.2  | Integrated luminosity per day measured by the VENUS. . . . .   | 22 |
| 3.3  | Overview of the VENUS detector. . . . .  | 23 |
| 3.4  | Central drift chamber; (a) end view of one quadrant and (b) cell geometry. . . . .   | 25 |
| 3.5  | Arrangement of the lead-glass counters. . . . .  | 28 |
| 3.6  | Assembly of a lead-glass counter module. . . . .   | 29 |
| 3.7  | End and side views of the liquid argon calorimeter. . . . .  | 31 |
| 3.8  | Eight-cell drift tube module of the muon detector. . . . .   | 32 |
| 3.9  | Block diagram of the trigger logic. . . . .  | 34 |
| 3.10 | VENUS data acquisition system. . . . .   | 36 |
| 4.1  | Definition of track parameters. . . . .  | 39 |
| 4.2  | Distribution of the total energy deposit of calorimeters. . . . .  | 44 |
| 4.3  | Distribution of the visible longitudinal momentum balance. . . . .   | 46 |
| 5.1  | Flowchart of the analysis procedure. . . . .   | 48 |
| 5.2  | Perturbative QCD correction by a parton shower model. . . . .  | 49 |
| 5.3  | Tree-level QCD diagrams up to second order of $\alpha_s$ . . . . .   | 49 |
| 5.4  | String fragmentation scheme of multi-hadron production. . . . .  | 51 |
| 6.1  | Normalized angular difference. . . . .   | 59 |
| 6.2  | Momentum dependence of the efficiency of the muon identification. . . . .  | 61 |

|      |  |    |
|------|--|----|
| 6.3  | Angular dependence of the efficiency of the muon identification. . .   | 62 |
| 6.4  | A sample of a superimposed event; (a) $\mu$ -pair production event, (b) a multi-hadronic event and (c) a superimposed event. . . . .   | 64 |
| 7.1  | Thrust distribution. . . . .   | 66 |
| 7.2  | Schematic illustration of the thrust. . . . .  | 67 |
| 7.3  | Thrust value vs. the polar angle difference between the thrust axis and quark direction. . . . .   | 67 |
| 7.4  | Polar angle difference between the thrust axis and quark direction.  | 69 |
| 7.5  | Schematic image of the jet-muon combined axis. . . . .   | 70 |
| 7.6  | Opening angle between jets. . . . .  | 71 |
| 7.7  | Polar angle difference with respect to the quark direction; the solid histogram for the thrust axis method and the dashed histogram for the jet-muon combined axis method. . . . .   | 72 |
| 7.8  | Transverse momentum of the muon candidates; (a) with respect to the thrust axis and (b) with respect to the combined axis. Shaded, cross-hatched, hatched and open histograms correspond to Monte Carlo calculations for $b \rightarrow \mu$ , $b \rightarrow c \rightarrow \mu$ , $c \rightarrow \mu$ and decay and punchthrough backgrounds, respectively. . . . . | 74 |
| 7.9  | $p_t$ -cut dependence of the prompt muon ratio and the track acceptance.   | 75 |
| 7.10 | Angular distribution of the thrust axis. Shaded, cross-hatched, hatched and open histograms correspond to Monte Carlo calculations for $b \rightarrow \mu$ , $b \rightarrow c \rightarrow \mu$ , $c \rightarrow \mu$ and decay and punchthrough backgrounds, respectively. . . . .   | 76 |
| 7.11 | Correction factor of the differential cross section for $e^+e^- \rightarrow b\bar{b}$ . . .  | 77 |
| 7.12 | Measured differential cross section for $e^+e^- \rightarrow b\bar{b}$ . . . . .  | 79 |
| 8.1  | Measurements of the $b$ -quark asymmetry at PEP, PETRA, TRISTAN and LEP; (a) without $B^0$ - $\bar{B}^0$ mixing and (b) with $B^0$ - $\bar{B}^0$ mixing.   | 86 |
| 8.2  | Mixing parameters in the $\chi_s - \chi_d$ plane. Dotted curves are the central value and the dashed and solid curves represent the 69 % and 80 % C.L. contours, respectively. . . . .   | 88 |

# Chapter 1

## Introduction

Elementary particle physics has been playing an important role in the search for fundamental constituents of matter. We can now understand the structure of matter as composites of a set of simple and fundamental particles governed by four types of interactions: the electromagnetic, strong, weak and gravitational interactions. The current theoretical picture of physics which is often referred to as the Standard Model, successfully describes interactions between elementary particles in the wide range of energy from  $10^6$  eV to  $10^{11}$  eV. The standard theory has, however, not become a complete theory yet. Namely, it has not completely unified all the interactions in nature and it cannot predict the masses of elementary particles. The standard theory needs further experimental confirmations.

### 1.1 Standard Model

Gauge symmetry is now believed to be a fundamental guiding principle to determine the form of particle interactions. The strong, weak and electromagnetic forces are embedded in an  $SU(3) \times SU(2) \times U(1)$  gauge group. The fundamental constituent particles are supposed to be point-like fermions and there are two types of fermions: leptons and quarks. This theory contains the electroweak theory and QCD<sup>1</sup>[1], both of which are based on the principle of local gauge invariance. The electroweak theory unifies the electromagnetic and weak interactions while QCD describes the strong interaction.

#### 1.1.1 Electroweak theory

Matter consists of point-like spin 1/2 fermions: leptons, quarks and their anti-particles in the electroweak theory. Left-handed fermions transform as doublets

---

<sup>1</sup>Quantum Chromodynamics

|       | lepton |         |         | quark |       |       |       | Higgs    |          |
|-------|--------|---------|---------|-------|-------|-------|-------|----------|----------|
|       | $\nu$  | $l_L^-$ | $l_R^-$ | $u_L$ | $d_L$ | $u_R$ | $d_R$ | $\phi^+$ | $\phi^0$ |
| $T$   | 1/2    | 1/2     | 0       | 1/2   | 1/2   | 0     | 0     | 1/2      | 1/2      |
| $T_3$ | 1/2    | -1/2    | 0       | 1/2   | -1/2  | 0     | 0     | 1/2      | -1/2     |
| $Q$   | 0      | -1      | -1      | 2/3   | -1/3  | 2/3   | -1/3  | 1        | 0        |
| $Y$   | -1     | -1      | -2      | 1/3   | 1/3   | 4/3   | -2/3  | 0        | 1        |

Table 1.1: *Characteristics of leptons, quarks and the minimal Higgs.*

and right-handed ones are singlets under SU(2) symmetry on weak isospin;  $T = (T_1, T_2, T_3)$ . The  $T_3$  eigenstates are expressed as follows:

$$\text{leptons : } l_L = \begin{pmatrix} \nu \\ l_L^- \end{pmatrix}_L, l_R^- \quad \text{quarks : } q_L = \begin{pmatrix} u \\ d_L \end{pmatrix}_L, u_R, d_R \quad (1.1)$$

where the indices  $L$  and  $R$  denote helicity states, namely left-handed and right-handed.  $\nu$  is a neutrino,  $l^-$  is a charged lepton, and  $u$  and  $d$  are the up-type and down-type quarks, respectively. These fermion states in the multiplets share the same weak-hypercharge  $Y$  which is the eigenvalue of the quantum state of the U(1) symmetry.  $T_3$  and  $Y$  are related to the electric charge  $Q$  through the equation,  $Q = T_3 + Y/2$ . In addition to the fermions, scalar bosons which are called Higgs particles are introduced as a complex isodoublet in SU(2)<sub>L</sub> in the minimal Standard Model. The characteristics of leptons, quarks and Higgs particles are summarized in Table 1.1 in the context of the standard electroweak theory.

Spin 1 bosons which correspond to the generators of the symmetry group are called gauge bosons. The introduction of the Higgs mechanism causes the so-called spontaneous break-down of the original SU(2)<sub>L</sub>  $\times$  U(1) symmetry and makes the gauge bosons and fermions massive. Another U(1) symmetry with a generator  $Q$  arises after the symmetry breaking. A well established theory called QED<sup>2</sup>[2] is constructed with a massless gauge boson which is called a photon or  $\gamma$ . Three massive gauge bosons, charged weak bosons  $W^\pm$  and a neutral weak boson  $Z^0$ , mediate the weak interaction. In the simplest Higgs mechanism there is only one neutral Higgs boson  $H^0$  which physically remains after the spontaneous symmetry breaking. However, the masses of the fermions and  $H^0$  are left as unknown parameters. Besides, there are three independent parameters which determine the strengths of the electroweak interactions. They are usually chosen to be the fine

---

<sup>2</sup>Quantum Electrodynamics

structure constant  $\alpha$ , weak mixing angle  $\theta_W$  and either  $Z^0$  mass  $M_Z$ [3] or Fermi constant  $G_F$ .

Leptons and quarks have several species. As for the mass eigenstates, flavours are classified in ascending order of mass as follows:

$$\text{leptons : } \begin{pmatrix} \nu_1 \\ e^- \end{pmatrix} \begin{pmatrix} \nu_2 \\ \mu^- \end{pmatrix} \begin{pmatrix} \nu_3 \\ \tau^- \end{pmatrix} \quad \text{quarks : } \begin{pmatrix} u \\ d \end{pmatrix} \begin{pmatrix} c \\ s \end{pmatrix} \begin{pmatrix} t \\ b \end{pmatrix} \quad (1.2)$$

These groups with a repetitive structure are called generations. The corresponding particle in a different generation has the same quantum numbers. In general, mass eigenstates do not always coincide with gauge eigenstates because masses are not given by the gauge interaction but by ad hoc Yukawa interactions with the Higgs particle. Assuming all neutrinos to be massless, any neutrino state can be a mass eigenstate. Therefore,  $\nu_1$ ,  $\nu_2$  and  $\nu_3$  are usually replaced by the gauge weak eigenstates  $\nu_e$ ,  $\nu_\mu$  and  $\nu_\tau$  and the different lepton generations are completely decoupled. On the other hand, all quarks are massive and actually there is a small mixing between the quark generations in the weak interaction, which is represented by a unitary, Kobayashi-Maskawa matrix[4]  $V$  as follows:

$$\begin{pmatrix} d_c \\ s_c \\ b_c \end{pmatrix} = \begin{pmatrix} V_{ud} & V_{us} & V_{ub} \\ V_{cd} & V_{cs} & V_{cb} \\ V_{td} & V_{ts} & V_{tb} \end{pmatrix} \begin{pmatrix} d \\ s \\ b \end{pmatrix} \quad (1.3)$$

where the subscript  $c$  denotes the Kobayashi-Maskawa mixed quark states of quark mass eigenstates which are generalized Cabbibo mixing.  $d_c$ ,  $s_c$  and  $b_c$  are the weak eigenstates coupled to  $u$ ,  $c$  and  $t$ , respectively. The Kobayashi-Maskawa matrix can be determined by three rotational angle parameters and one phase parameter which accounts for  $CP$  violating phenomena. The weak eigenstates are expressed as follows:

$$\text{leptons : } \begin{pmatrix} \nu_e \\ e^- \end{pmatrix} \begin{pmatrix} \nu_\mu \\ \mu^- \end{pmatrix} \begin{pmatrix} \nu_\tau \\ \tau^- \end{pmatrix} \quad \text{quarks : } \begin{pmatrix} u \\ d_c \end{pmatrix} \begin{pmatrix} c \\ s_c \end{pmatrix} \begin{pmatrix} t \\ b_c \end{pmatrix} \quad (1.4)$$

### 1.1.2 Quantum chromodynamics

Quarks are  $SU(3)$  triplets in QCD, that is, each quark has one of three color charges. Of course, each anti-quark has one of three anti-color charges. The eight  $SU(3)$  generators physically correspond to massless gauge bosons: gluons or  $g$ . A gluon possesses a color and an anti-color, mediating the strong interaction between quarks. On account of its non-Abelian nature, gluons also interact with each other and the visible strength of the strong interaction increases according

to the distance. This feature is responsible for the quark-confinement. Quarks and gluons which are often called partons always collapse into hadrons. At short distances, namely at high momentum transfer squared  $q^2$ , the coupling strength becomes so small that a perturbative approach can be made.

## 1.2 History of the Theory and Experiments

Interactions between fundamental particles are described by gauge theories where interactions are mediated by gauge bosons; the photon for the electromagnetic interaction, the gluon for the strong interaction,  $W^\pm$ ,  $Z^0$  for the weak interaction and gravitons for the gravitational force. The oldest gauge theory is the quantum electrodynamics (so-called QED) and it has an important feature of renormalizability. QED is one of the Abelian gauge theories and predicts phenomena under electromagnetic interactions very accurately. A non-Abelian gauge theory was presented by C.N. Yang and Robert L. Mills in 1954. S.L. Glashow, Steven Weinberg and Abdus Salam applied the Yang-Mills gauge theory to the unification of the electromagnetic and weak interactions and it is called the GWS theory[5]. However, in the original Yang-Mills theory, the gauge bosons are treated as massless. The sophisticated Higgs mechanism was introduced to give masses to the bosons through the vacuum expectation value of a Higgs field holding renormalizability of the theory. The unified theory, which is called the electroweak theory, predicted the existence of a weak neutral current mediated by a neutral weak boson:  $Z^0$ . The weak neutral current was actually observed in  $\nu_\mu e$  and  $\nu_\mu p$  scattering in 1973. Its existence provided a strong support for the electroweak theory.

Since both an electron and a positron are point-like particles, the beam energy is effectively utilized in  $e^+e^-$  collisions and the ensuing reactions are simple to understand. As a consequence of such advantages of  $e^+e^-$  colliding experiments, various contributions to particle physics have been made. In 1974,  $\Psi$ -series of the  $c\bar{c}$  bound states with masses of about 3 GeV/ $c^2$  were first observed at SLAC using the  $e^+e^-$  collider SPEAR[6] and the  $c\bar{c}$  state called the  $J$ -particle was discovered at BNL in proton nucleus collision. The discovery of  $c$ -quark completed the second generation. In 1975,  $\tau$ -lepton was discovered also at SPEAR[7]. This was the first observation of a third generation particle. The third member, the down type quark  $b$ , was discovered in 1977 at the proton-nucleon collision experiment[8] at Fermilab. And then,  $\Upsilon$ -series of the  $b\bar{b}$  bound states with masses around 10 GeV/ $c^2$  were clearly resolved in  $e^+e^-$  collisions at DORIS storage ring, DESY and at CESR, Cornell[9]. The center-of-mass energy was increased using the accelerators, PEP at SLAC and PETRA at DESY up to 46.8 GeV. Though the predicted  $t$ -quark was not found, the results showed good agreements with the Standard Model. In the

electroweak theory,  $\sin^2 \theta_W$  was determined by the forward-backward asymmetry of lepton-pair productions[10], combining the results from the neutrino experiments. In a QCD related field, a hard gluon emission was clearly observed as a three-jet event and its cross section agreed well with the perturbative calculation of QCD.

A number of experimental studies using  $e^+e^-$  colliding machines, PEP and PETRA, were carried out to check the validity of the electroweak theory. All the efforts resulted in verifying the theory although only the tail of  $Z^0$  was measured in their low energy region:  $30 \sim 40$  GeV. At last all the weak bosons  $W^\pm$  and  $Z^0$  were discovered at the CERN  $\bar{p}p$  collider in 1983. Thus the GWS electroweak theory seems to be standing on strong bases of experimental results. However, the model has many unpredictable parameters such as masses of Higgs, quarks and leptons, the number of generations, weak mixing angles, and so on. In spite of many successes, this model is considered to be an approximate theory of the more comprehensive theory. So it is important to check the validity of the Standard Model in higher energy region. In 1986, just after PEP and PETRA had finished their operation, TRISTAN in Japan began operation. TRISTAN had been the world highest energy  $e^+e^-$  collider with center-of-mass energies around 60 GeV before SLC at SLAC and LEP at CERN came into their operation. In this energy region, the interference effect between electromagnetic and weak interactions increases to the maximum. SLC and LEP experiments started at the center-of-mass energy around the  $Z^0$  pole ( $\approx 91$  GeV) in summer 1989.

### 1.3 Standard Model Today

The status of the Standard Model is summarized as follows. The electroweak theory which has 17 parameters to be measured seems quite successful. There is no evidence which contradicts the theory though there are two missing members:  $t$ -quark and Higgs boson  $H^0$ . As for the strong interaction, a perturbative approach of QCD successfully explains many phenomena at high energies. But the strong interaction in low  $q^2$  region such as the jet-formation mechanism and the mass-spectrum of hadrons have not been clearly understood. Moreover, there remain some problems which cannot be explained by the present theory. For example, the origin and the number of generations cannot be given theoretically. The theory seems to be far from the ultimate theory, rather a well established phenomenology.

In this thesis, the Standard Model is tested by measuring the forward-backward asymmetry in the heavy quark production process. It gives a very good check of the model because of its clearness and its sensitivity to the electroweak parameters.





# Chapter 2

## Forward-Backward Asymmetry

The Standard Model predicts measurable electroweak effects at TRISTAN energy region. Though the direct contribution from weak interaction is still very small, an interference between electromagnetic and weak interactions sufficiently changes the angular distribution of fermion-pair production reaction such as quark-pair production. In this chapter, the formalism of the Standard Model is given and the results of the theoretical calculation based on the lowest order Feynman diagrams are presented.

### 2.1 Quark-pair Production

The process of a fermion-pair production is mediated by a virtual photon ( $\gamma$ ) and a virtual neutral weak boson ( $Z^0$ ) and only the s-channel reaction is possible except for the Bhabha scattering in  $e^+e^-$  annihilation as shown in Fig. 2.1 because of the lepton or baryon number conservation. The weak neutral current is a mixture of vector and axial-vector current. So the Lagrangian for this process in the standard electroweak theory is written as follows:

$$\mathcal{L}_{f\bar{f}} = ieq_f \bar{u}_f \gamma^\mu u_f A_\mu + i \frac{g}{4 \cos \theta_W} \bar{u}_f \gamma^\mu (v_f - a_f \gamma^5) u_f Z_\mu^0 \quad (2.1)$$

where suffix  $f$  denotes the type of pair-created fermions and  $u_f$  denotes the Dirac spinor.  $A_\mu$  and  $Z_\mu^0$  are the fields of photon and weak neutral boson, respectively.  $e$  and  $g$  are the electromagnetic and weak coupling constants.  $q_f$  is the electric charge of the fermion in units of  $e$ .  $v_f$  and  $a_f$  are the dimensionless vector and axial-vector coupling constants. The first term in the Lagrangian corresponds to the electromagnetic interaction and the second to the weak interaction. The coupling constants  $e$  and  $g$  are related to each other by the weak mixing angle  $\theta_W$ .

$$e = g \sin \theta_W \quad (2.2)$$

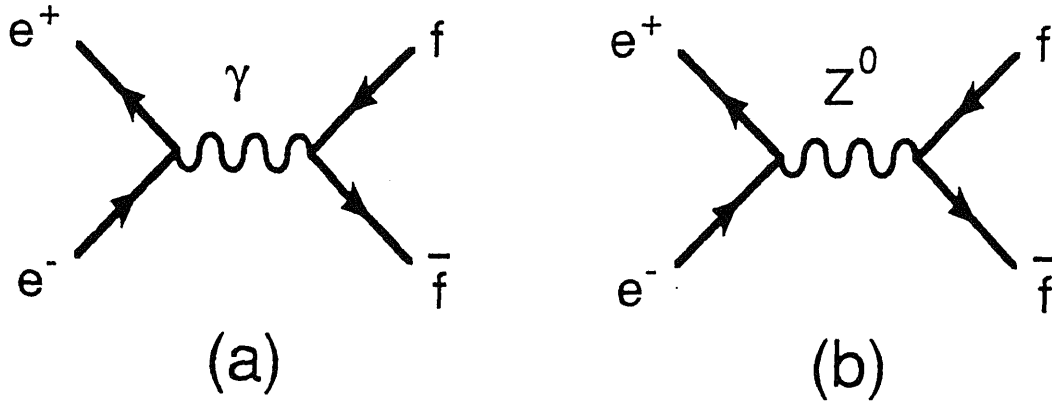


Figure 2.1: Lowest order Feynman diagrams for fermion-pair production; (a) a virtual  $\gamma$  exchange and (b) a virtual  $Z^0$  exchange.

In the QED, a virtual photon mediates the electromagnetic interaction between charged fermions as shown in Fig. 2.1(a). The lowest order differential cross section of a quark-pair production is written as:

$$\frac{d\sigma_0^{QED}}{d\Omega} = 3 \frac{\alpha^2}{4s} \frac{\beta(3 - \beta^2)}{2} [1 + \cos^2 \theta + (1 - \beta^2) \sin^2 \theta] Q_f^2 \quad (2.3)$$

where  $\beta = \sqrt{1 - 4m^2/s}$ ,  $m$  is the mass of the quark,  $s$  is the square of the center-of-mass energy,  $\alpha$  is the fine structure constant  $e^2/4\pi$  ( $\approx 1/137$ ),  $Q_f$  is the electric charge and  $\theta$  is the angle between the direction of an incident electron and that of an outgoing negative-charge quark state. The cross section is multiplied by a factor three due to the color charge degrees of freedom of the quark. The contribution from the higher order QCD processes such as the effect of gluon emissions should be taken into account. In the TRISTAN energy region which is around 5S GeV, the QCD correction increases the total cross section by approximately 5 %. An event from a quark-pair production often forms a two-jet structure where two clusters of hadrons are ejected in opposite direction. Hard gluon emissions result in a multi-jet event. Fragmentation mechanism of hadrons which explains the jet-formation is not completely resolved but there are some phenomenological models to describe this.

This differential cross section is averaged over the spins of the initial state particles and summed over the spins of the final state particles since the electron and positron beams which are dealt with in this thesis are not polarized. Therefore,

the cross section has no azimuthal angular dependence. Under the condition  $\sqrt{s} \sim 58$  GeV,  $\beta$  is almost equal to unity. The differential cross section becomes

$$\frac{d\sigma_0^{QED}}{dz} = 3 \frac{\pi\alpha^2}{2s} (1 + z^2) \quad (2.4)$$

where  $z = \cos \theta$ . This equation shows that the lowest order QED differential cross section is symmetric under the exchange  $\theta \leftrightarrow \pi - \theta$ .

In electroweak interactions, a process of a quark-pair production is mediated also by a virtual  $Z^0$  as shown in Fig. 2.1(b) in addition to a virtual photon. The differential cross section has to be modified to

$$\begin{aligned} \frac{d\sigma_0^{GWS}}{d\Omega} = & 3 \frac{\alpha^2}{4s} \frac{\beta(3 - \beta^2)}{2} \left[ Q_f^2 f_{(\theta)} - 2Q_f \chi_1 \{ v v_f f_{(\theta)} \} \right. \\ & + \chi_2 \{ v_f^2 (1 + v^2) f_{(\theta)} + \beta^2 a_f^2 (1 + v^2) [1 + \cos^2 \theta] \\ & \left. - 8\beta v v_f a_f \cos \theta \} \right] \end{aligned} \quad (2.5)$$

$$f_{(\theta)} = [1 + \cos^2 \theta + (1 - \beta^2) \sin^2 \theta] \quad (2.6)$$

$$\chi_1 = \frac{1}{16 \sin^2 \theta_W \cos^2 \theta_W} \frac{s(s - M_Z^2)}{(s - M_Z^2)^2 + \Gamma_Z^2 M_Z^2} \quad (2.7)$$

$$\chi_2 = \frac{1}{256 \sin^4 \theta_W \cos^4 \theta_W} \frac{s^2}{(s - M_Z^2)^2 + \Gamma_Z^2 M_Z^2} \quad (2.8)$$

where  $M_Z$  and  $\Gamma_Z$  is the mass and the decay width of the  $Z^0$  boson, respectively, and the subscript  $f$  refers to the quark of interest. The Standard Model predicts the values of  $v$ ,  $v_f$  and  $a_f$  as follows:

$$v = -1 + 4 \sin^2 \theta_W \quad (2.9)$$

$$a_f = 2T_{3f} \quad (2.10)$$

$$v_f = 2T_{3f} - 4Q_f \sin^2 \theta_W \quad (2.11)$$

$$T_{3f} = +\frac{1}{2} : \quad f = \nu_e, \nu_\mu, \nu_\tau, u, c, t \quad (2.12)$$

$$T_{3f} = -\frac{1}{2} : \quad f = e^-, \mu^-, \tau^-, d, s, b \quad (2.13)$$

The electroweak mixing angle  $\theta_W$  is given by the ratio of masses of weak bosons.

$$\sin^2 \theta_W = 1 - \frac{M_W^2}{M_Z^2} \quad (2.14)$$

Under the condition of  $\beta = 1$ , the cross section becomes

$$\frac{d\sigma_0^{GWS}}{dz} = \frac{\pi\alpha^2}{2s} R_f \left( 1 + z^2 + \frac{8}{3} A_f z \right) \quad (2.15)$$

| Parameter         |  |
|-------------------|--|
| $G_F$             | $1.16637 \times 10^{-5}$               |
| $\sin^2 \theta_W$ | 0.231                                  |
| $m_b$             | 5.0 (GeV/c <sup>2</sup> )              |
| $M_Z$             | $91.16 \pm 0.03$ (GeV/c <sup>2</sup> ) |
| $\Gamma_Z$        | 2.5 (GeV/c <sup>2</sup> )              |
| $\Lambda_{QCD}$   | 0.16 (GeV)                             |

Table 2.1: *Parameters of the Standard Model.*

$$R_f = 3 \left[ Q_f^2 - 2Q_f \chi_1 v v_f + \chi_2 (1 + v^2) (v_f^2 + a_f^2) \right] \quad (2.16)$$

$$A_f = 3 \left[ \frac{3}{2} a_f (Q_f \chi_1 - 2\chi_2 v v_f) / R_f \right] \quad (2.17)$$

$R_f$  and  $A_f$  are called  $R$ -ratio and forward-backward charge asymmetry, respectively. They can be calculated from the differential cross section as follows:

$$R_f = \frac{\sigma_0^{GWS}}{\sigma_0^{QED}} \quad (2.18)$$

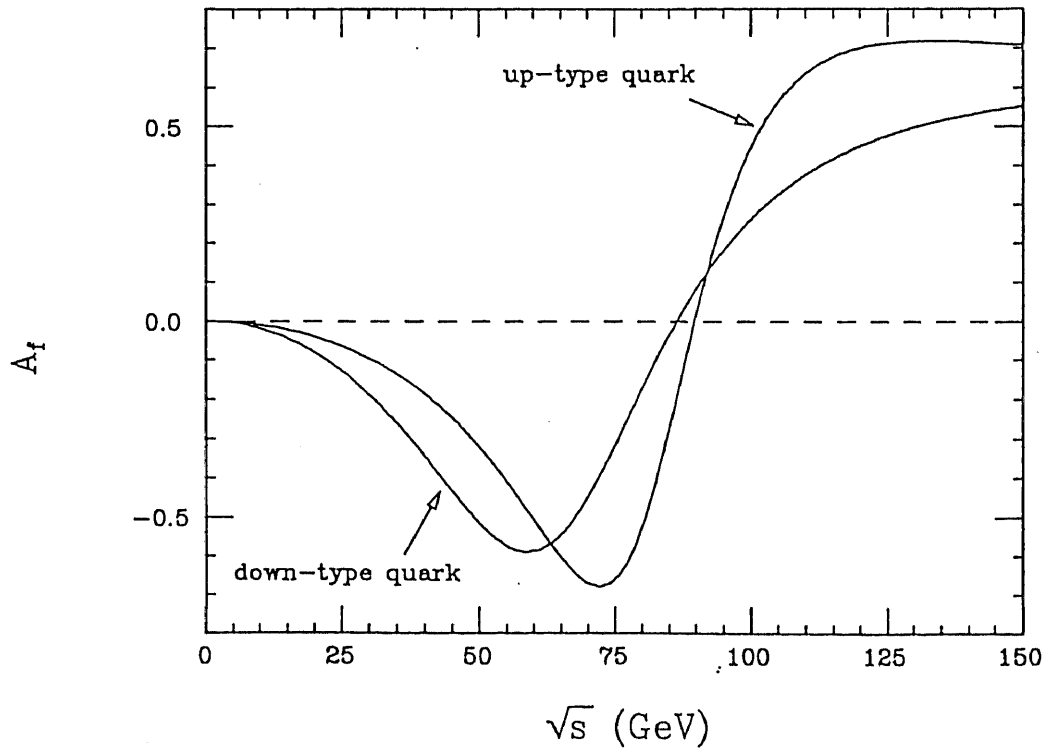
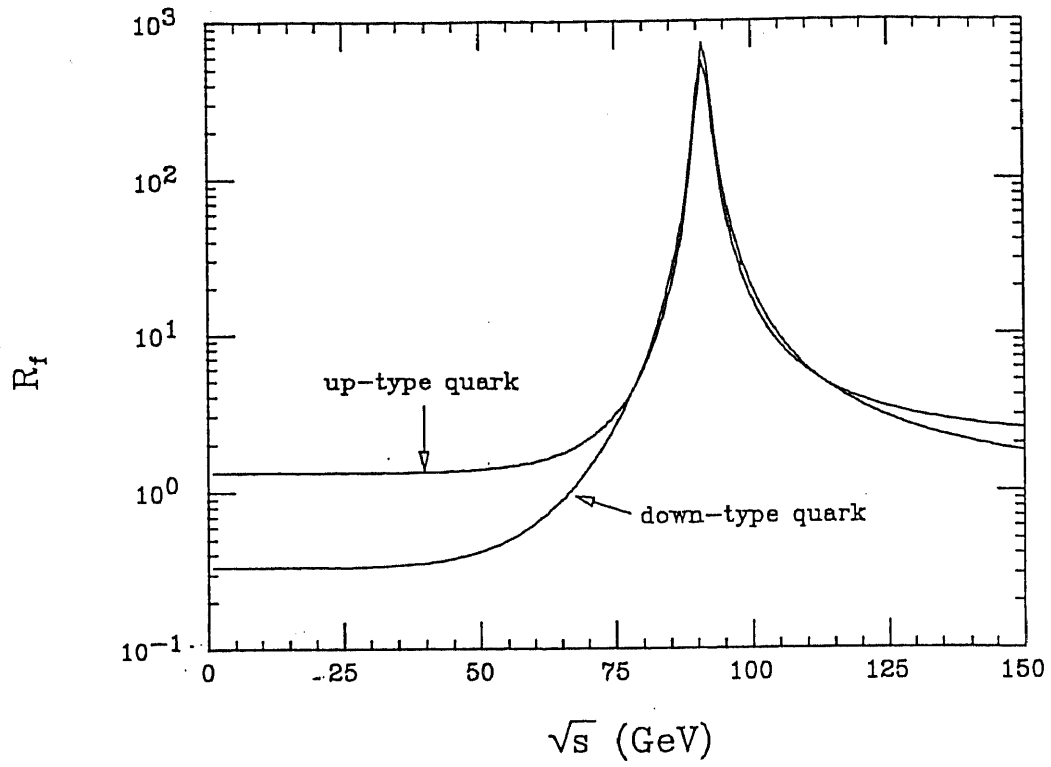
$$A_f = \frac{1}{\sigma_0^{GWS}} \left( \int_0^1 \frac{d\sigma_0^{GWS}}{dz} dz - \int_{-1}^0 \frac{d\sigma_0^{GWS}}{dz} dz \right) \quad (2.19)$$

Without weak contribution,  $R_f$  becomes 1/3 for the up-type quark and 4/3 for the down-type quark. Deviations of  $R_f$  from these values and of  $A_f$  from 0 indicate the effect of the weak neutral current. The effect is more apparent in  $A_f$  than in  $R_f$  since the interfering term in equation 2.16 is suppressed because of the smallness of vector coupling constants. The parameters of the GWS theory are listed in Table 2.1 and in Fig. 2.2, theoretical predictions of  $R_f$  and  $A_f$  are shown as a function of  $\sqrt{s}$ . The theory predicts the values of  $R_b$  and  $A_b$  to be respectively 0.58 and  $-0.59$  at  $\sqrt{s} = 58.4$  GeV. These values can be compared with the experimental observations for testing the Standard Model.

## 2.2 Mechanism of Inclusive Muon Production

A heavy quark such as  $c$  and  $b$  can decay to a lighter quark through the weak charged current which is called the semi-leptonic decay. The total decay rate of  $b$ -quark can be separated into the semi-leptonic part and hadronic part. When the gluon emission is ignored, the semi-leptonic decay rate of  $b$ -quark is given by

$$\Gamma(b \rightarrow q l \nu_l) = \frac{G_F^2 m_b^5}{192\pi^3} |V_{qb}|^2 I(\epsilon) \quad (2.20)$$

Figure 2.2: Theoretical prediction of  $R_f$  and  $A_f$ .

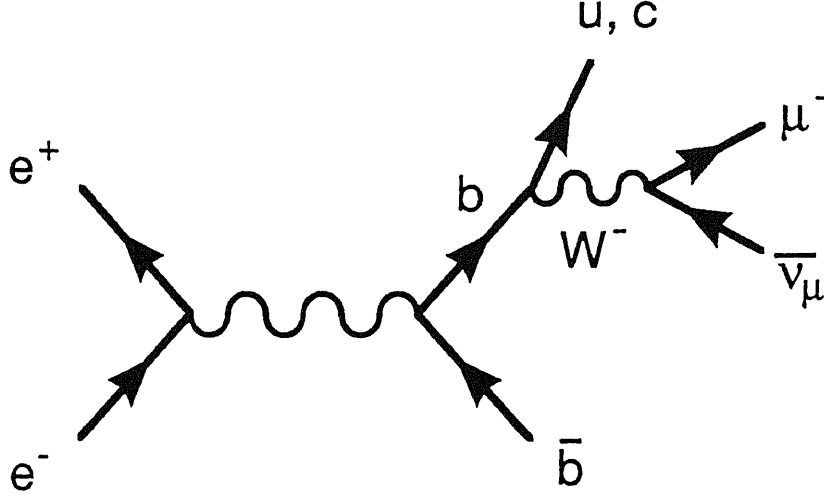


Figure 2.3: Diagram of weak charged current decay of a heavy quark in the spectator model.

where  $V_{qb}$  is the Kobayashi-Maskawa matrix element and  $I(\epsilon)$  is the phase factor.

$$I(\epsilon) = 1 - 8\epsilon^2 + \epsilon^6 + \epsilon^8 - 24n\epsilon \quad (2.21)$$

where  $\epsilon \equiv m_q/m_b$ . The factor  $I(\epsilon)$  is close to unity for the  $b \rightarrow u$  transition while it is about 0.5 for the  $b \rightarrow c$  transition in which  $\epsilon \sim 0.3$ .

Neglecting spin polarizations and all the decay product masses, the width for a weak charged current decay of a fermion into three fermions  $f \rightarrow gf'g'$  is calculated as follows:

$$d\Gamma_f = |V_{fg}|^2 |V_{f'g'}|^2 G_F^2 \frac{m_f}{E_f} (2\pi)^{-5} \\ 64(p_f \cdot p_{g'}) (p_g \cdot p_{f'}) \frac{d^3 p_g}{2E_g} \frac{d^3 p_{f'}}{2E_{f'}} \frac{d^3 p_{g'}}{2E_{g'}} \delta^4(p_f - p_g - p_{f'} - p_{g'}) \quad (2.22)$$

where  $p_f, p_g, p_{f'}$  and  $p_{g'}$  denote four momenta of the fermions and  $f'$  has the same  $T_3$  value as that of  $f$  while  $g$  and  $g'$  have the flipped  $T_3$  value. The weak charged current decay of a heavy flavoured hadron is well approximated by the spectator model as shown in Fig. 2.3. The accompanying light quark in the hadron, so-called a spectator quark, is considered to be irrelevant to decay.

The decay rate of the hadronic part is simply three times that of the semi-leptonic part. The factor three comes from the color charge of the quark. Considering the possible lepton and quark combinations from the  $W$  decay, the decay rate ratio for the  $b \rightarrow q$  transition is roughly estimated as follows:

$$e\nu_e : \mu\nu_\mu : \tau\nu_\tau : \bar{u}d : \bar{c}s = 1 : 1 : 1 : 3 : 3 \quad (2.23)$$

And assuming  $|V_{ub}|^2/|V_{cb}|^2 \approx 0$

$$Br(b \rightarrow c\mu^-\bar{\nu}_\mu) = \frac{\Gamma_{\mu\nu_\mu}}{\Gamma_{ud} + \Gamma_{cs} + \Gamma_{e\nu_e} + \Gamma_{\mu\nu_\mu} + \Gamma_{\tau\nu_\tau}} \frac{|V_{cb}|^2}{|V_{ub}|^2 + |V_{cb}|^2} \approx \frac{1}{9} \quad (2.24)$$

The simple characteristic of  $b$ -quark decay gives a branching ratio of 11 % for the muon.

## 2.3 Radiative Correction

In comparing experimental results with the theoretical predictions or results of other experiments, the values corrected to the lowest order are usually used. The effects of the higher order interaction terms have to be taken into account in order to compare the experimental measurements with the theoretical expectations. This correction is called a radiative correction and cannot be neglected because this effect in the total cross section is expected typically to be a few tens of percent. Since the magnitude of the correction decreases with the order of coupling, the contributions beyond the second order need not to be considered. In practice, it is very difficult to include more complicated diagrams.

As the radiative correction has an angular dependence, the lowest order differential cross section should be modified as

$$\left(\frac{d\sigma}{dz}\right)_{RC} = \left(\frac{d\sigma_{lowest}}{dz}\right) [1 + \delta_{RC}(z)] \quad (2.25)$$

where  $(d\sigma/dz)_{RC}$  is the differential cross section including the higher order terms and  $1 + \delta_{RC}(z)$  is the radiative correction factor with angular dependence. The effects of the higher order terms are mainly due to electroweak one-loop and real photon emission terms, and those of still higher order terms are negligible. One-loop diagrams including vacuum polarizations, vertex corrections and box diagrams are shown in Fig. 2.4. Real photon emission diagrams are shown in Fig. 2.5. In calculating the correction factor, all these electroweak diagrams are taken into account.

The lowest order cross section  $\sigma_0$  should be corrected into the observable cross section  $\sigma$  ignoring the threshold effect due to the mass of the final particle as follows:

$$\sigma = (1 + \delta)\sigma_0 \quad (2.26)$$

$$\delta = \delta_{vacuum} + \delta_{vertex} + \delta_{emission} \quad (2.27)$$

where  $\delta_{vacuum}$ ,  $\delta_{vertex}$  and  $\delta_{emission}$  are effects of vacuum polarization, vertex correction and photon emission, respectively. The energy spectrum of the “hard” radiation is limited in order to avoid the divergence in the infra-red region, where

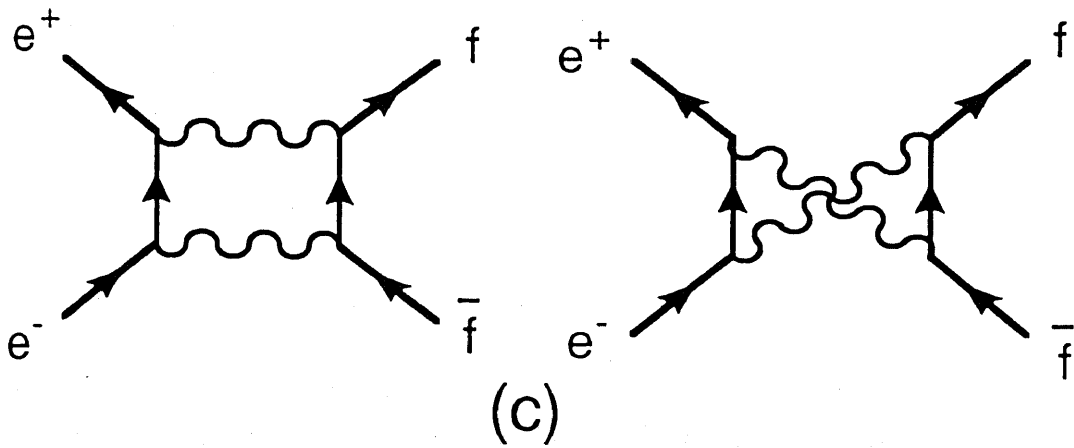
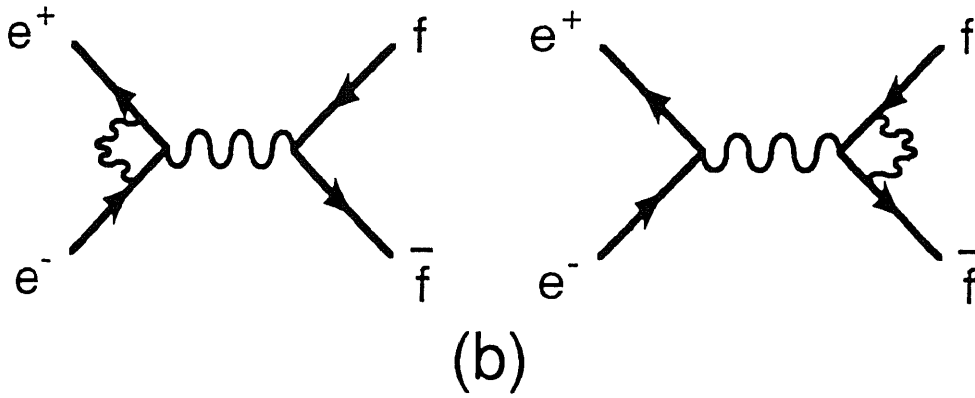
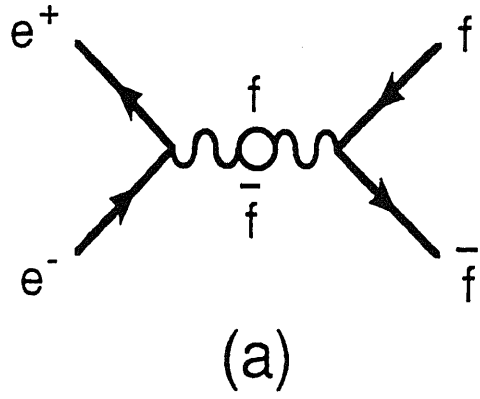


Figure 2.4: One-loop diagrams of the electroweak interaction; (a) vacuum polarizations, (b) vertex corrections and (c) box diagrams.



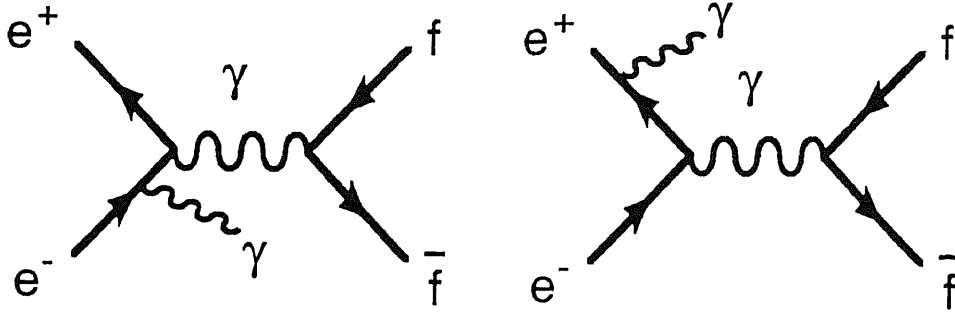


Figure 2.5: *Photon emission diagrams of the electroweak interaction.*

the correction is performed by the “soft” part neglecting real photon emission. The cut-off value on the scaled energy of the photon  $k_{min} = (E_\gamma/E_{beam})_{min}$  is normally set to 0.01. The maximum energy of the “hard” photon should be determined by the mass of the produced particle but the upper limit  $k_{max}$  is normally set to 0.99 for light particles. The magnitudes of these corrections to five-flavour quark-pair productions at  $\sqrt{s} = 60$  GeV are calculated to be  $\delta_{vacuum} = 0.0845$ ,  $\delta_{vertex} = 0.0844$  and  $\delta_{emission} = 0.0861$ . These corrections increase the total cross section by 25.5 %.

## 2.4 $B^0$ - $\overline{B}^0$ Mixing

The bottom meson  $B^0$  can make a transition to  $\overline{B}^0$ , or vice versa, via box diagrams shown in Fig. 2.6. This transition changes the observable charge asymmetry of  $b$ -quark because the  $b$ -quark charge is identified after the transition. In 1987 the ARGUS Collaboration reported the first observation of substantial  $B^0$ - $\overline{B}^0$  mixing[11]. The mixing parameters  $\chi_i$  ( $i = d, s$ ) for the semi-leptonic decay channels are defined to show the mixing effect against the charge asymmetry explicitly,

$$\chi_i = \frac{\Gamma(B_i^0 \rightarrow \overline{B}_i^0 \rightarrow l^- \nu X)}{\Gamma(B_i^0 \rightarrow l^+ \overline{\nu} X) + \Gamma(B_i^0 \rightarrow \overline{B}_i^0 \rightarrow l^- \nu X)} \quad (2.28)$$

where  $X$  denotes the decay products of  $B^0$  meson and  $0 \leq \chi_i \leq 0.5$ . The production ratio of  $B_u^+ : B_d^0 : B_s^0$  is expected to be about  $f_u : f_d : f_s = 1 : 1 : 0.3$  at PEP

and PETRA experiments. Thus, the following average above the  $B_s^0$  threshold is obtained:

$$\begin{aligned}\chi &= \frac{f_d R_d \chi_d + f_s R_s \chi_s}{f_u R_u + f_d R_d + f_s R_s} \approx f_d \chi_d + f_s \chi_s \\ &= \frac{\chi_d + 0.3 \chi_s}{2.3}\end{aligned}\tag{2.29}$$

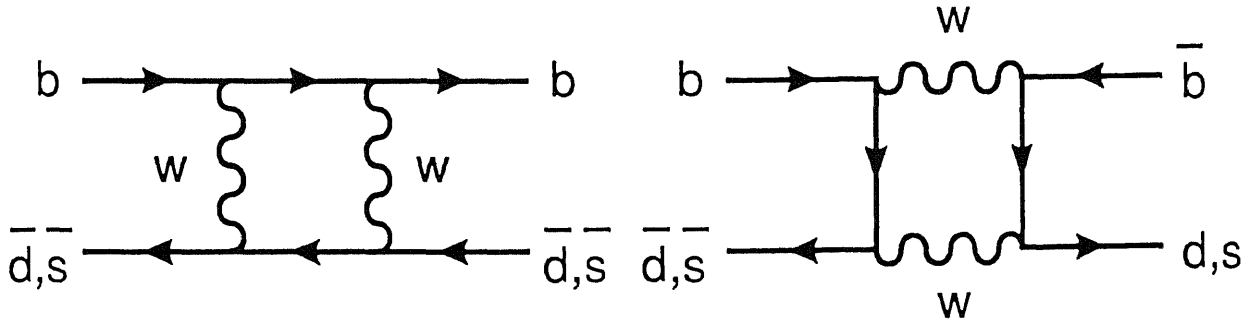
where  $R_u$ ,  $R_d$  and  $R_s$  are branching ratios and  $f_u + f_d + f_s = 1$ . The  $B_u^+$  mixing must be zero because of charge conservation in the mixing diagrams. The approximation in this equation holds under the assumption of equal semi-leptonic branching ratios of all  $B$  mesons which are implied by the spectator model, i.e.  $R_u = R_d = R_s$ . The unknown but expectedly small contribution of  $b$ -flavoured baryons can be neglected within the uncertainties in the fractions  $f_{u,d,s}$ . The measured charge asymmetry of  $b$ -quark is related to the true or Born charge asymmetry through  $B^0$ - $\overline{B}^0$  mixing[12], namely

$$A_b^{measured} = (1 - 2\chi) A_b^{true}\tag{2.30}$$

At present, the mixing parameter  $\chi_d$  is measured by the ARGUS[13] and CLEO[14] for  $B_d^0$ - $\overline{B}_d^0$  oscillations at the  $\Upsilon(4S)$  resonance. The combined value for  $\chi_d$  is obtained to be

$$\chi_d = 0.17 \pm 0.03\tag{2.31}$$

$\chi_s$  must be  $0 \sim 0.5$  from the definition. The Mark II Collaboration suggests  $\chi_s \sim 0.5$  which corresponds to the full  $B_s^0$ - $\overline{B}_s^0$  mixing.

Figure 2.6: Box diagrams for  $B^0$ - $\overline{B}^0$  mixing.



# Chapter 3

## Experimental Apparatus

The data discussed in this thesis were collected with the VENUS detector at the  $e^+e^-$  collider TRISTAN from July 1987 to July 1990. They cover center-of-mass-energies from 54.0 GeV to 64 GeV. A brief introduction of the TRISTAN accelerator and the VENUS detector is given below.

### 3.1 TRISTAN

TRISTAN<sup>1</sup>[15] is a high energy electron-positron colliding beam facility at the National Laboratory for High Energy Physics (KEK) in Tsukuba Science City, Japan. Since its start of operation in November 1986, it had provided  $e^+e^-$  collisions with the world's highest energy until SLC at SLAC and LEP at CERN were completed and came into operation at a center of mass energy in the neighborhood of the  $Z^0$  pole in April 1989 and in August 1989, respectively.

Fig. 3.1 illustrates the schematic view of the TRISTAN accelerator at the KEK site. There are four intersections and four corresponding experimental halls at the main ring. They are named counting clockwise from the southwest hall Fuji, Nikko, Tsukuba and Oho. The VENUS detector is located at the Fuji experimental hall. The TRISTAN accelerator consists of three parts, i.e. a linear accelerator (LINAC), an accumulation ring (AR) and a main ring (MR).

#### 3.1.1 Injectors

The main electron linear accelerator which is 390 m long is called LINAC. The positron generation system which is set at the upstream end of the main LINAC, consists of a pre-accelerator, a conversion section and a post accelerator. The pre-accelerator is a high current ( $\sim 10$  A) electron LINAC of 200 MeV. The electron

---

<sup>1</sup>Transposable Ring Intersecting STorage Accelerator in Nippon

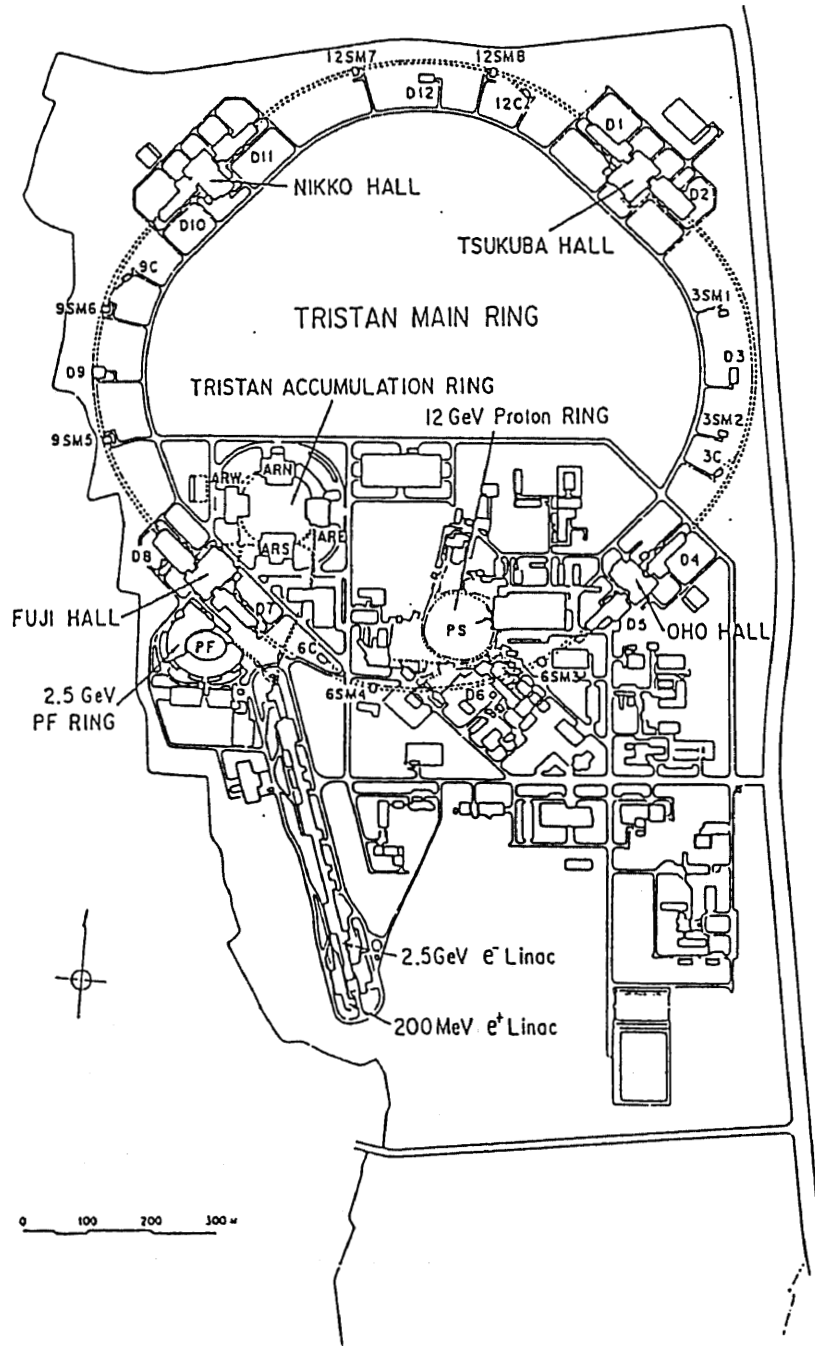


Figure 3.1: Site layout of the TRISTAN.

beam from the LINAC bombards a tantalum target and positrons are generated through the electron-positron pair creation process. The conversion section includes a solenoid magnet system which collects produced positrons. Positrons which are selected within a certain momentum acceptance are accelerated by the post accelerator up to 250 MeV and are transferred to the main LINAC.

The main LINAC accelerates electrons and positrons up to 2.5 GeV at the peak currents of about 100 mA and 15 mA, respectively, with a pulse width of 1.5 ns and injects them into the accumulation ring.

### 3.1.2 Accumulation ring

The accumulation ring which is called AR is a booster whose circumference is 377 m. It stores electrons and positrons with a maximum current of 20 mA and accelerates them up to 8.0 GeV and injects them into the main ring.

### 3.1.3 Main ring

The main colliding beam ring which is called MR has a 3018 m circumference and has a structure of four fold symmetry. The ring consists of four 194.4 m long straight sections and quadrant arcs of 346.5 m in average curvature radius. A large portion of the straight section is allocated for RF cavities ( $f_{RF} = 508.58$  MHz) which accelerate the beams from the injection energy to the required collision energy and compensate for a high rate of energy loss by intense synchrotron radiation. Electron and positron beams of two bunches each at the diagonal locations circulate in the clockwise and counter-clockwise directions, respectively. These bunches collide every 5.0  $\mu$ s with each other at the midpoints of the straight sections, where the colliding beam detectors are located. Each bunch of the circulating beams in the MR approximately has a Gaussian distribution with an effective rms width of approximately  $\sigma_x^* \sim 2$  mm in the horizontal direction,  $\sigma_y^* \sim 50 \mu$ m in the vertical direction and  $\sigma_z^* \sim 20$  mm in the beam direction at the interaction points. The energy spread  $\sigma_E$  is expressed as

$$\frac{\sigma_E}{E_b} = 0.86 \times 10^{-3} \times \frac{E_b}{\sqrt{\rho}} \quad (3.1)$$

where  $E_b$  is the beam energy in GeV and  $\rho$  stands for the bending radius of MR in units of m.  $\sigma_E/E_b = 1.39 \times 10^{-3}$  and  $\sigma_E$  amounts to 42 MeV at  $E_b = 30$  GeV. ( See reference [15]. ) The beam life time is typically 4  $\sim$  5 hours during a physics run and a typical run lasts for 1.5  $\sim$  2.0 hours. Refilling beams takes about 30 minutes. The beam life strongly depends upon the vacuum pressure in the beam duct, which is about  $0.5 \sim 1 \times 10^{-8}$  Torr.

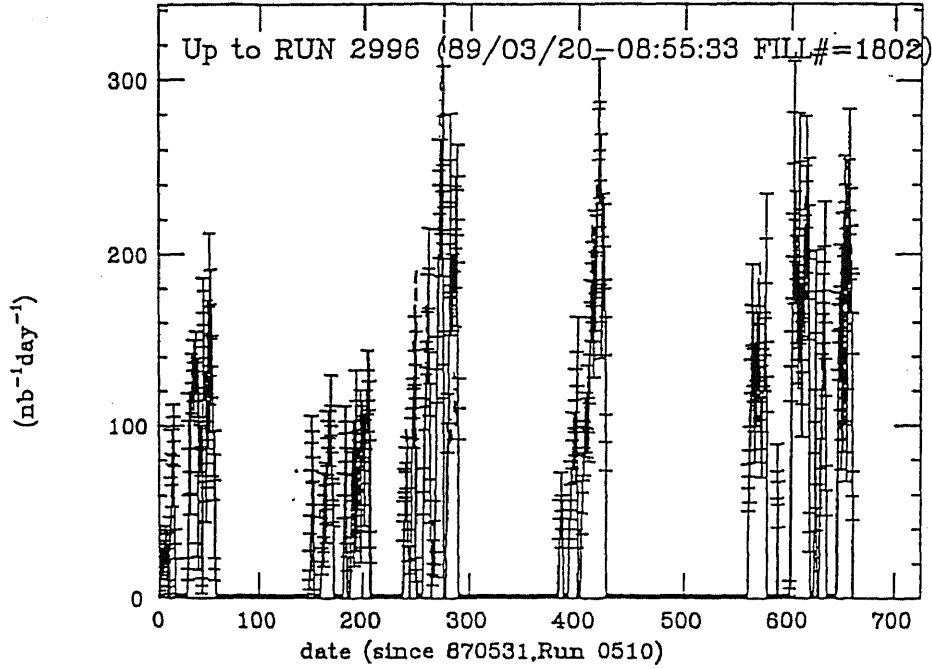


Figure 3.2: *Integrated luminosity per day measured by the VENUS.*

In the first year of the TRISTAN operation, the RF accelerating system consisted of 104 nine-cell cavities of alternating periodic structure type driven by 26 klystrons of 1 MW power at 508.58 MHz, and the colliding beam energy had reached to 28.5 GeV with an accelerating voltage of 320 MV. To upgrade the beam energy further, a superconducting cavity system was installed in addition to the conventional cavity system in the summer of 1988. The system consists of 16 units of five-cell niobium cavities and a cryogenic system to cool the cavities down to 4.2 K. The cavities were installed in the Nikko RF section, and an accelerating voltage was increased to about 440 MV. This upgrade brought the maximum beam energy to 32 GeV. The peak luminosity of  $1.4 \times 10^{31} \text{ cm}^{-2}\text{s}^{-1}$  was achieved and the integrated luminosity per day was approximately  $150 \text{ nb}^{-1}$  as shown in Fig. 3.2.

### 3.2 VENUS Detector

The VENUS<sup>2</sup> [16] detector is a general purpose magnetic spectrometer designed to study charged and neutral particles produced from  $e^+e^-$  annihilation. With

<sup>2</sup>Versatile Nilhep and Universities Spectrometer



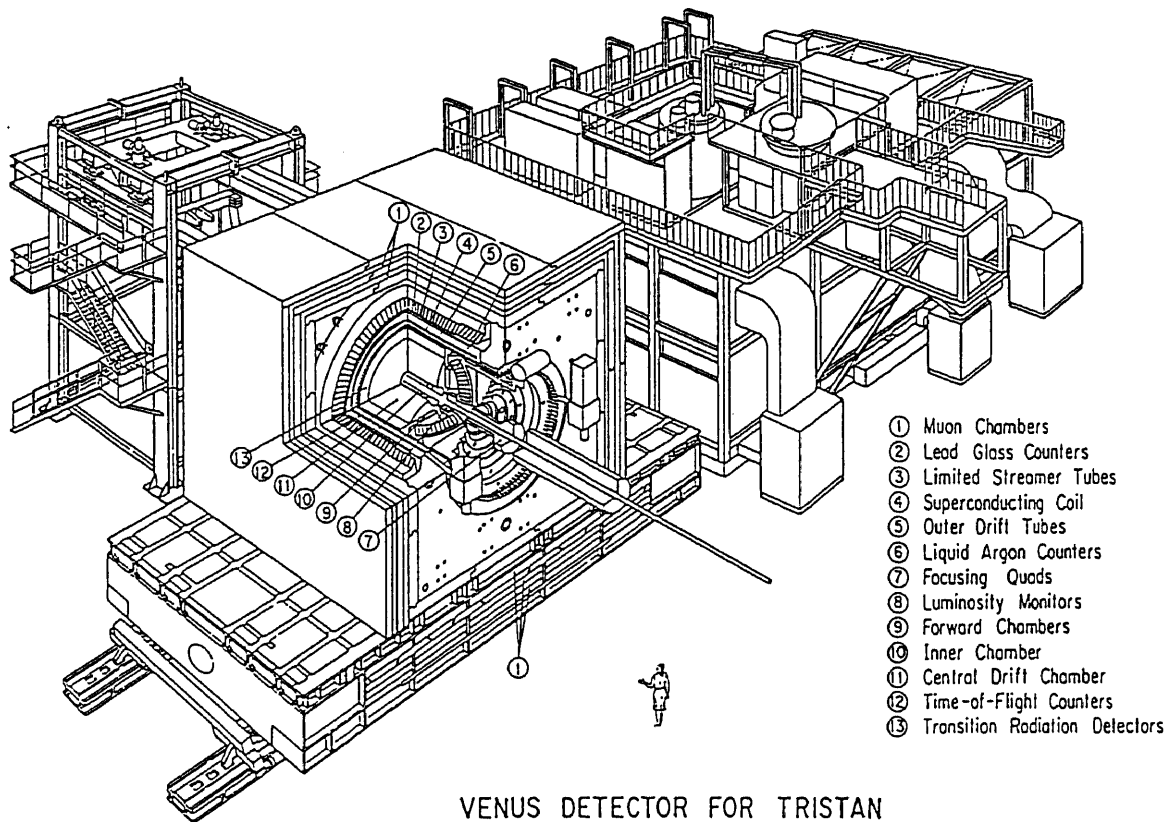


Figure 3.3: Overview of the *VENUS* detector.

the exception of the muon detector located at the outside, it has a cylindrical symmetry around the beam axis and it is located at the southwest experimental hall Fuji of the TRISTAN MR.

An overview of the *VENUS* detector is shown in Fig. 3.3. The components of the *VENUS* detector were designed using the elements whose characteristic features had been well established in the former colliding beam experiments at PEP and PETRA. Main emphases were placed to have a large angular coverage for both charged particle tracking and electromagnetic calorimetry with good momentum and energy resolutions. In particular, the electromagnetic calorimeters were designed to cover 99.7 % of  $4\pi$  solid angle without any gaps.

The *VENUS* detector started its operation in November 1986 and observed the first Bhabha event on the 19-th of November 1986. It accumulated data from

$e^+e^-$  annihilations in a broad range of the center of mass energies between 50 and 64 GeV until July 1990.

The coordinate system for data analyses is based on the right-handed Cartesian coordinate. The  $x$ -axis is horizontal and outward from the center of the TRISTAN ring, the  $y$ -axis is vertical and upward direction and  $z$ -axis is parallel to the direction of the electron beam. The origin is located at the interaction point; in other words, at the center point of the central drift chamber. The polar angle  $\theta$  is defined as the angle from the  $z$ -axis and the azimuthal angle  $\phi$  is measured in the  $x - y$  plane counter-clockwise from the  $x$ -axis.

The individual components of the VENUS detector upon which the analysis presented in this thesis relies primarily, are described in the following sections.

### 3.2.1 Central drift chamber

The central drift chamber which is frequently abbreviated to CDC[19] is a cylindrical multiwire drift chamber and is the main tracking device of the VENUS detector. An end view of the CDC in the  $r - \phi$  plane is shown in Fig. 3.4. The dimension is 300 cm long with the inner and outer radii of 25 cm and 126 cm, respectively. Since the CDC was needed to be constructed with thin material, carbon fiber reinforced plastic (CFRP) was adopted as the cylinder material because of its mechanical strength and long radiation and interaction lengths. The thicknesses of the inner and outer walls are 1.5 mm and 5.0 mm, respectively. The material thicknesses of the inner wall and tracking volume in the direction perpendicular to the beam axis are  $0.007 X_0$  and  $0.015 X_0$ , respectively. The end plates are made of 2.1 mm thick aluminium.

It has 7104 single-hit drift cells whose cross sections are  $2 \times 2 \text{ cm}^2$ . A cell unit consists of one anode wire and six cathode wires. Gold plated tungsten wires with the diameter of  $30 \mu\text{m}$  are used for anode and gold plated molybdenum wires with the diameter of  $140 \mu\text{m}$  for cathodes. There are twenty layers of axial wires parallel to the beam axis for measuring the  $r - \phi$  coordinates and nine layers of stereo wires for measuring the  $z$ -coordinates of tracks. Stereo wires are slanted with an angle of  $\pm 3.5^\circ$  with respect to the beam axis, so they are sometimes referred to as ‘slant wires’. For charged tracks in the polar angular range of  $|\cos \theta| \leq 0.75$ , their coordinates are measured in all layers. The chamber is filled with HRS gas<sup>3</sup> at an atmospheric pressure and operated at a high voltage of 2.6 kV during the data taking period.

Signals from anode wires are amplified by charge-sensitive pre-amplifiers located on the end plate and transported via twisted-pair cables to postamplifier-

---

<sup>3</sup>Ar:CO<sub>2</sub>:CH<sub>4</sub> = 89:10:1 gas mixture

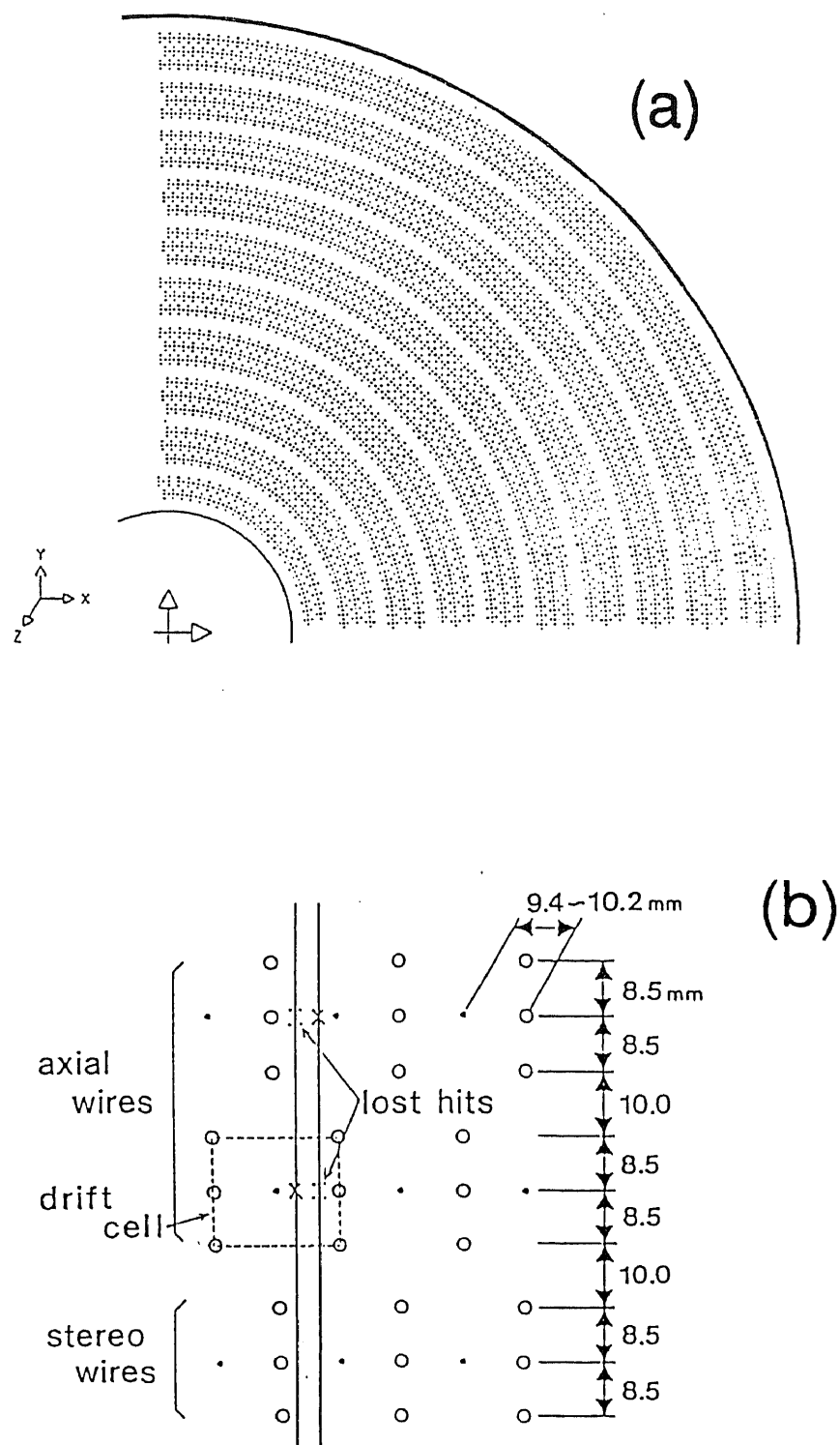


Figure 3.4: Central drift chamber; (a) end view of one quadrant and (b) cell geometry.

discriminators in the electronics hut. The drift time is digitized and measured by using the FASTBUS TDC system. The outputs of the discriminators are also fed to a fast track finder module (TFM) on FASTBUS[17] and generate a fast  $r - \phi$  track trigger signal with the look-up table method. Tracks within a polar angle range of  $|\cos \theta| \leq 0.87$  whose transverse momenta are larger than 0.7 GeV/c are detected with the detection efficiency of more than 99 %.

Since charged tracks in the range of  $|\cos \theta| \leq 0.75$  are able to pass through all the axial and slant layers, the tracking performance is evaluated by using Bhabha scattering events. The mean spatial resolution is measured to be 270  $\mu\text{m}$  at each axial layer. The vertex resolutions for high  $P_t$  tracks are given to be

$$\begin{cases} \sigma_{vtx(r-\phi)} \simeq 460 \mu\text{m} \\ \sigma_{vtx(z)} \simeq 6.7 \text{mm} \end{cases}$$

when multiple coulomb scattering is neglected. In the same way, the angular resolutions in the polar and azimuthal angles are estimated to be

$$\begin{cases} \sigma_\theta = 9 \times \sin^2 \theta \text{mrad} \\ \sigma_\phi = 1.3 \text{mrad} \end{cases}$$

The measurement of the polar angle is much less accurate than that for the azimuthal angle. The momentum resolution in the  $r - \phi$  plane under the magnetic field of 0.75 T is estimated to be

$$\frac{\sigma_{p_t}}{p_t} = \sqrt{(1.3\%)^2 + (0.8\% \times p_t)^2} \quad (3.2)$$

with  $p_t$  measured in GeV/c. The first term is the contribution from multiple coulomb scattering. The second is due to the finite spatial resolution of the chamber. The reconstruction efficiency for the high- $p_t$  charged tracks in the range of  $|\cos \theta| \leq 0.75$  is better than 99.9 % in the  $r - \phi$  plane and 98.0 % in the  $s - z$  plane<sup>4</sup>.

### 3.2.2 Barrel lead glass calorimeter

The lead glass calorimeter (LG)[20] is an electromagnetic shower calorimeter in the barrel region dedicated to the detection of electromagnetic particles such as electrons and photons. It is located outside the solenoid magnet and covers the range of  $|\cos \theta| \leq 0.8$  and  $2\pi$  in the azimuth angle. It has the radial range of 197-230 cm and the length of 615 cm. The LG consists of 5160 lead glass modules segmented into 120 blocks in  $\phi$  view and into 43 blocks in  $\theta$  view. A lead glass

---

<sup>4</sup>spiral plane: the plane containing the track

block is made of NIKON DF6<sup>5</sup> and has a radiation length of 1.69 cm and a critical energy of 12.6 MeV. A typical module has a cross section of  $12.0 \times 11.6 \text{ cm}^2$  at the front face and a depth of 30 cm which corresponds to  $18.0 X_0$ .

The LG is divided into seven sections in the  $z$ -direction and modules are set parallel within each section as shown in Fig. 3.5. The lead glass modules are pointed to the interaction region to minimize the multi-hit probability of particles. Their longitudinal axes are, however, tilted from the ideal pointing geometry by  $2^\circ$  to  $14^\circ$  in the  $\theta$  direction and by  $3^\circ$  in the  $\phi$  direction. This semi-tower geometry prevents photons from escaping through gaps between modules. A schematic view of a lead glass module is shown in Fig. 3.6. A three inch diameter photomultiplier surrounded by a  $\mu$ -metal magnetic shield is attached to each lead glass block with a plastic light guide of 5 cm in length. In the central part of the LG, the photomultipliers are R1911<sup>6</sup> and at the both end parts where the leakage field is 20 to 30 Gauss, they are R1652<sup>7</sup>.

Particle energies are measured with Čerenkov lights which are emitted by charged particles in electromagnetic showers. The total amount of the light yield is proportional to the energy deposit in modules. The relation between the energy deposit and the light yield was calibrated by using the electron beam. Furthermore, in order to trace the gain fluctuation of photomultipliers, a monitoring system of a Xe flash tube with an optical fiber system is adopted. Lights are amplified by photomultipliers and signals from the photomultipliers are sent to 96 channel 12-bit charge integrating ADC modules<sup>8</sup> on FASTBUS. They integrate the charges of the signals and digitize the integrated charge.

For the energy trigger, the LG is divided into 58 segments with seven segments in the  $\theta$  direction and eight or ten segments in the  $\phi$  direction. Each ADC module corresponding to one segment produces an analog segment-sum signal. Each segment-sum signal is sent to a discriminator and its output is used for the segment-sum trigger. Also, all 58 segment-sum signals are sent to an analog-sum circuit to obtain the total energy deposit in the LG which is used for the total energy-sum trigger.

The energy resolution for an electromagnetic shower is estimated to be

$$\frac{\sigma_E}{E} = 2.5\% + \frac{7.0\%}{\sqrt{E}} \quad (3.3)$$

where  $E$  is measured in GeV. The first term accounts for errors such as instrumental noise, shower leakage and inter calibration uncertainties. The second is due to

---

<sup>5</sup>Its main components are PbO (70.9 %) and SiO<sub>2</sub> (27.3 %) and the refractive index is 1.805.

<sup>6</sup>Hamamatsu Photonics: box and grid type photomultiplier.

<sup>7</sup>Hamamatsu Photonics: mesh type photomultiplier.

<sup>8</sup>LeCroy 1885

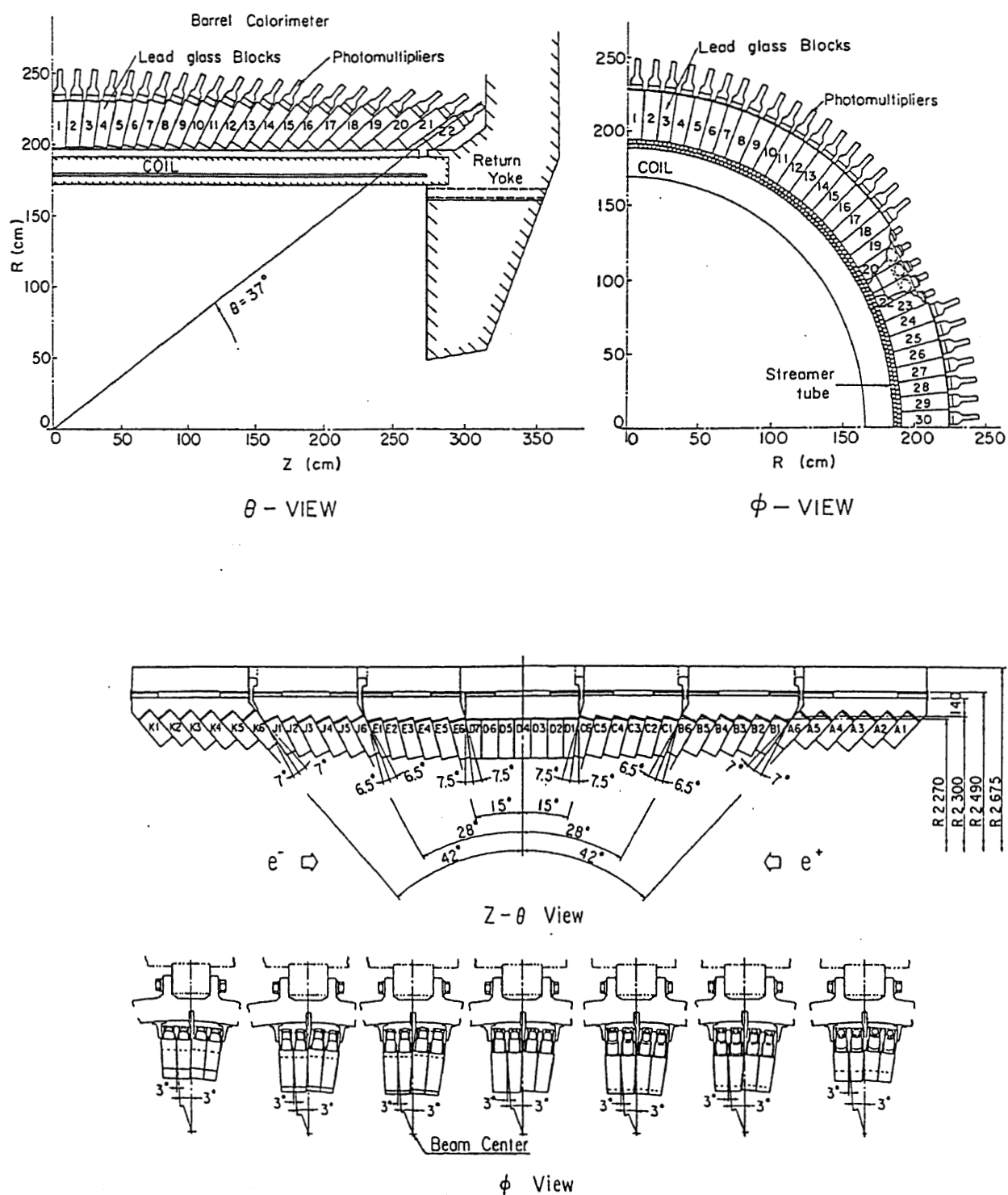


Figure 3.5: Arrangement of the lead-glass counters.

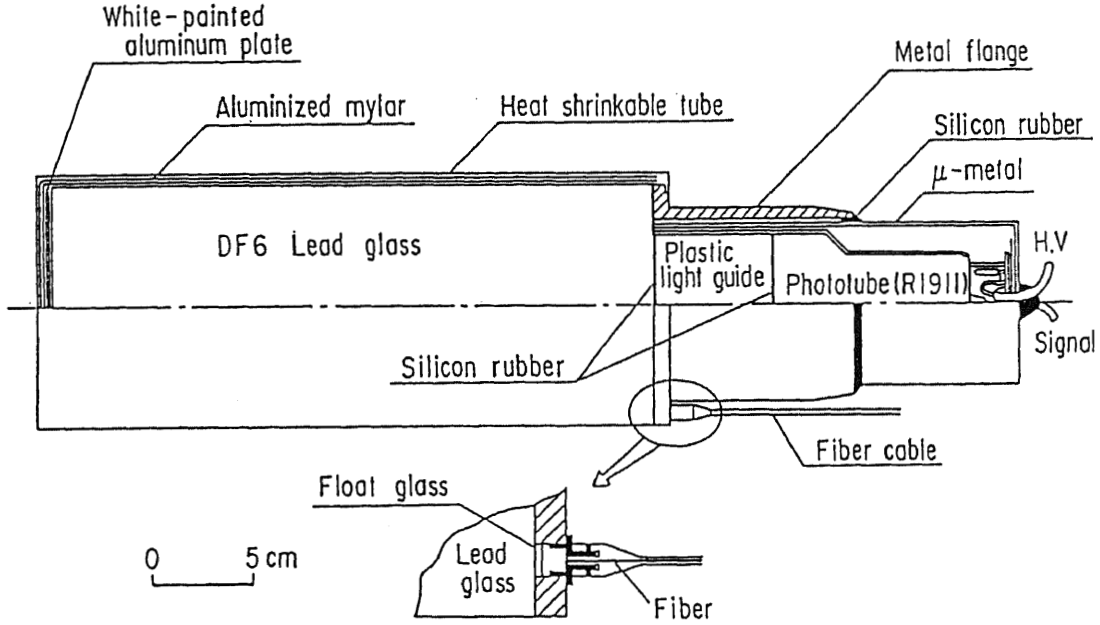


Figure 3.6: *Assembly of a lead-glass counter module.*

the statistical fluctuation of the number of photo-electrons. The angular resolution is also estimated by comparing the measured shower-center position with the CDC track extrapolated to the surface of the LG module for large angle Bhabha scattering events. It is obtained to be

$$\begin{cases} \sigma_{\theta} = 4.0\text{mrad} \\ \sigma_{\phi} = 5.2\text{mrad} \end{cases}$$

### 3.2.3 End-cap liquid argon calorimeter

The end-cap liquid argon calorimeter (LA)[21] is a sampling calorimeter for measuring energies of electromagnetic particles which emerge in the forward region. The energies are measured by collecting charges from ionization induced by shower particles. Two liquid argon calorimeters are installed between the CDC and both end-caps of the return yoke and cover an angular range of  $0.79 \leq |\cos \theta| \leq 0.99$  as shown in Fig. 3.7. There is no energy leakage gap between the end-cap and barrel calorimeters. Each liquid argon calorimeter consists of 480 tower modules which look at the point toward 80 cm beyond the interaction point on the beam axis. Each tower module consists of 70 calcium-lead plates of 1.5 mm in thickness corresponding to  $20.3 X_0$ . The whole calorimeters are soaked in liquid argon at 86

K.

Each side of the calorimeter has 1920 signal readout channels and lead plates of each tower are electrically segmented into four groups. Signals are amplified by pre-amplifiers placed on the outer vessel of the calorimeter and transmitted to shaper-amplifiers. Pulse heights are measured by sample-and-hold ADC's in TKO[18] boxes. Each calorimeter is divided into twelve sectors. The angle between two adjacent sectors is  $30^\circ$  in the  $r - \phi$  plane. Each sector is further divided into the inner and outer part subsectors, which have the angular ranges of  $0.91 \leq |\cos \theta| \leq 0.99$  and  $0.79 \leq |\cos \theta| \leq 0.91$ , respectively. The energy-sum signals are provided by analog sum circuits and two kinds of energy-sum triggers are obtained. The energy-sum signals from the 48 subsectors in both sides are used for the sector-sum trigger. The total sum signal of all the 1920 channels for each side of the LA is used for the total sum trigger.

The energy resolution of the LA is estimated by using radiative Bhabha scattering events, to be

$$\frac{\sigma_E}{E} = 1.6\% + \frac{10.2\%}{\sqrt{E}} \quad (3.4)$$

where  $E$  is measured in GeV. There are some intrinsic uncertainties as for the LG. The first term accounts for the errors such as instrumental noises, shower leakage and inter calibration uncertainties. The second is due to the statistical fluctuations of the energy deposition in the liquid argon which is known as the Landau fluctuations and the track length of the electromagnetic shower. The normalization factor for the energy calibration is given by measuring energies of Bhabha events. The angular resolution is also estimated by using the same method as that used for the LG. It is obtained to be

$$\begin{cases} \sigma_\theta = 2.9 \pm 0.6 \text{ mrad} \\ \sigma_\phi = \frac{2.6 \pm 0.3}{\sin \theta} \text{ mrad} \end{cases}$$

where errors are due to results of fitting.

### 3.2.4 Barrel muon detector

The muon detector system covers the large outermost area of the VENUS detector to detect penetrating particles. It consists of four layered arrays of aluminium modules. Each module consists of two layers of four cells staggered by a half cell as shown in Fig. 3.8. Each cell has a cross section of  $5 \times 7 \text{ cm}^2$  with the wall thickness of 2.5 mm in average. The length of a module is 760 cm. A sense wire is stretched at the center of each cell with a tension of 400 gw. The sense wire has the diameter of  $70 \text{ } \mu\text{m}$  and made of gold-plated tungsten with 3 % rhenium.



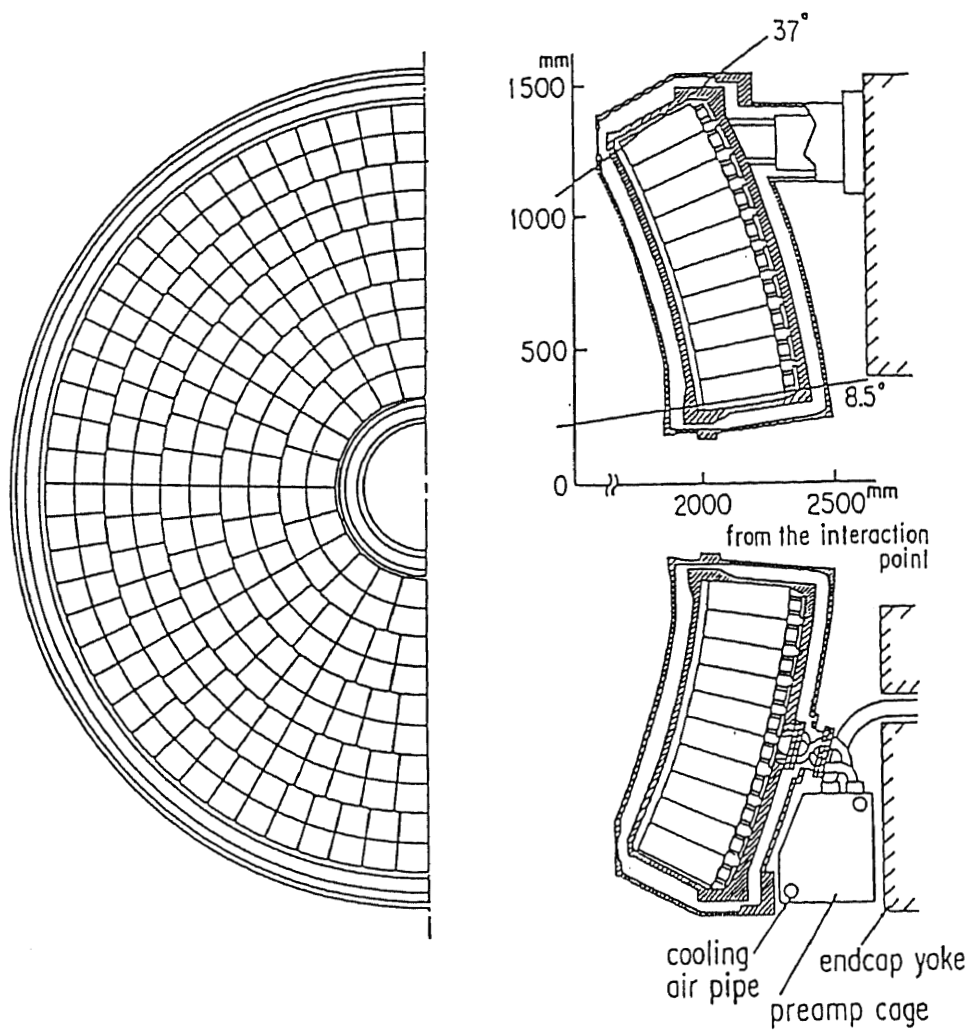


Figure 3.7: *End and side views of the liquid argon calorimeter.*

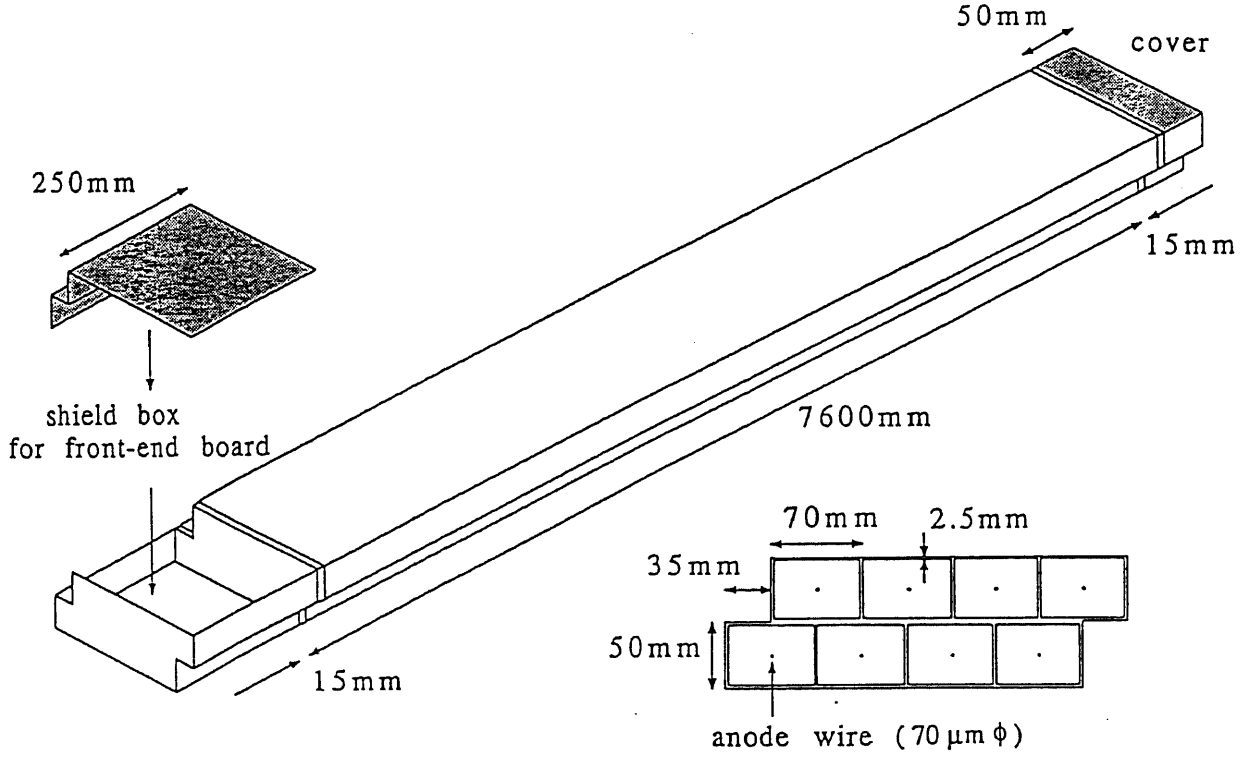


Figure 3.8: *Eight-cell drift tube module of the muon detector.*

Modules are filled with P-10 gas<sup>9</sup> and to each sense wire a high voltage of 2.7 kV is applied. The drift tubes of the muon detector are operated in a proportional mode. Three layers of modules interleaved with 20 cm thick iron filters measure the  $r - \phi$  positions. The outermost layer of modules is located just outside of the third layer without iron filters. It measures the  $z$ -positions. The barrel muon detector has an angular range of  $|\cos \theta| \leq 0.695$ .

Signals from anode wires are amplified and digitized by front-end electronics boards which are mounted at one end of modules. The digitized data are sent to memory boards on TKO boxes in the electronics hut through two types of address generator boards: Main Address Generator and Module Address Generator.

The performance of the muon drift tube modules was tested by using cosmic

---

<sup>9</sup>Ar:CH<sub>4</sub> = 90:10 gas mixture

rays. The results of the bench test which was carried out before installation have been reported[22]. After the installation, a cosmic ray test was performed by using the FB muon detector<sup>10</sup>. A detailed description of this test can be found in Reference[23].

### 3.2.5 Other detector components

#### Inner drift chamber

The inner drift chamber (IC) is a cylindrical multiwire drift chamber[24]. The length is 160 cm and the inner and outer radii are 10 cm and 25 cm, respectively. In order to minimize multiple coulomb scattering and photon conversion in the chamber, the chamber walls are made of paper honeycomb cylinders. The material thickness of this chamber amounts to  $0.03 X_0$  in the direction of  $\theta = 90^\circ$ . The IC has six layers of anode wires and cathode planes. The cathode planes cover the polar angle from  $16.3^\circ$  to  $163.7^\circ$  and each plane is divided into 128 pads, namely 16 divisions in the  $\theta$ -direction and 8 divisions in the  $\phi$ -direction. The cathode pads are located in a tower geometry pointing to the interaction region. Signals from the cathode pads are processed by shaper amplifiers and sent to discriminators. Hit information of the cathode pads is fed into fast track-finding processors which look for charged tracks coming from the interaction point in the  $r - \phi$  plane and serves the information for the event trigger.

#### Time of flight counter

The time of flight counter (TOF)[25] is located on the inner wall surface of the superconducting magnet and covers an angular range of  $|\cos \theta| \leq 0.818$  with the inner radius of 164 cm. It consists of 96 plastic scintillators whose dimension is  $4.2 \times 10.7 \times 466 \text{ cm}^3$ . There are 3 mm gaps between adjacent scintillators and they cause an inefficiency of about 3 %. The TOF is used for triggering and identification of detected particles by accurately measuring their flight times. Each end of a scintillator is viewed by a photomultiplier tube<sup>11</sup> through an acrylic light guide of 145 cm in length. The obtained time resolution was 200 ps for Bhabha and  $\mu$ -pair events. The  $z$ -coordinate of a charged particle was determined by a time difference method with a resolution of 5 cm.

---

<sup>10</sup>Forward-backward muon detector. In this thesis, it has not been used.

<sup>11</sup>Hamamatsu Photonics H1949-01

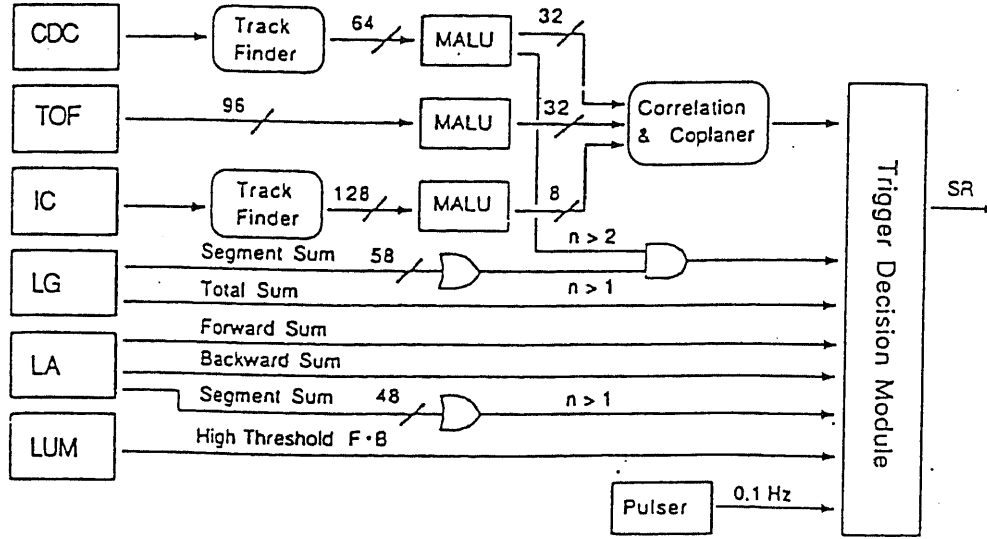


Figure 3.9: Block diagram of the trigger logic.

### Luminosity monitor

The luminosity monitor (LM)[26] measures the luminosity by detecting very small angle Bhabha scattering events. It consists of 27 layers of lead sheets and scintillators and the total thickness amounts to  $20 X_0$ . The LM covers an angular range of  $0.988 \leq |\cos \theta| \leq 0.997$ . The LM module at each end of the VENUS detector is divided into eight pieces in the  $r - \phi$  plane. For triggering the small angle Bhabha scattering events, large energy deposits in both sides with back to back configuration were required. The energy resolution was evaluated to be

$$\frac{\sigma_E}{E} = \frac{37\%}{\sqrt{E(\text{GeV})}} \quad (3.5)$$

## 3.3 Event Trigger

The TRISTAN accelerator has been operated with a two-bunch mode whose crossing interval is  $5 \mu\text{s}$ . A trigger system is required to control selective recording of data with fast signals. The VENUS trigger system is composed of two levels: a first-level trigger is designed to work between beam crossings and a second-level trigger is a rather slow software trigger.

The first-level trigger carries out the trigger decision within every  $5 \mu\text{s}$  and data are taken by an on-line computer VAX11/780 or a 68K20-FPI microprocessor module on FASTBUS. Also the first-level trigger has two types of triggers; one

is a neutral trigger which is based on a high energy deposit in electromagnetic calorimeters, and the other is a charged-track trigger which is based on the signals from the IC and CDC. Trigger signals are processed by the trigger decision module (TDM). The diagram of the trigger logic is shown in Fig. 3.9. The TDM has a memory look-up table and generates a FASTBUS service request (SR) signal to mask the subsequent clear signals if the trigger condition is satisfied. Trigger decision is made within a collision interval of  $5 \mu\text{s}$ . The first-level trigger conditions are as follows:

- Neutral trigger

$$\begin{cases} LG_{totalsum} & E \geq 5 \text{ GeV} \\ LA_{totalsum} & E \geq 6 \text{ GeV} \\ LA_{sectorsum} & E \geq 2.5 \text{ GeV} \end{cases}$$

- Charged track trigger

$$\begin{cases} coplanar & (2 \text{ charged tracks}) \times (2 \text{ TOF hits}) \times (\text{IC hits}) \\ LG_{segmentsum} & (E \geq 0.7 \text{ GeV}) \times (2 \text{ charged tracks}) \end{cases}$$

- LM trigger

$$\text{luminosity} \quad (E_F \geq 10 \text{ GeV}) \times (E_B \geq 10 \text{ GeV})$$

- Random trigger

$$\text{random (clock)} \quad 0.1 \text{ Hz}$$

‘Tracks’ seen in the above list are found by the fast track-finder of the CDC and must have a transverse momentum greater than  $0.7 \text{ GeV}/c$ . For the coplanar trigger condition, the acoplanarity angle between two tracks must be less than  $10^\circ$ . The acoplanarity angle is defined as the supplementary angle in the  $r - \phi$  plane between the two tracks and expressed as:

$$\theta_{acop} = \cos^{-1} \left( \frac{-\vec{p}_{t1} \cdot \vec{p}_{t2}}{|\vec{p}_{t1}| |\vec{p}_{t2}|} \right) \quad (3.6)$$

where  $\vec{p}_{t1}$  and  $\vec{p}_{t2}$  are the momentum vectors projected onto the  $r - \phi$  plane. The acceptance of the coplanar trigger was extended to  $\theta_{acop} \leq 60^\circ$  in November 1988.

The coplanar triggered events in the first-level trigger condition contain a large amount of backgrounds which amount to about a half of all the events. The second-level trigger is a software trigger with 68K20-FPI which processes information of the TFM and TOF. It reduces the number of coplanar triggered events to about 50 % by using severer track finding conditions than that in the first-level.

The total trigger rate is typically 5 Hz though it strongly depends on the beam condition.

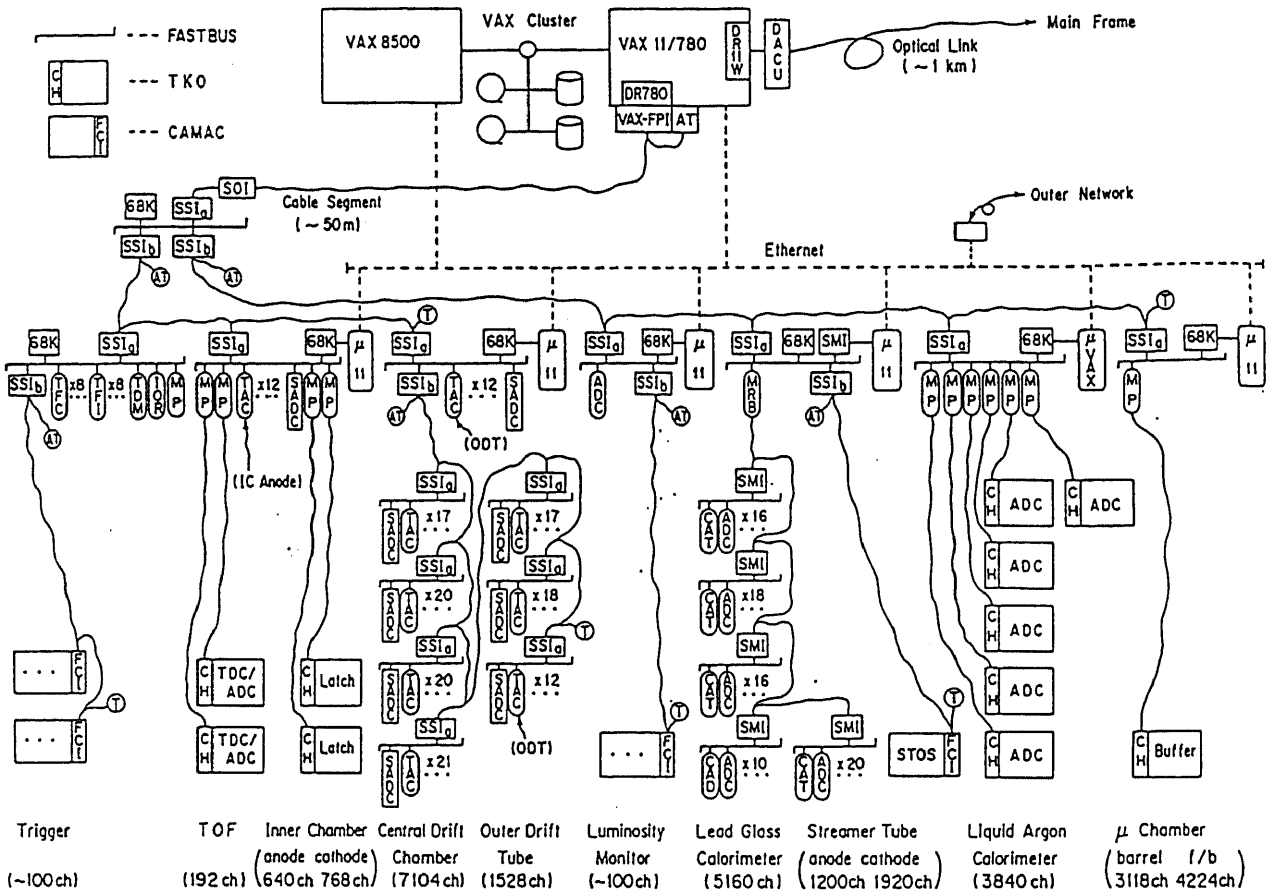


Figure 3.10: VENUS data acquisition system.

### 3.4 Data Acquisition System

The VENUS data acquisition system[27] deals with more than 30,000 channels of readout electronics and has a tree-like structure as shown in Fig. 3.10. Signals from the ten detector components are processed at the front-end electronics of CAMAC, FASTBUS and TKO. All digitized data are transferred to FASTBUS memory buffers and collected whenever an event trigger occurs. The collected data are sent to the on-line computer system, the VAX11/780-VAX8530 cluster, through the FASTBUS-VAX interface. The on-line computer controls the data acquisition and makes quick analyses for monitoring the data status. A typical time for data acquisition was 28 ms per event and dead time was 10 %. Data collected on the on-line computer are sent to the main frame computer FACOM M780 which replaced M382 in March 1988 via optical fibers and stored in the automatic loading cartridge tape library. A typical data size was 5 kB.

# Chapter 4

## Multihadronic Final States

The triggered data sample contains a large amount of background events. For example, they are beam beam-pipe interactions, beam residual-gas interactions and cosmic rays. In order to reduce the data size and select multi-hadronic events, the following event reconstruction process and selection criteria are required.

### 4.1 Event Reconstruction

The event reconstruction consists of two steps. At first, the raw data are converted to the physical quantities through calibration routines. For example, TDC data of the CDC are converted to drift lengths and ADC data of the calorimeters to energies deposited. Secondly, analysis routines process the calibrated data and provide several sets of particle information such as momenta and trajectories in the CDC, energy deposits and positions in the LG, and so on.

#### 4.1.1 CDC track reconstruction

The trajectories of charged particles in the CDC are reconstructed by a program named PERPR[28]. The reconstruction procedure is carried out in both the  $r - \phi$  and  $r - z$  planes as follows.

##### Reconstruction in the $r - \phi$ plane

Since the magnetic field of 0.75 T is applied along the  $z$ -axis, the trajectory of a charged particle is a spiral in the three dimensional space. When projected onto the  $r - \phi$  plane, the trajectory follows a circle and the transverse momentum  $p_t$  is given by

$$p_t(\text{GeV}/c) = 0.3 \times B(\text{T}) \times \rho(\text{m}) \quad (4.1)$$

where  $B$  is a magnetic field strength and  $\rho$  is a radius of the circle. The track reconstruction in the  $r - \phi$  plane is based on the hit information of axial layers of the CDC. The reconstruction algorithm of the PERPR is given as follows:

1. PERPR searches the initial ‘road’ in the outmost two axial layers of the CDC. After finding successive hits in these layers, the ‘road’ of a track is defined. Then four combinations of a track are possible because of the left-right ambiguity in the ‘road’.
2. Further search is made for the candidate hits along the ‘road’ and the track is extended with the help of axial wire positions. By using a method of the least  $\chi^2$  fit, the most likely track is determined by eliminating bad quality hits. In this step, the left-right ambiguity of that track is solved. If the value of reduced  $\chi^2$  exceeds five, the track is abandoned.
3. The program determines physical quantities associated with measured tracks such as charges,  $p_t$  and  $R_{min}$ . The  $R_{min}$  is the distance between the interaction point and the closest point of the track to the interaction point. If the interaction point is inside the track circle, the sign of  $R_{min}$  is assigned to positive and otherwise negative. The definition of  $R_{min}$  is shown in Fig. 4.1

### Reconstruction in the $r - z$ plane

To determine the particle trajectory in the  $z$  direction, hit information of slant layers in association with the axial layer hits is used. The  $z$  coordinate of the track is given by

$$z = \frac{l}{2} - \frac{d}{\tan \alpha} \quad (4.2)$$

where  $d$  is the distance between the axial track which is reconstructed in the  $r - \phi$  plane and the slant wire hit.  $\alpha$  is the slant angle (  $3.5^\circ$  ) and  $l$  is the slant wire length projected onto the beam axis. The track finding algorithm in the  $r - z$  plane is similar to that in the  $r - \phi$  plane. The  $z$  coordinate can be expressed by a linear form with a useful parameter  $Z_{min}$  for further analyses,

$$z = \frac{dz}{ds}s + Z_{min} \quad (4.3)$$

where  $Z_{min}$  is the  $z$  coordinate of the point which gives  $R_{min}$  and  $s$  is the length of the arc element in the  $r - \phi$  plane. The definition of  $Z_{min}$  is shown in Fig. 4.1.

#### 4.1.2 LG clustering

A shower energy is shared by several neighbouring lead glass blocks. Such sharing of energy permits the measurement of the shower center position with a precision



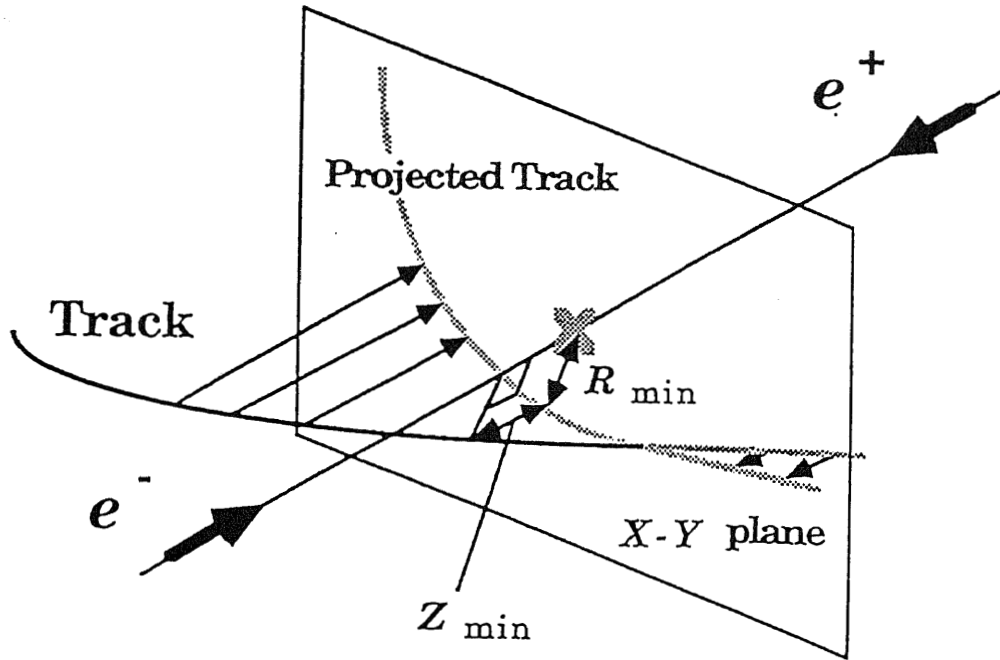


Figure 4.1: Definition of track parameters.

better than the granularity of the blocks. In order to determine the shower energy and its incident position, the clustering of electromagnetic signals in the LG is performed as follows:

1. Starting from the module which contains the highest energy, the neighbouring modules are examined whether they belong to the same cluster or not. Thus, the 'connected region' is formed by searching all neighbouring modules adjacent in  $\theta$  and  $\phi$  directions.
2. The shower energy is determined by summing up the energy deposits which belong to the same cluster.
3. The incident position of the electromagnetic particle is defined by the energy-weighted mean position of the lead glass modules, namely

$$x_{cluster} = \frac{\sum_i (E_i)^\alpha x_i}{\sum_i (E_i)^\alpha} \quad (4.4)$$

where  $x_i$  is the central  $\theta$  and  $\phi$  positions of the  $i$ -th block in the cluster and the weighting exponent  $\alpha$  is optimized to be 0.34 by the Monte Carlo program EGS4[29].

### 4.1.3 LA clustering

The cluster-finding algorithm for the LA is similar to that for the LG. The lateral spread  $E(x)$  of an electromagnetic shower is described approximately by the following exponential form:

$$E(x) = E_0 e^{-\frac{|x|}{\lambda}} \quad (4.5)$$

where  $x$  is the lateral distance from the shower center and  $\lambda$  represents the shower extension. The parameter  $\lambda$  is taken as a function of the lateral energy and therefore, it is given by

$$\lambda = g(y) \quad (4.6)$$

$$y = \ln \frac{1}{2} \left( \frac{E_i}{E_{i+1}} \right) \quad (4.7)$$

where  $E_i$  represents the energy deposit in the  $i$ -th tower. The function  $g(y)$  is parametrized by using the EGS4.

The polar angle  $\theta$  of the shower center is obtained by

$$g(y) = (a_0 + a_1 y^2) \times (1 \pm \beta \Delta\theta) \quad (4.8)$$

where  $\beta \Delta\theta$  corresponds to the detector inclination against the interaction point and  $\beta = 0.45$ . In the above equation, the plus sign corresponds to the LA placed in the positive  $\cos\theta$  side of the VENUS detector, while the minus sign corresponds to that in the negative side. Firstly, the energy deposits per ring are integrated over the  $\phi$  direction. Secondly, the shower energy is calculated by using only the modules adjacent to the tower which contains the maximum energy. This procedure is applied for the four longitudinal layers and the average shower center is calculated.

The azimuthal angle of the shower center is calculated in a way similar to that for the polar angle, but in this case there is no detector inclination. Therefore, it is given by

$$g(y) = a_0 + a_1 y^2 \quad (4.9)$$

To find the shower center, only the modules adjacent to the tower which contains the maximum energy in the  $\phi$  direction are required.

## 4.2 Data Reduction

For an efficient analysis, reduction of background events at an early stage is necessary. Two steps of the data reduction are performed for the present analysis. At the first stage, 'Process 1' is applied to all the collected data to discard as many events as possible without losing interesting events.

### 4.2.1 Process 1

Process 1 which is abbreviated to PROC-1 is a general purpose event filter of the triggered events. It is intended for the selection of events from  $e^+e^-$  collisions and the reduction of backgrounds such as beam beam-pipe events. Process 1 consists of two steps. The first step is preselection without event reconstruction and the second step is genuine selection after reconstruction of the CDC and the calorimeters.

At first, events accepted by the LM trigger and the random trigger are rejected. The preselection rejects the events which do not have any tracks originating from the interaction point in spite of the fact that they are accepted by the charged track trigger. The vertex positions of any charged tracks are examined in the  $r - z$  plane by using the information of hits of cathode pads of the IC. More than four layer hits out of six layers of associated towers are required for each charged track found by the track finder of the CDC. Tracks which are not connected to hit towers, or whose vertices are away from the interaction point are discarded as fake tracks. For the coplanar trigger, a pair of back-to-back tracks are required. For the LG segment sum trigger, at least two tracks are required. About 50 % of the events accepted by only the charged track trigger are rejected by this preselection. All the events accepted by the neutral trigger are not examined in this preselection stage.

Next, the reconstruction of the CDC tracks and the LG and LA calorimeters are carried out. The events are sent to the next stage if at least one of the following requirements are satisfied.

1. Total shower energy deposited in the LG is larger than 3.0 GeV for the events accepted by the LG total trigger.
2. Total shower energy deposited in the LA is larger than 3.0 GeV for the events accepted by the LA total trigger.
3. Total shower energy deposited in the LA is larger than 1.5 GeV for the events accepted by the LA sector sum trigger.
4. At least two ‘long tracks’ are detected in the CDC for the events accepted by the coplanar trigger.

The ‘long track’ must satisfy the following conditions:

- The track is reconstructed in both the  $r - \phi$  and  $r - z$  planes with more than nine axial wire hits and more than three stereo wire hits.
- $|R_{min}| < 7$  cm and  $|Z_{min}| < 30$  cm.

- The transverse momentum is larger than 0.2 GeV/c.
5. At least one long track is detected in the CDC and the total energy sum of the LG is larger than 0.5 GeV for the event accepted by the LG segment sum trigger.

The data reduction ratio of Process 1 is about 35 %.

#### 4.2.2 Process 2

Process 2 which is abbreviated to PROC-2 is a single purpose event filter. Three kinds of Process 2 programs are prepared for the event filters of multi-hadronic, QED and low multiplicity events. The purpose of the first program is to make samples of the events with many energetic charged particles and certain energy deposits in the calorimeters. These events are called the multi-hadronic events due to quark pair production. The second program is for the selection of events with high energy deposits in the calorimeters. These events include Bhabha scattering or  $\gamma\gamma$  events. The third program selects events with low charged-track multiplicity due to  $\mu\mu$  or  $\tau\tau$  production.

In the present analysis the data samples of the multi-hadronic events are used. Process 2, however, executes a preselection and an exact multi-hadronic event selection will be carried out at the next stage. Data summary tapes after the selection by the Multi-hadronic Process 2 contain about 15000 events at center-of-mass energies between 54 and 64 GeV. The selection criteria in Process 2 are as follows:

1. Total shower energy deposit in the LG and LA,  $E_{cal}$ , is larger than 5 GeV.

$E_{cal}$  is defined as a sum of the shower energy deposits in the LG and the outer parts of the LA on both sides. The outer parts are the 7-th to 10-th rings which correspond to the angular range of  $|\cos\theta| < 0.89$ . Energy deposits in the inner parts of the LA are excluded in  $E_{cal}$  for lack of the tracking capability in this region.

2. The number of 'good tracks' is at least five.

A 'good track' satisfies the following requirements:

- The track is reconstructed with at least eight hits of the axial layers and four of the stereo layers of the CDC.
- The transverse momentum is larger than 0.2 GeV/c.
- $|R_{min}| < 2$  cm

- $|Z_{min}| < 20$  cm
- $|\cos \theta| < 0.85$

The energy-deposit cut rejects backgrounds from two photon processes and cosmic rays. The cut by the number of good tracks excludes Bhabha scattering and  $e^+e^- \rightarrow \tau\tau$  events. Process 2 rejects more than 90 % of the total events which survived in Process 1.

### 4.2.3 Multi-hadronic event selection

The selection criteria for multi-hadronic events produced via single photon/ $Z^0$  annihilation are optimized in order to minimize background contamination. Multi-hadronic events are characterized by large visible energies and small missing momenta along the beam direction.

Event selection criteria are as follows:

- Total energy deposit in the calorimeter ( $E_{cal}$ ) is larger than 5 GeV, where  $E_{cal}$  is the sum of the deposit energy in the LG and LA within  $|\cos \theta| < 0.89$ . The reason why the energy deposit in the inner part of the LA is excluded is attributed to the poor tracking efficiency of the CDC in this region as described in the previous section. In addition, this criterion is effective for the suppression of the trigger bias. Fig. 4.2 shows the distribution of  $E_{cal}$  at center-of-mass energies of about 58 GeV.
- At least five good tracks ( $N_{good}$ ) are observed in CDC. A good track is defined in the previous subsection.
- Total visible energy ( $E_{vis}$ ) is greater than the beam energy.  $E_{vis}$  is defined as the sum of momenta of good tracks and cluster energies in the barrel and endcap calorimeters.
- The absolute value of the visible longitudinal momentum balance ( $p_{bal}/E_{vis}$ ) is smaller than 0.4 as shown in Fig.4.3. Here,  $p_{bal}$  represents the sum of momenta of all good tracks and energies of calorimeter clusters along the beam direction.
- Dividing each event into two hemispheres with respect to the plane perpendicular to the thrust[30] axis, the invariant mass of the particles in either hemisphere is greater than 3 GeV/ $c^2$ . The thrust ( $T$ ) and the thrust axis ( $\vec{n}$ ) which are used to divide the event are defined as:

$$T = \max \frac{\sum |\vec{p}_i \cdot \vec{n}|}{\sum |\vec{p}_i|} \quad (4.10)$$

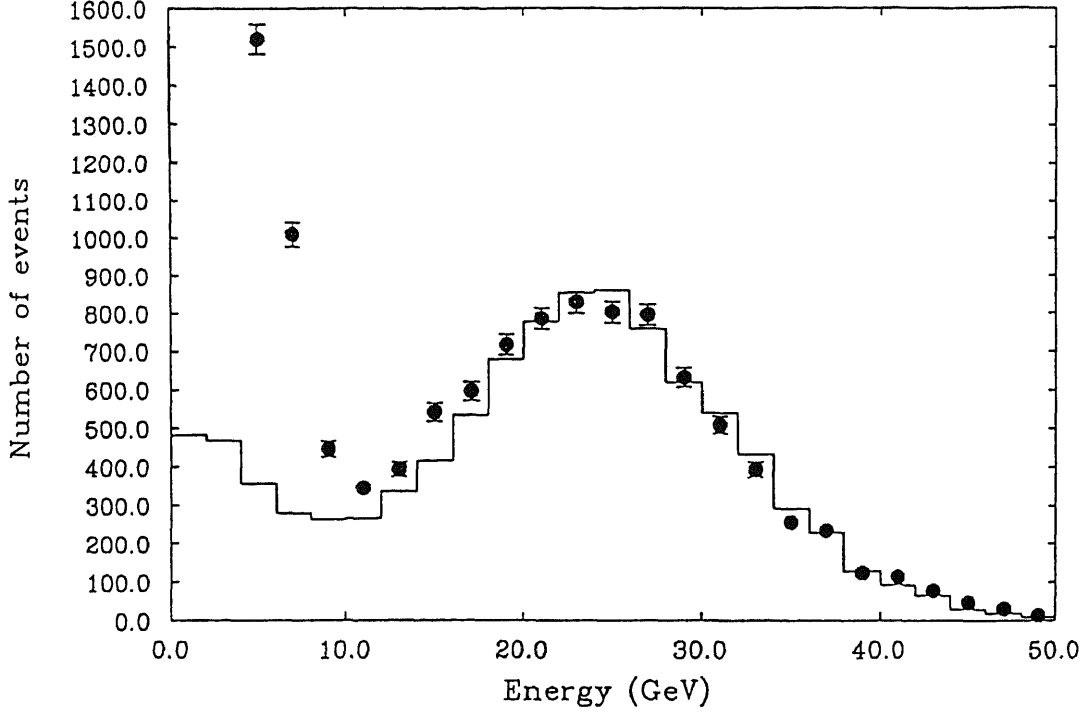


Figure 4.2: *Distribution of the total energy deposit of calorimeters.*

In this calculation of  $T$ , it is assumed that good tracks are those of pions and that energy clusters are those of photons.  $\vec{n}$  is an arbitrary unit vector which is determined to maximize the value of  $T$  and  $\vec{p}_i$  is the momentum of the  $i$ -th good track or the energy of the  $i$ -th cluster.

These selection criteria are the VENUS standard for multi-hadronic events. Furthermore, an additional criterion is used for the event shape and jet clustering analysis which requires that most of the final particles are detected in the fiducial volume of the CDC.

- The polar angle of the thrust axis  $\theta_T$  is within  $|\cos \theta_T| < 0.7$ .

The results of the multi-hadronic event selections at each energy are summarized in Table 4.1. The integrated luminosity and the weighted-mean center-of-mass energy are respectively

$$\int \mathcal{L} dt = 60.6 \pm 0.1(\text{stat.}) \pm 1.6(\text{sys.}) \quad (4.11)$$

$$\langle \sqrt{s} \rangle = 58.4 \text{ GeV} \quad (4.12)$$

| $\sqrt{s}$ (GeV) | Process 2 | Rejected | $E_{cal} \cdot N_{good}$ | $E_{vis}$ | $P_{bal}$ | $M_{jet}$ | $\cos \theta_T$ |
|------------------|-----------|----------|--------------------------|-----------|-----------|-----------|-----------------|
| 54               | 152       | 0        | 151                      | 126       | 120       | 117       | 78              |
| 55               | 290       | 0        | 284                      | 223       | 213       | 212       | 160             |
| 56               | 960       | 0        | 937                      | 752       | 717       | 708       | 519             |
| 56.5             | 145       | 0        | 142                      | 103       | 99        | 96        | 69              |
| 57               | 729       | 219      | 496                      | 386       | 367       | 362       | 265             |
| 57.5             | 18        | 0        | 18                       | 13        | 13        | 12        | 9               |
| 58               | 5767      | 14       | 5631                     | 4284      | 4042      | 4009      | 2891            |
| 58.5             | 191       | 0        | 186                      | 146       | 139       | 139       | 101             |
| 59               | 179       | 0        | 173                      | 130       | 120       | 116       | 83              |
| 59.5             | 20        | 0        | 20                       | 10        | 10        | 10        | 8               |
| 60               | 654       | 21       | 622                      | 468       | 448       | 443       | 315             |
| 60.8             | 869       | 0        | 851                      | 639       | 598       | 592       | 421             |
| 61.4             | 934       | 9        | 898                      | 654       | 615       | 603       | 428             |
| 64               | 278       | 0        | 266                      | 192       | 185       | 179       | 121             |
| Others           | 359       | 23       | 330                      | 245       | 233       | 229       | 159             |
| Total            | 11545     | 286      | 11005                    | 8371      | 7919      | 7827      | 5627            |

Table 4.1: List of events triggered and survived from each selection stage.

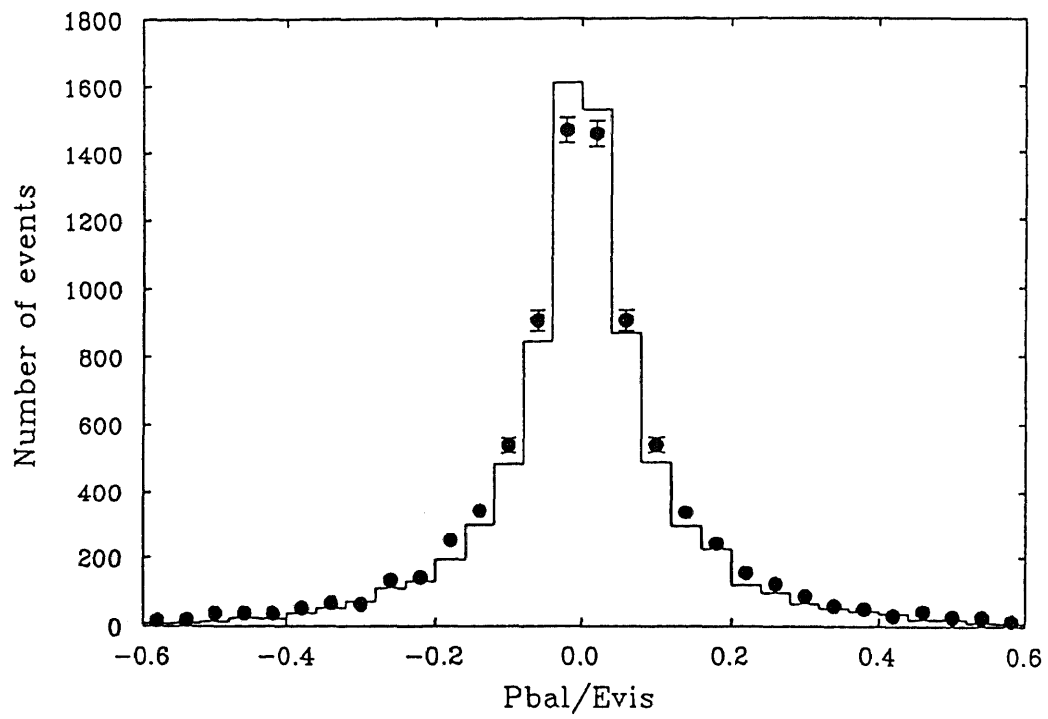


Figure 4.3: *Distribution of the visible longitudinal momentum balance.*



# Chapter 5

## Monte Carlo Simulation

Data analyses were performed by comparing measured data with expectations from theoretical models. An event generator simulates particle productions based on the models. Output data are four momentum information of the produced particles. Since some of the information are inevitably lost in reconstruction, a simulation of the detector performance must be included in order to compare data with Monte Carlo results directly. In order to simulate the response of the VENUS detector and to calculate the detection efficiency, there are two simulator programs called VMONT and VITMIN<sup>1</sup>. For a complete analysis, the full detector simulation program VMONT is used which simulates the particle behaviors in the VENUS detector and produces the detector responses. As the VMONT gives the detector responses in the same format as the real data, which is called the VDS[32] format, tracks and clusters in Monte Carlo events can be reconstructed in the same way as the real data. For a quick analysis, the fast simulation program VITMIN is used, which directly produces expected tracks and clusters for given particles simply by smearing their four momenta from the event generator. Fig. 5.1 shows the flow chart of an analysis using a Monte Carlo simulation program.

### 5.1 Event Generation

Since no calculational methods exist for soft processes such as fragmentations in QCD, some phenomenological models have to be imposed in the simulation. The LUND Monte Carlo program is a fairly classical and well established program[31]. The program package for jet fragmentation and  $e^+e^-$  physics named JETSET is a popular event generator of multi-hadronic events at  $e^+e^-$  colliding experiments. Eight quarks of four generations are originally supported. Here, the JETSET version 6.3 program is adopted in a Monte Carlo simulation of hadronic jet phenomena

---

<sup>1</sup>VENUS Instant Tracer by MINami

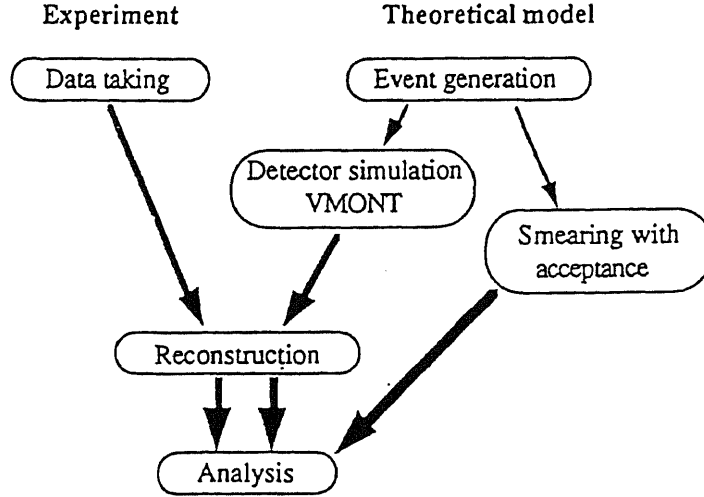


Figure 5.1: *Flowchart of the analysis procedure.*

on account of its good agreement with real data.

The production of a quark and its anti-quark is calculated according to the electroweak theory with radiative and QCD corrections. The radiative correction is performed according to the scheme by Fujimoto et al[33]. The QCD correction is usually performed by the parton shower model (PS) with leading logarithmic approximation. In this scheme, a parton shower develops by successive processes of  $q \rightarrow qg$ ,  $\bar{q} \rightarrow \bar{q}g$ ,  $g \rightarrow gg$  and  $g \rightarrow q\bar{q}$  as shown in Fig. 5.2. The probability for these reactions are proportional to  $\alpha_s$ , which is determined by QCD scale parameter  $\Lambda$ . Since the perturbative treatment becomes impossible in low  $q^2$  region, the cut-off parameter  $Q_0$  for the invariant mass is imposed in emission processes. The parton shower develops until the virtual mass of any parton becomes lighter than  $Q_0$ .

Besides the parton shower model, an alternative correction by a tree-level calculation of the QCD matrix elements (ME) up to  $\alpha_s^2$ -order is possible. In calculating the matrix elements, a cut-off parameter  $y_{min}$  which is the minimum scaled invariant mass between two partons is introduced. These diagrams are shown in Fig. 5.3. The main difference between the ME and PS schemes appears in the fraction of multi-jet events because the ME can not reproduce more than four jets in principle.

A pair of quark and anti-quark generated in an electron positron annihilation are transformed into hadrons through fragmentation processes of quarks. In the energy range of TRISTAN, the average hadron momentum along the original quark direction is large compared with its transverse momentum which is limited to

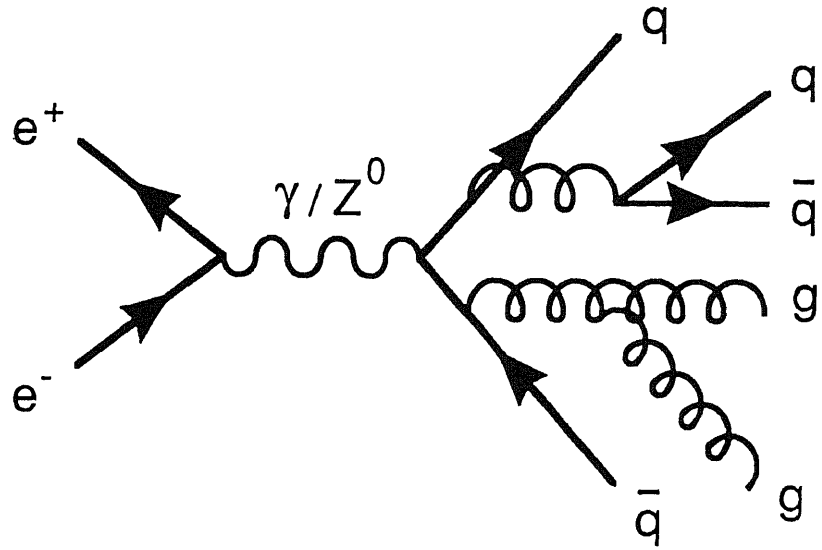


Figure 5.2: *Perturbative QCD correction by a parton shower model.*

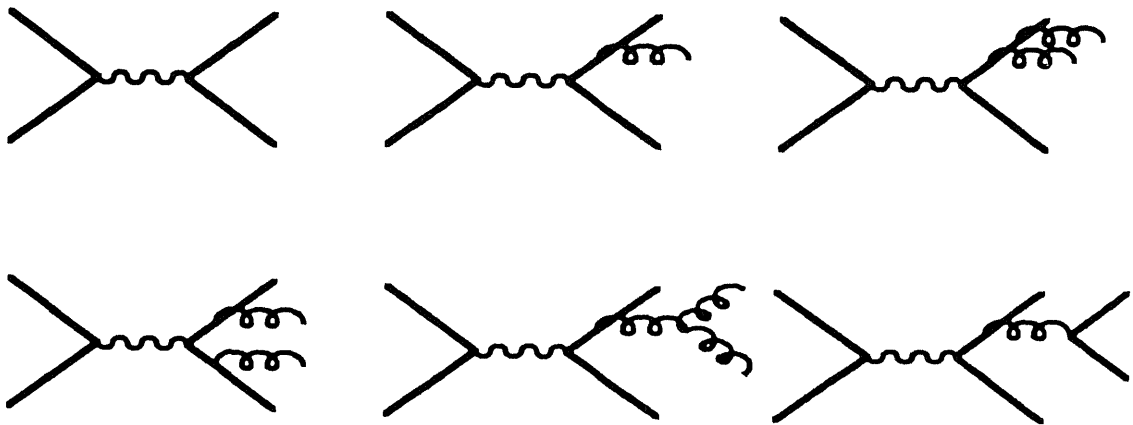


Figure 5.3: *Tree-level QCD diagrams up to second order of  $\alpha_s$ .*

be about 0.5 GeV. Hence, hadrons appear in the form of two jets collimated around the quark axes. Occasionally, when a quark radiates a hard gluon with a large angle, hadrons appear in the form of three jets. This gluon radiation can presumably be described by perturbative QCD. Non-Abelian nature of QCD disables a perturbative approach in low  $q^2$  region, where partons fragment into hadrons. Phenomenological models are used in fragmentation processes. The string fragmentation model is based on the dynamics of a string. Between the partons in a color-singlet system, a one-dimensional string is placed, where a quark is located at the end point and a gluon is located at the intermediate point to be a kink as shown in Fig. 5.4. The relative momentum between the partons determines the tension. The tension breaks the string with generating a new pair of quark and anti-quark at the breaking point. The original parton brings one of the pair and forms a meson. The scaled longitudinal momentum of the hadron  $z$  with respect to the direction of the parton is given by a fragmentation function. The LUND symmetric function has two parameters  $a$  and  $b$ .

$$f(z) = \frac{(1-z)^a}{z} \exp\left(-\frac{bm_t^2}{z}\right) \quad (5.1)$$

where  $m_t = \sqrt{m^2 + p_t^2}$  is the transverse mass of the produced hadron. The transverse momentum of the hadron  $p_t$  is produced independently by a Gaussian distribution with a standard deviation  $\sigma_q$ . The breaking of the string is repeated as far as the string has enough energy to generate a pair of quark and anti-quark. Baryons can be also produced by replacing a  $q\bar{q}$ -pair by a  $(qq)(\bar{q}\bar{q})$ -pair.

There are some parameters to determine the effects of QCD and fragmentation. Since they are correlated each other, they should be treated as a parameter set. As shown in Table 5.1, these parameters were tuned by each experimental group, in addition to the original default values. In this thesis, the parameter set presented by the TASSO Collaboration is adopted. The uncertainties in these parameters are taken into account as systematic errors.

## 5.2 Full Detector Simulator VMONT

The program VMONT accepts momentum vectors of final particles in a hypothetical event which is generated by an event generator and it produces event data which have the same format as that of the calibrated real data. The VMONT supports all the components of the VENUS detector.

Decays of  $\pi^\pm$ ,  $K^\pm$ ,  $K_L^0$  and  $\mu^\pm$  are included in the VMONT. The positions of the decay vertices are calculated even for particles with short lifetimes such as  $K_S^0$ ,  $\Lambda$  and  $D$  mesons as well as ones with long lifetimes. The time of flight is also calculated.

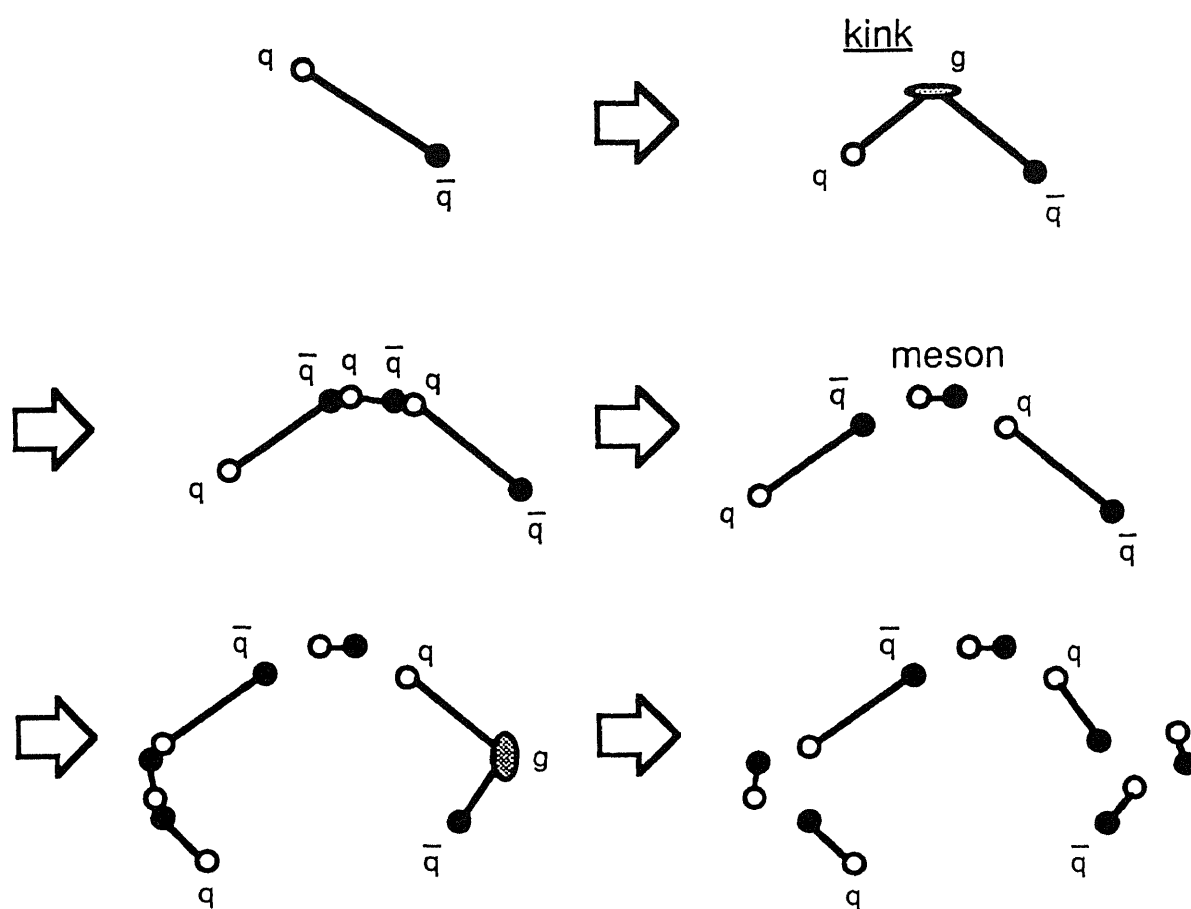


Figure 5.4: *String fragmentation scheme of multi-hadron production.*

| Parameters               | Parton Shower |         |       | Matrix Element |         |       |
|--------------------------|---------------|---------|-------|----------------|---------|-------|
|                          | default       | MARK-II | TASSO | default        | MARK-II | TASSO |
| $\Lambda_{QCD}$ (GeV)    | 0.4           | 0.4     | 0.26  | 0.5            | 0.5     | 0.62  |
| $Q_0$ (GeV)              | 1.0           | 1.0     | 1.0   | -              | -       | -     |
| $y_{min}$                | -             | -       | -     | 0.02           | 0.015   | 0.02  |
| $a$                      | 0.5           | 0.45    | 0.18  | 1.0            | 0.9     | 0.58  |
| $b$ (GeV <sup>-2</sup> ) | 0.9           | 0.90    | 0.34  | 0.7            | 0.70    | 0.41  |
| $\sigma_q$ (GeV)         | 0.35          | 0.33    | 0.39  | 0.4            | 0.33    | 0.40  |

Table 5.1: *Parameter-sets for the JETSET version 6.3.*

Multiple coulomb scattering, energy loss, nuclear interactions and electromagnetic cascade showers in the detector are simulated on the actual geometry and materials coded in the program. Electromagnetic showers in the calorimeters originating from electrons and/or photons are simulated by EGS4. The calorimeter responses are obtained by using the information from the EGS4. The nuclear absorption and responses of the calorimeters for hadrons and muons are also calculated on the basis of the beam test data.

The chamber responses are simulated by the relation between the drift time and the drift distance. The resolution of each chamber is also taken into account. The simulation of detector responses is optimized by studying actual responses of each chamber.

In addition, the VMONT can incorporate simulations of the hardware trigger systems.

### 5.3 Fast Simulator VITMIN

Since the program VMONT is required to simulate the entire responses of the VENUS detector in the shortest possible time interval, the interactions of particles with the VENUS detector and/or other reactions such as decay in flight are traced in short steps, but many Monte Carlo calculations are needed. Therefore, a long calculation time is needed for the VMONT. For example, in order to simulate a process of  $e^+e^- \rightarrow \text{hadrons}$  at  $\sqrt{s} = 58$  GeV, it takes a few second per event by FACOM M780/30. In addition, a similar amount of time is needed to reconstruct charged tracks in the CDC. Therefore, it is difficult to pursue an analysis method like parameter tuning when a large number of events have to be generated.

In the program VITMIN, the interactions and/or other reactions of particles are calculated in long steps and done analytically as quick as possible. The VITMIN simulates only three detector components; i.e. the CDC, LG and LA. Decays of  $\pi^\pm$ ,  $K^\pm$ ,  $K_L^0$  and  $\mu^\pm$  and positions of decay vertices for particles with shorter lifetimes are also taken into account.

### Simulation of the CDC part

In this part, only charged stable particles are treated. The momentum of a particle is smeared according to the finite resolution of the CDC given in Eq. 3.2. Then some particles are rejected as a function of opening angles for closely emitted particles with similar momenta. Hence the efficiency of the track reconstruction program of the VMONT can be estimated. Track reconstruction is not incorporated in this program.

### Simulation of the LG and LA parts

Calculations are done for all stable particles except for neutrinos. Energy deposits by electromagnetic showers are calculated in terms of the Gaussian distribution with their resolution given in Eqs. 3.3 and 3.4. Other interactions are calculated by the same routines as in the VMONT. After these calculations, energy deposits spaced very closely are merged in one cluster.

The VITMIN is a few hundred times faster than the VMONT in CPU time and calculated values are in good agreement with those by the VMONT regarding certain shape variables such as thrust, sphericity and acoplanarity.





# Chapter 6

## Muon Identification

The performance of particle identification can be evaluated by the detection efficiency of a particle of interest and by misidentification probabilities of unwanted particles. The misidentification probability of hadrons should be, of course, small. Identification of a muon in a simple final state is straightforward. However, when a muon is produced together with other stable background particles in a multi-hadronic final state, some difficulties arise. Detection of the muon is carried out by the muon detector system located at the outermost part of the VENUS detector.

### 6.1 Identification Procedure

Muons can be characterized by the nature of high penetrability through matters. Multiple coulomb scattering, energy loss and magnetic bending complicate muon trajectories in the muon detector. Therefore, the match between an extrapolated CDC track and a local track which is reconstructed from hit points in the muon detector becomes important in the muon track reconstruction.

#### 6.1.1 CDC track extrapolation

The track extrapolation procedure is applied only to good tracks defined in Chapter 4. (See page 42.) The barrel muon detector system covers an angular range of  $|\cos \theta| \leq 0.75$ . Tracks whose polar angles are in this range are taken into account. Each CDC track of interest is extrapolated to the muon detector in steps of ten radiation lengths while expected bending in the magnetic field in the solenoid and the return yoke,  $dE/dx$  losses and multiple coulomb scattering are taken into account. In these extrapolation processes, tracks are treated to be muons.

The primary contribution to the extrapolation error comes from multiple coulomb scattering in the LG ( $\sim 18.0X_0$ ), the return yoke ( $\sim 17.0X_0$ ) and the iron filters ( $\sim 11.4X_0/\text{layer}$ ).

|            | momentum (GeV/c) |     |     |      |
|------------|------------------|-----|-----|------|
|            | 2.0              | 4.0 | 8.0 | 16.0 |
| 1-st layer | 9.4              | 4.4 | 2.2 | 1.1  |
| 2-st layer | 9.7              | 4.5 | 2.2 | 1.2  |
| 3-st layer | 11.8             | 5.5 | 2.6 | 1.4  |
| 4-st layer | 12.2             | 5.6 | 2.7 | 1.4  |
| 5-st layer | 13.9             | 6.7 | 3.2 | 1.6  |
| 6-st layer | 14.4             | 6.8 | 3.3 | 1.7  |
| 7-st layer | 17.1             | 7.8 | 4.1 | 2.7  |
| 8-st layer | 17.6             | 7.9 | 4.1 | 2.7  |

Table 6.1: *Typical value of extrapolated deviation (cm) due to multiple coulomb scattering.*

The rms scattering angle  $\theta_0$  can be written in the Gaussian approximation[34] as

$$\theta_0 = \frac{14.1}{p\beta} \sqrt{\frac{L}{L_R}} \left( 1 + \frac{1}{9} \log \frac{L}{L_R} \right) \quad (6.1)$$

where  $\theta_0$  is in radians,  $p$  is the momentum in MeV/c and  $\beta$  is the velocity in units of  $c$  of the incident particle.  $L/L_R$  is the thickness in radiation length of the scattering medium. The rms position deviation projected in one dimension after passing through material of thickness  $t_0$  and drift space of  $d_0$ [35] is given by

$$\sigma_0 = \theta_0 \sqrt{\frac{t_0^2}{3} + t_0 d_0 + d_0^2} \quad (6.2)$$

In the VENUS detector, a particle traverses several detector elements. The scattering effects of each element are independent and the contribution can be added in quadrature. In a given layer of the muon drift tubes, the mean-squared positional error  $\sigma_{mcs}^2$  is expressed as the quadratic sum of each positional deviation. The typical positional errors for muons of 2, 4, 8 and 16 GeV/c are listed in Table 6.1.

The rest of the extrapolation error is due to the deviation of the CDC tracking and the spatial resolution of the muon detector. According to the Monte Carlo simulation, the spatial deviation of the CDC extrapolation in the  $r - \phi$  plane  $\sigma_{CDC}$  is about 4 mm. The spatial resolution of the muon detector  $\sigma_{mu}$  is estimated by cosmic ray test[36] to be 1.3 mm. The total extrapolation error  $\sigma_{ex}$  is expressed as follows:

|            | Momentum (GeV/c) |     |     |      |
|------------|------------------|-----|-----|------|
|            | 2.0              | 4.0 | 8.0 | 16.0 |
| 1-st layer | 0.1              | 0.1 | 0.1 | 0.1  |
| 2-st layer | 0.1              | 0.1 | 0.1 | 0.1  |
| 3-st layer | 1.5              | 0.5 | 0.2 | 0.1  |
| 4-st layer | 1.8              | 0.6 | 0.3 | 0.1  |
| 5-st layer | 4.1              | 1.4 | 0.6 | 0.3  |
| 6-st layer | 4.6              | 1.5 | 0.6 | 0.3  |

Table 6.2: Typical value of the weight at the local track reconstruction  $\sigma_{lo}$  (cm).

$$\sigma_{ex}^2 = \sigma_{mcs}^2 + \sigma_{CDC}^2 + \sigma_{mu}^2 \quad (6.3)$$

### 6.1.2 Local tracking

A certain window has to be set along an extrapolated track to pick up a set of correct hit points in the muon detector. Position deviations between an extrapolated track and observed hit points are given by  $\sigma_{ex}$ . The window is taken with the value of  $\pm 3\sigma_{ex}$  around the extrapolated track. The number of layers which contain hit points of the muon tubes should be at least four out of six. The track fit is carried out by selecting one hit for each hit layer with all left-right ambiguity combinations and the reduced  $\chi^2$  of each local track is calculated. When there are  $N$  hit points used for the fit, the number of degrees of freedom  $\nu$  is given by  $N - 2$  and the reduced  $\chi_\nu^2$  is obtained by

$$\chi_\nu^2 = \frac{1}{N - 2} \cdot \sum_{i=1}^N \frac{\Delta r_i^2}{\sigma_{lo}^2} \quad (6.4)$$

where  $\Delta r_i$  is the deviation of the measured drift distance of the  $i$ -th hit point from the estimated distance of the local track.  $\sigma_{lo}$  is given by

$$\sigma_{lo}^2 = \sigma_{mcs}'^2 + \sigma_{mu}^2 \quad (6.5)$$

where  $\sigma_{mcs}'$  is the spatial deviation due to multiple coulomb scattering from the iron filter. Typical values of  $\sigma_{lo}$  are listed in Table 6.2.

In order to evaluate the goodness of the fit, the integrated probability  $P(\chi_\nu^2, \nu)$  of each local track is calculated. The local track must satisfy the following condition:

$$P(\chi_\nu^2, \nu) \leq 0.997 \quad (6.6)$$

This limit corresponds to three standard deviations in a Gaussian distribution.

### Track quality selection: Matching of tracks and amount of penetrated materials

The angle difference in the  $r-\phi$  plane between the extrapolated track and the local track at the outer surface of the return yoke is adopted to evaluate the connection quality. The angular deviation at the outer surface of the return yoke is determined to be as follows:

$$\theta_{dev}^2 = \theta_{mcs}^2 + \theta_{CDC}^2 + \theta_{lo}^2 \quad (6.7)$$

where  $\theta_{mcs}$  is the angular deviation due to multiple coulomb scattering of the track extrapolation given in Eq. 6.1 caused by all the materials except for iron filters.  $\theta_{CDC}$  is the angular deviation of CDC extrapolation which is negligible and  $\theta_{lo}$  is that due to multiple coulomb scattering in the iron filters. A distribution of the normalized angular difference  $\Delta\theta/\theta_{dev}$  is shown in Fig. 6.1. The track matching condition is required to be:

$$\frac{\Delta\theta}{\theta_{dev}} < 3 \quad (6.8)$$

A muon whose momentum is above a few GeV/c can penetrate the materials of the inner detector components. If a particle penetrates through the barrel muon system, it passes through at least 5.3 absorption lengths of materials. The amount of materials along the extrapolated track and the local track is calculated by taking into account  $dE/dx$  energy loss. It is required that the track must pass through the amount of materials more than 5.3 absorption lengths in total.

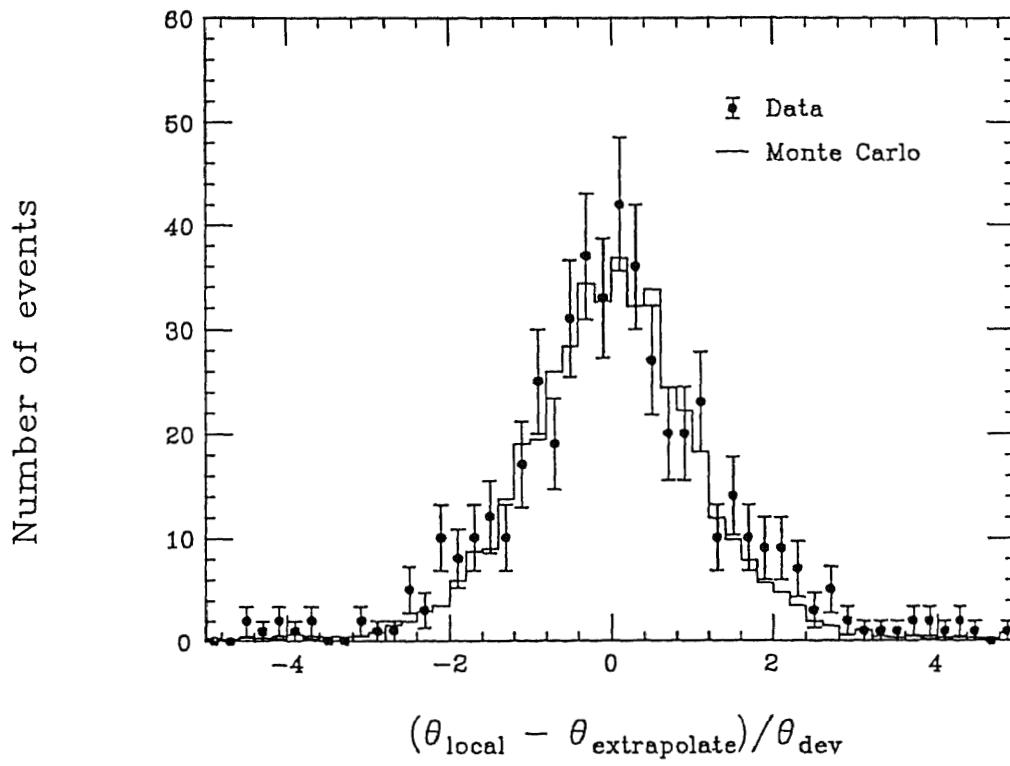
The track which satisfies the above criteria is denoted as a candidate track. If there is no candidate track and if the number of hit layers is larger than four, one of the hit layers is discarded and the local track fit and the track quality selection with the other hit layers are carried out.

### Selection of the most likely track

If there are some candidate tracks, the overall reduced  $\chi_{overall}^2$  is calculated and the most likely track is decided by comparing the integrated probability.  $\chi_{overall}^2$  is defined by replacing  $\sigma_{lo}$  with  $\sigma_{ex}$  in Eq. 6.4 as follows:

$$\chi_{overall}^2 = \frac{1}{N-2} \cdot \sum_{i=1}^N \frac{\Delta r_i^2}{\sigma_{ex}^2} \quad (6.9)$$

The track which gives the minimum value of  $P(\chi_{overall}^2, \nu)$  is the most likely track and selected as the muon candidate track.

Figure 6.1: *Normalized angular difference.*

## 6.2 Efficiency and Backgrounds

### 6.2.1 Detection efficiency of an isolated muon

The detection efficiency with the cuts introduced in the previous section and the overall efficiency were estimated both by the muon sample and by the simulated single muon events with the detector simulation program VMONT.

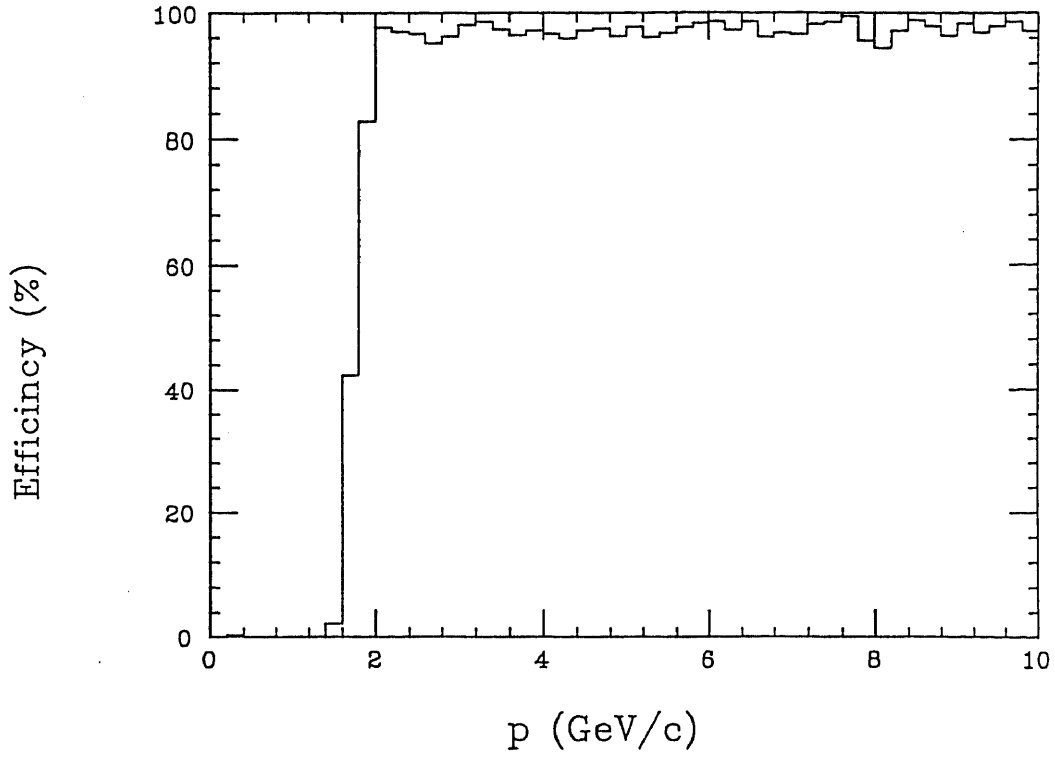
#### Muon selection without the muon detector

In order to estimate the efficiency by using the real events, muon tracks must be identified without using the muon detector. It can be done for the low multiplicity events such as  $\mu\mu$  or  $\mu\mu\gamma$  events with center-of-mass energies between 54 and 64 GeV corresponding to an integrated luminosity of  $60.8 \text{ pb}^{-1}$ . The criteria of this muon pre-selection are as follows:

1. Number of charged tracks is equal to 2.
2. Both tracks must be good tracks.
3.  $|\cos \theta| \leq 0.81$
4. Time-of-flight difference is not larger than 5 ns.
5. Both track momenta must be larger than 2.5 GeV/c to penetrate materials which are placed inside the muon detector.
6. Energy sum of the clusters around the track within  $10^\circ$  must be the minimum ionizing energy, not larger than 1.5 GeV.
7. Two charged tracks have opposite charges.

The cut value of the track momentum is determined from Fig. 6.2 which shows the momentum dependence of the muon identification described in the previous section. The decrease in the low momentum region is due to the material thickness to be penetrated, which determines the overall efficiency. The result of this muon selection is listed in Table 6.3. The procedure of the muon identification in the previous section resulted in 1122 events as di-muon events and 653 events as single muon events among these final 2112 events,

Fig. 6.3 shows the polar angle dependence of the efficiency. Points with error bars show the data of the low multiplicity events and the histogram shows the result of a Monte Carlo simulation. From this distribution the fiducial region of the muon identification is determined to be  $|\cos \theta| \leq 0.6$ . The decrease of about 5 % in the fiducial region comes from the background of the above muon pre-selection procedure.

Figure 6.2: *Momentum dependence of the efficiency of the muon identification.*

| Cut                    | Number of survived events |
|------------------------|---------------------------|
| Total number of events | 49637                     |
| Good track selection   | 32986                     |
| $ \cos \theta  < 0.81$ | 32876                     |
| TOF difference         | 31665                     |
| Momentum               | 7113                      |
| Energy deposit         | 2122                      |
| Track charge           | 2112                      |

Table 6.3: *Muon selection without the muon detector.*

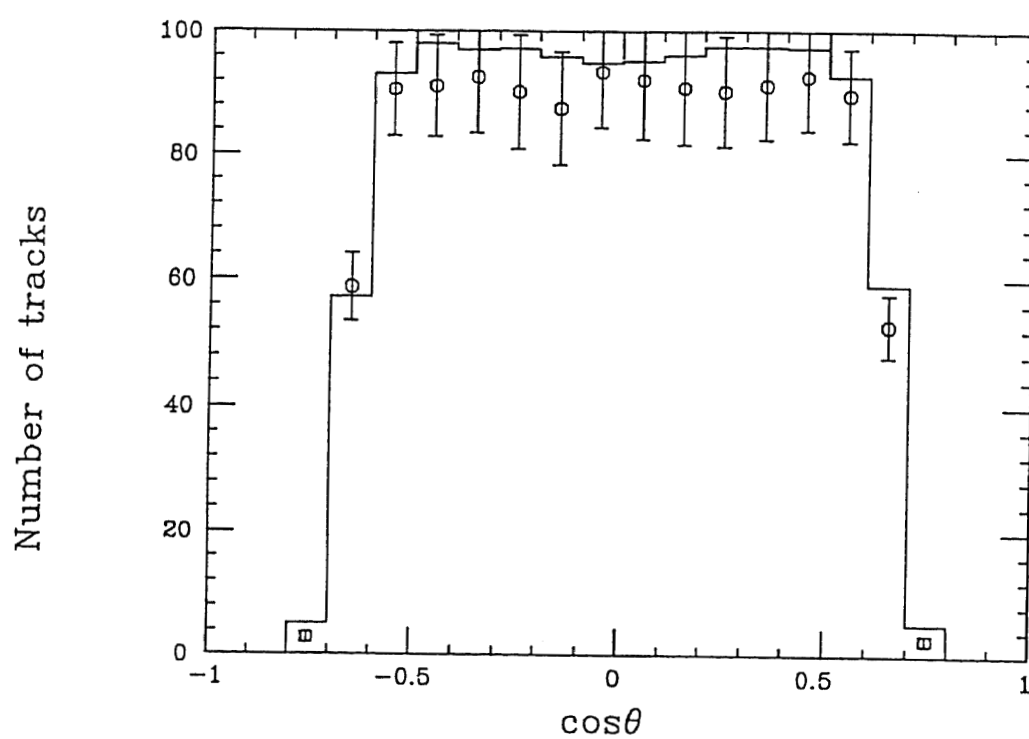


Figure 6.3: Angular dependence of the efficiency of the muon identification.



### 6.2.2 Efficiency for muon identification in multi-hadronic events

The previous identification procedure can be applied to the multi-hadronic event sample. Total 533 muon candidates were selected from 7827 multi-hadronic events with center-of-mass energies between 54 and 64 GeV corresponding to the integrated luminosity of  $60.8 \text{ pb}^{-1}$ .

Since there are many hadrons in multi-hadronic events, it is difficult to eliminate their contamination to the muon candidate completely. In fact, the efficiency for tagging muons is degraded because of the misassociation of tracks and the confusing of hit points of the CDC in a jet. The total detection efficiency of the muon identification in the multi-hadronic events can be estimated by the Monte Carlo calculation if the responses of the VENUS detector were simulated precisely.

The track-misassociation probability can be estimated by using  $\mu\mu$  and  $\mu\mu\gamma$  events which are superimposed in multi-hadronic events. A sample of a superimposed event is shown in Fig. 6.4. In Fig. 6.4(c), the 18-th and 19-th tracks are the superimposed muon tracks found in Fig. 6.4(a). The track-misassociation probability is estimated to be about 5 % which is consistent with the result of a Monte Carlo simulation. The track-misassociation occurs mainly due to the spatial resolution of the CDC.

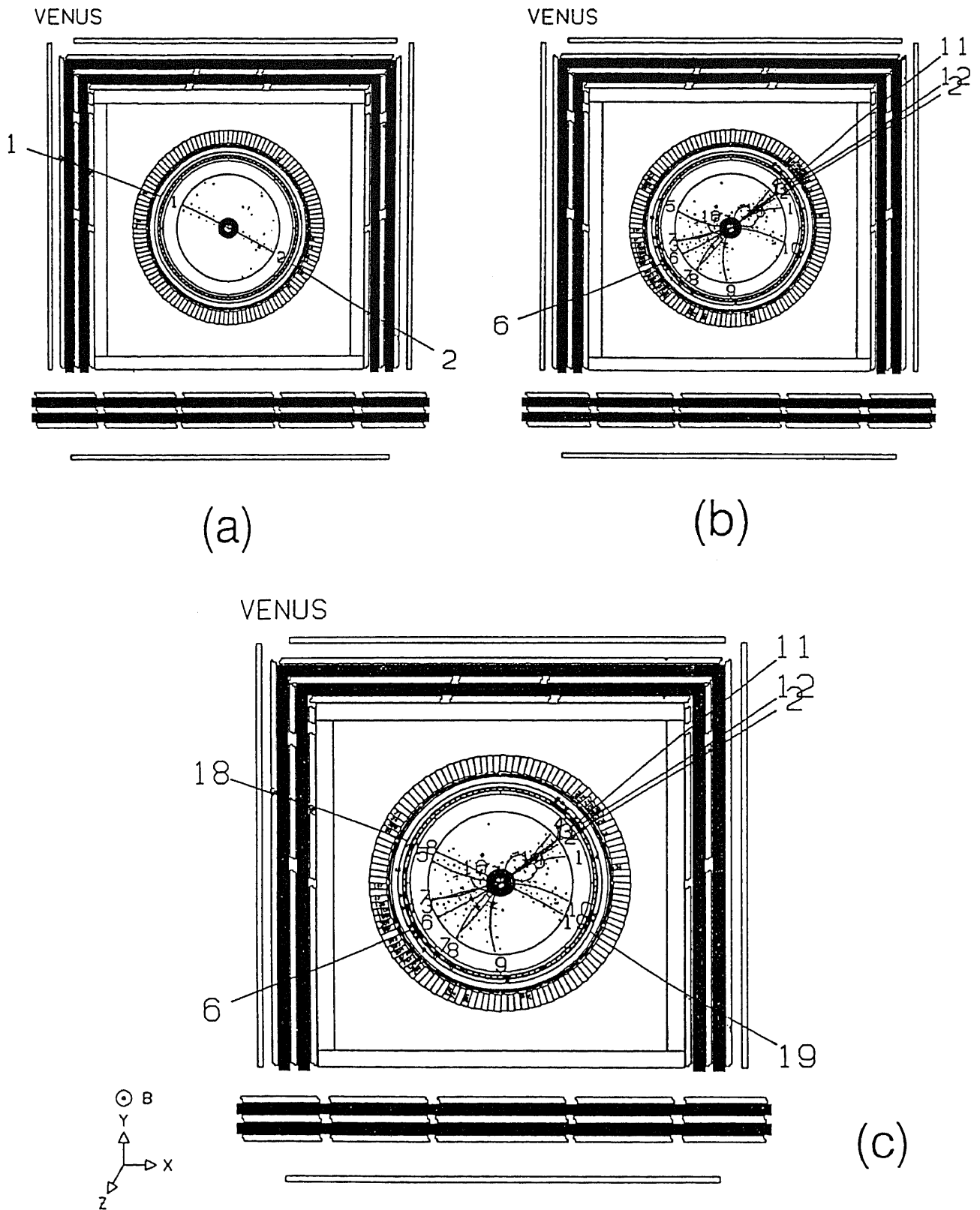


Figure 6.4: A sample of a superimposed event; (a)  $\mu$ -pair production event, (b) a multi-hadronic event and (c) a superimposed event.

# Chapter 7

## Procedure of Measurements

In the theory of electroweak interactions, interference of the vector and axial-vector currents can result in a cross section for  $e^+e^- \rightarrow q\bar{q}$  which is asymmetric with respect to the cosine of the angle between the  $e^-$  and  $q$  directions. The forward-backward asymmetry which is defined as:

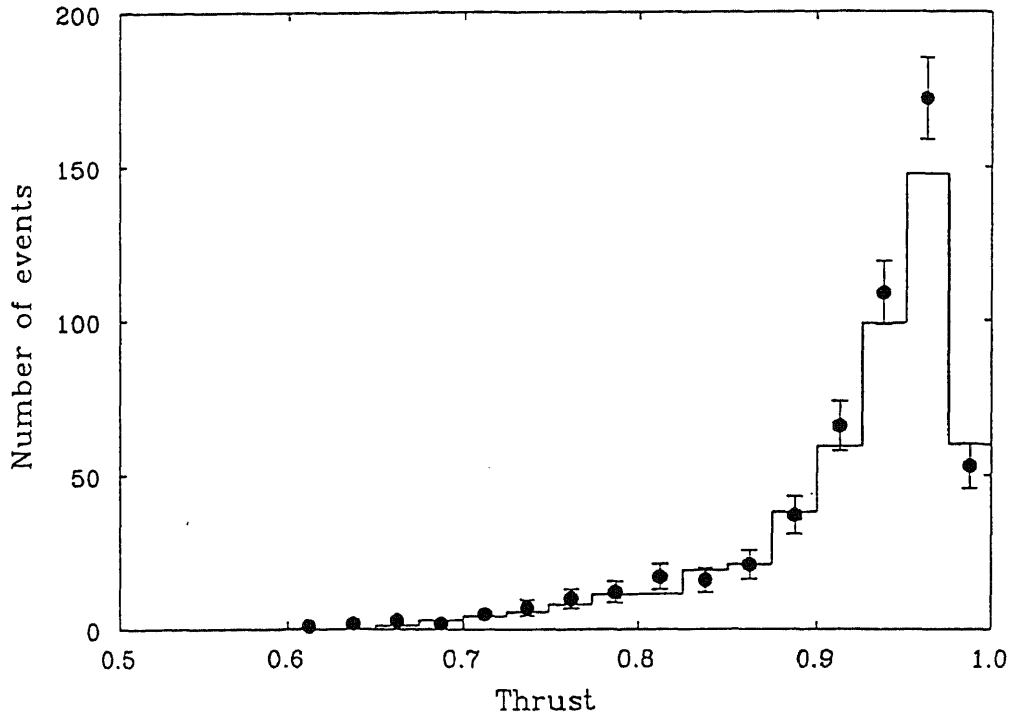
$$A_{FB} = \frac{\sigma_F^q - \sigma_B^q}{\sigma_F^q + \sigma_B^q} \quad (7.1)$$

arises from the difference between the left-handed and right-handed couplings. It can be measured in the case of heavy quarks by using leptons from semi-leptonic decays of  $c$  and  $b$  hadrons to tag the quark charge although a correction must be made to account for  $B-\bar{B}$  mixing, which brings about incorrect charge assignment in a certain fraction of events.

There are 533 muon inclusive multi-hadronic events collected by the VENUS detector at center-of-mass energies around 58 GeV. Muons are identified in hadronic jets. The transverse momentum  $p_t$  of the muon with respect to the jet direction is used to select the contributions of  $b\bar{b}$  pair production events.

### 7.1 Jet Reconstruction

Jets are constructed using all good charged tracks and neutral electromagnetic energy clusters in an event. In order to get the initial quark direction, two methods are tested here. In this section, it is assumed that good tracks are those of pions and that energy clusters are those of photons.

Figure 7.1: *Thrust distribution.*

### Thrust axis

The thrust ( $T$ ) and thrust axis ( $\vec{n}$ ) which are often used to describe an event shape are defined in Chapter 4, namely

$$T = \max \frac{\sum |\vec{p}_i \cdot \vec{n}|}{\sum |\vec{p}_i|} \quad (7.2)$$

where  $\vec{n}$  is an arbitrary unit vector to be determined to maximize the value of  $T$  and  $\vec{p}_i$  is the momentum of the  $i$ -th good track or the energy of the  $i$ -th cluster. When the thrust has a value near 1, the event shape is expected to be collinear. On the other hand, when it has a value near 0.5, the shape is expected to be spherical or planar. The thrust distribution is shown in Fig. 7.1. Points with error bars show the data and the histogram shows the result of a Monte Carlo simulation for the multi-hadronic events. The number of events of the histogram is normalized for the integrated luminosity of the data. The Monte Carlo simulation agrees with the data and the thrust axis can be used to approximate the quark direction as shown in Fig. 7.2.

The polar angle difference between the thrust direction and the quark direction obtained by the Monte Carlo program is plotted in Fig. 7.3. As shown in this figure, the thrust axis is close to the quark direction for high thrust events. Deviated

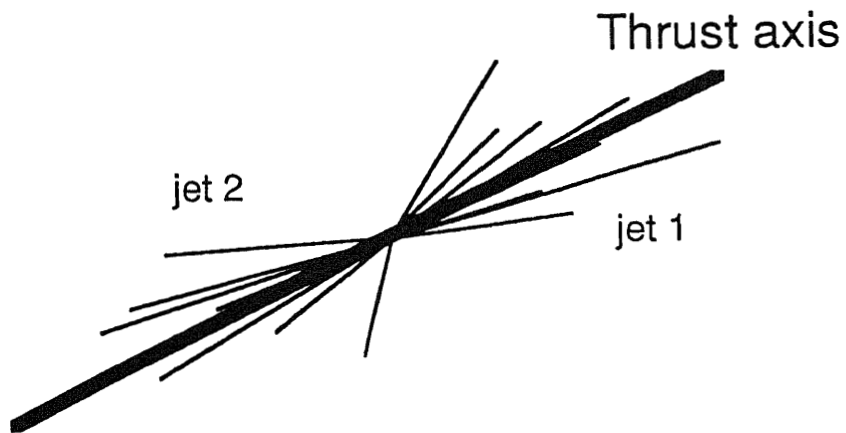


Figure 7.2: Schematic illustration of the thrust.

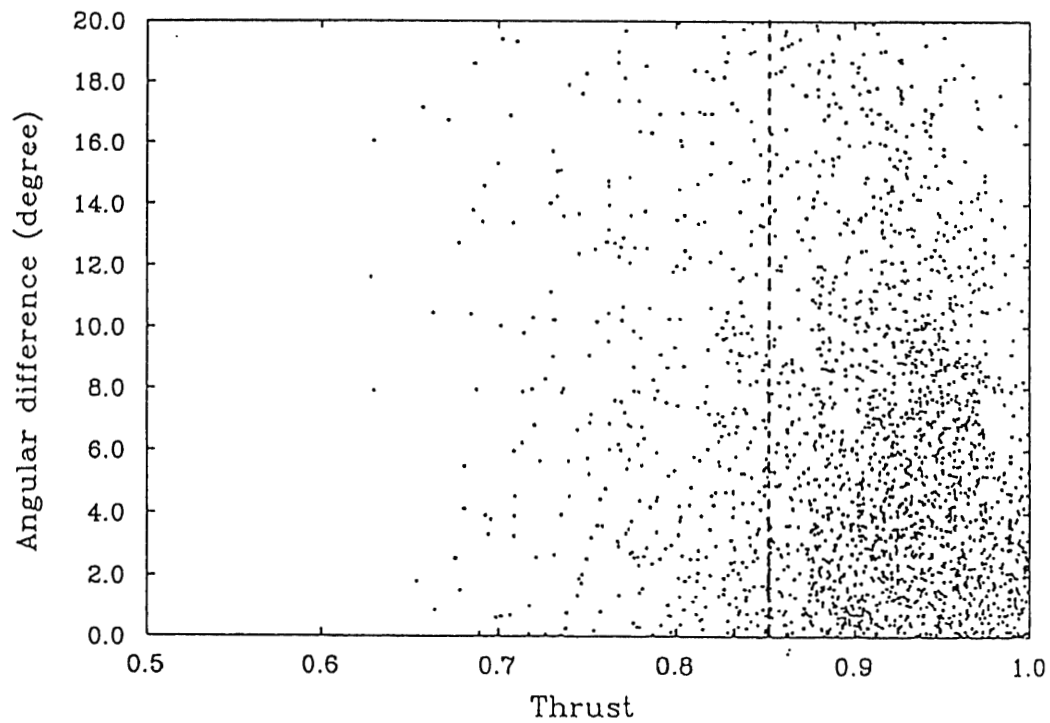


Figure 7.3: Thrust value vs. the polar angle difference between the thrust axis and quark direction.

points are mainly due to initial photon radiation and also due to three-jet events in which hard gluons are emitted with large opening angles. As for such spherical events, event axes are difficult to be determined correctly because the quark is kicked away from the original direction. When the thrust axis is used as the quark direction, the two-jet event selection should be applied because the event must be a two-jet event whose jet axes go back-to-back each other. To select back-to-back two-jet events, the following criterion is imposed:

- Events are required to have thrust values over 0.85.

This reduces the number of events with higher jet-multiplicities; i.e.,  $e^+e^- \rightarrow q\bar{q}g, q\bar{q}gg$  and so on. Distributions of the polar angle differences for the high thrust and low thrust regions are shown in Fig. 7.4. In the high thrust region, the thrust axis is very close to the quark direction.

It should be noted that the thrust axis provides no information of the initial quark charge. This information can be found in the lepton charge. In the present case, it is the muon charge when the muon is produced through semi-leptonic decay processes. The polar angle of the initial  $b$ -quark is determined by

$$\cos \theta_b = -1 \times |\cos \theta_T| \times Q_\mu \times \text{sgn}(p_z) \quad (7.3)$$

where  $\theta_T$  is the polar angle of the thrust axis,  $Q_\mu$  is the charge of the muon and  $\text{sgn}(p_z)$  is a function which has a value +1 or -1 according to the direction of the muon with respect to the  $z$  axis.

## Jet clustering method

In order to find the jet axis, two well known methods are often used; D-join and Y-cut methods. Notice that tracks of leptons are ordinarily excluded in these procedures of jet-axis determination except for  $E_{det}$  which is defined in the Y-cut method.

The jet clustering procedure of the D-join method is as follows:

1. Find the smallest  $D_{ij}$  value which is defined as:

$$D_{ij} = \frac{m_{ij} \sqrt{p_i p_j}}{p_i + p_j} \quad (7.4)$$

where  $m_{ij}$  is the invariant mass, and  $p_i$  and  $p_j$  are the momenta of the  $i$ -th and  $j$ -th tracks or clusters, respectively.

2. Combine the  $i$ -th and  $j$ -th tracks or clusters.
3. Iterate (1) and (2) while the  $D_{ij}$  value is smaller than a given cut value.

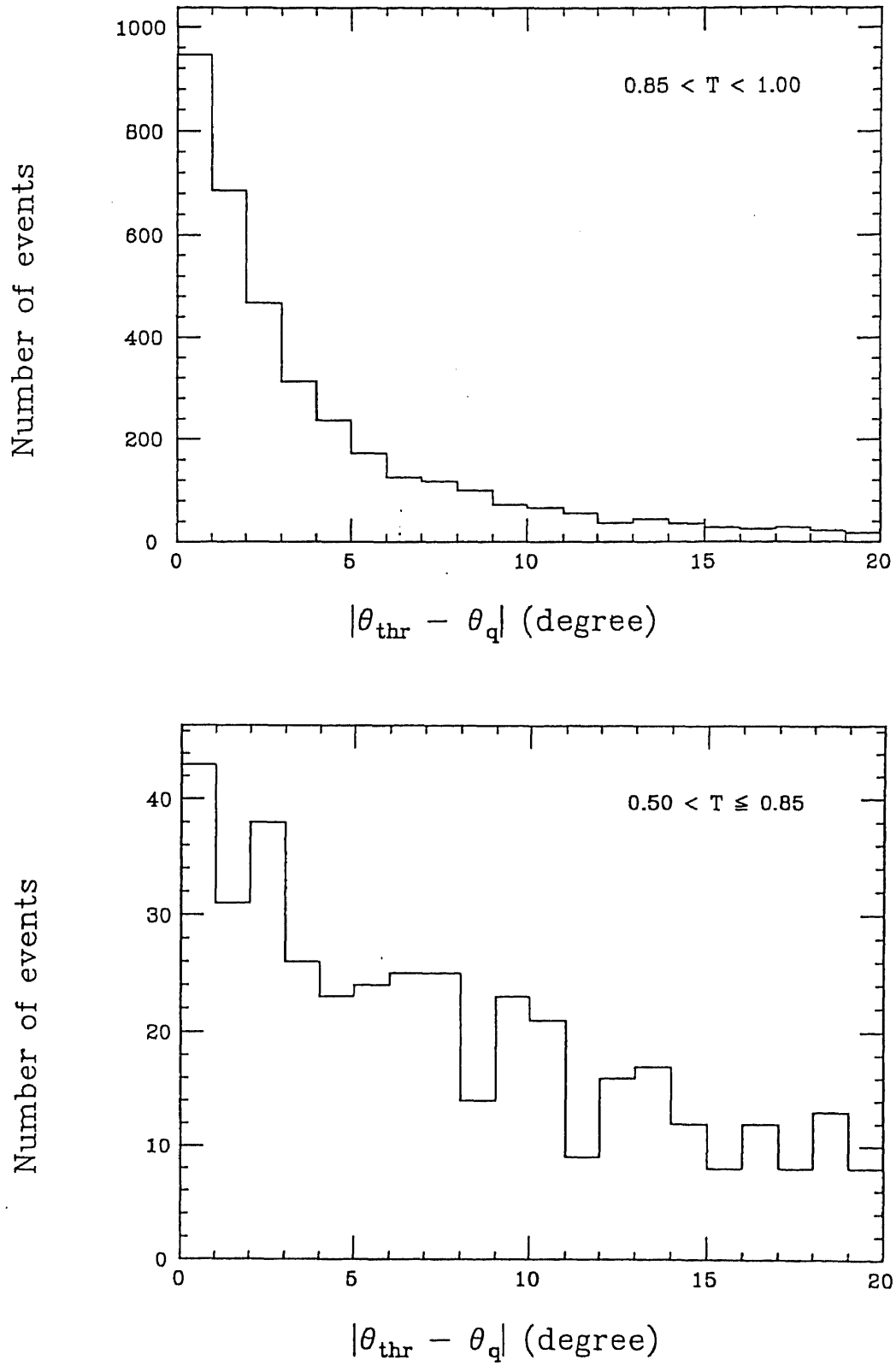


Figure 7.4: Polar angle difference between the thrust axis and quark direction.

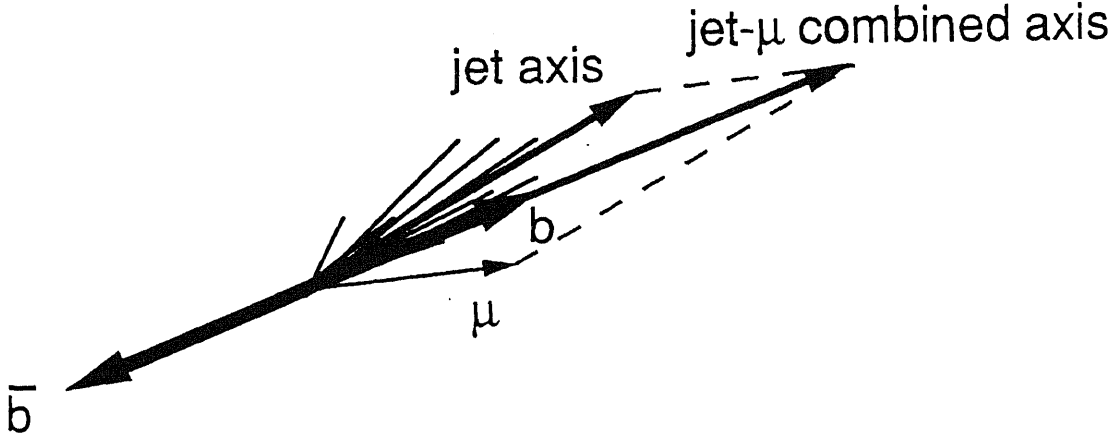


Figure 7.5: Schematic image of the jet-muon combined axis.

And the jet clustering procedure of the Y-cut method is similar to the above as follows:

1. Find the smallest  $Y_{ij}$  value which is defined as:

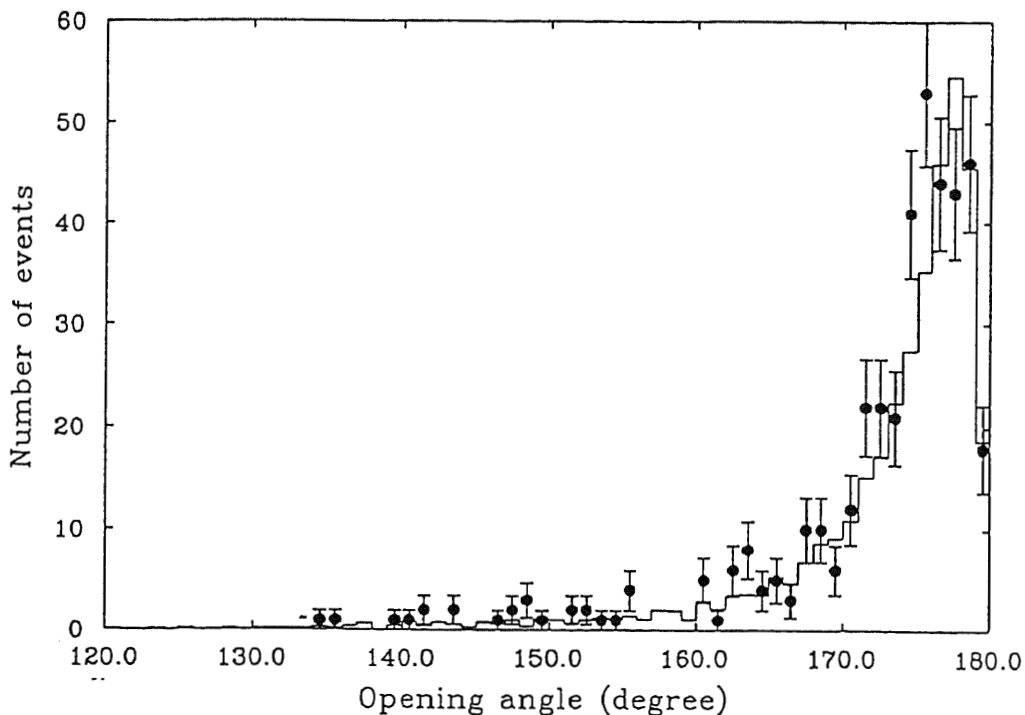
$$Y_{ij} = \frac{m_{ij}^2}{E_{det}^2} \quad (7.5)$$

where  $m_{ij}$  is the invariant mass of the  $i$ -th and  $j$ -th tracks or clusters and  $E_{det}$  is the detected energy including leptons.

2. Combine the  $i$ -th and  $j$ -th tracks or clusters.
3. Iterate (1) and (2) while the  $Y_{ij}$  value is smaller than a given cut value.

Here, the Y-cut method was adopted for jet clustering and the Y-cut value was determined to be 0.80. Only two-jet events are taken into account. Fig. 7.5 shows that the opening angle between two jets is very close to  $180^\circ$  and the jets almost go back-to-back. A jet which is closer to the muon track is called 'jet1' and regarded as the origin of the muon. The other jet is called 'jet2'. The initial quark direction is determined by the combination of the jet1 direction and the muon direction because the jet1 axis seems to be kicked from the initial direction by emitting the muon as shown in Fig. 7.6. The quark charge is determined to be the same as the muon charge. If the muon has a positive charge, the combined axis looks toward the  $\bar{b}$ -direction.



Figure 7.6: *Opening angle between jets.*

Both the thrust axis and the jet-muon combined axis represent the initial quark directions well. Fig. 7.7 shows the polar angle differences calculated by the Monte Carlo program with respect to the initial  $b$ -quark. The solid and dashed histograms represent the polar angle differences for the thrust axis and the combined axis, respectively. The thrust axis seems to be a better approximation of the initial quark direction. In the present analysis, the thrust axis method is adopted.

## 7.2 $b\bar{b}$ Pair Production Enhancement

Muon inclusive multi-hadronic events consist of quark-pair productions of five flavours. All events but  $b\bar{b}$  pair production become backgrounds. The hadronization and decay products from two  $b\bar{b}$  jets are well separated in space to facilitate a cleaner study of  $b$  physics.

Tagging of heavy flavours using high  $p_t$  leptons from semi-leptonic decays has been one of the most important techniques in the recent years. The  $p_t$  of a charged lepton is estimated with respect to a  $b$ -quark direction which is considered to be represented either by the thrust axis or by the resultant direction of the charged lepton and the nearest  $b$ -quark left-over jet. The  $p_t$  distributions are similar in these two cases, except for the effects of three or more jet events in which sometimes

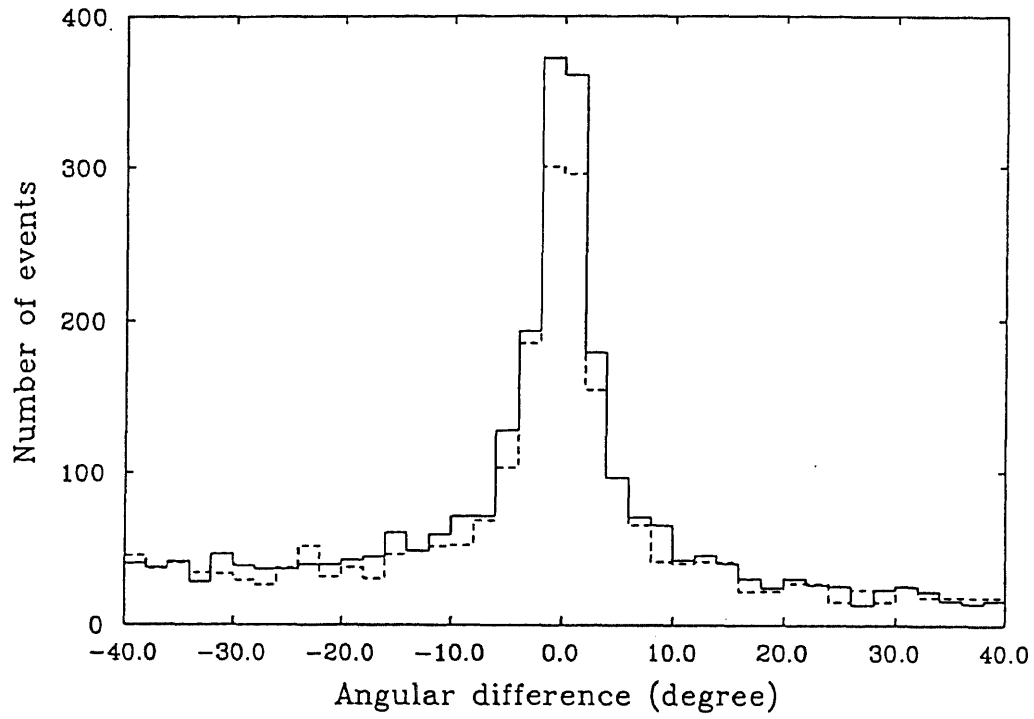


Figure 7.7: Polar angle difference with respect to the quark direction; the solid histogram for the thrust axis method and the dashed histogram for the jet-muon combined axis method.

| $p_t$ (GeV) | Thrust     |            | Jet clustering |            |
|-------------|------------|------------|----------------|------------|
|             | Candidates | Purity (%) | Candidates     | Purity (%) |
| No cut      | 440        | 17.8       | 394            | 18.8       |
| 0.5         | 284        | 25.7       | 230            | 28.6       |
| 0.6         | 231        | 29.2       | 202            | 32.4       |
| 0.7         | 201        | 32.6       | 171            | 35.6       |
| 0.8         | 171        | 36.3       | 150            | 39.7       |
| 0.9         | 145        | 38.3       | 133            | 43.1       |
| 1.0         | 133        | 41.0       | 115            | 45.5       |
| 1.1         | 116        | 44.0       | 99             | 47.8       |
| 1.2         | 95         | 47.2       | 84             | 50.6       |
| 1.3         | 88         | 49.1       | 77             | 51.7       |
| 1.4         | 75         | 49.1       | 70             | 50.1       |
| 1.5         | 63         | 48.0       | 55             | 49.9       |

Table 7.1: List of events survived from the  $p_t$  cut.

the determination of the thrust axis and  $p_t$  is affected. The fact that  $b$ -flavoured hadron decays lead to high  $p_t$  leptons in semi-leptonic decays is just a phase space phenomenon. A massive  $b$  quark/hadron of  $\approx 5$  GeV leads to an average  $p_t \approx 1.5$  GeV/c for the charged lepton. Fig. 7.8 shows the transverse momentum distribution of muon candidates. Points with error bars show the data and the histograms show the results from the Monte Carlo simulation. The shaded area indicates the fraction of  $b \rightarrow \mu$ , and the cross-hatched and hatched areas correspond to  $b \rightarrow c \rightarrow \mu$  and the charm contribution ( $c \rightarrow \mu$ ), respectively. The open area represents the background contribution from muons for charged  $\pi$  and  $K$  decays and from punchthrough particles. Table 7.1 gives the prompt muon ratio with respect to the total muon candidates which is shown in Fig. 7.9.

A prompt lepton decayed from a heavy quark generally tends to be isolated because of the relatively large  $Q$ -value compared with the masses of decay products. It can be seen clearly from Fig. 7.9 that a higher  $p_t$  cut yields a purer  $b \rightarrow \mu$  event sample but reduces the number of events. In order to tag the  $b\bar{b}$  pair production efficiently, the following criterion is adopted:

- The transverse momentum of a muon candidate is required to be greater than 1.3 GeV.

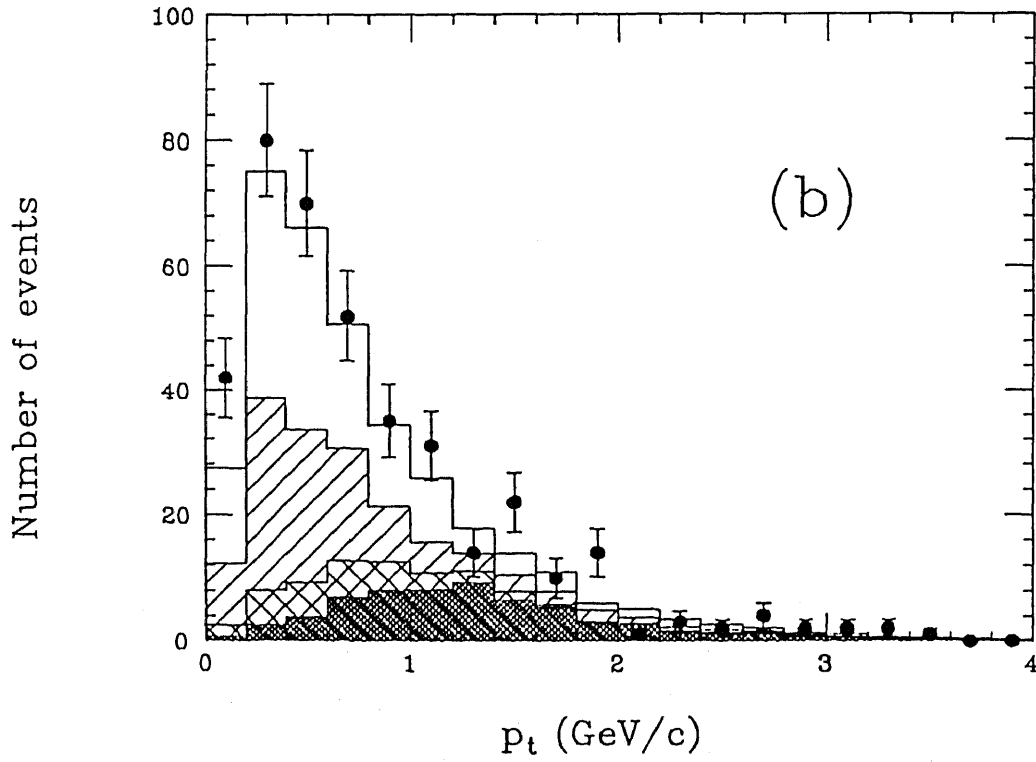
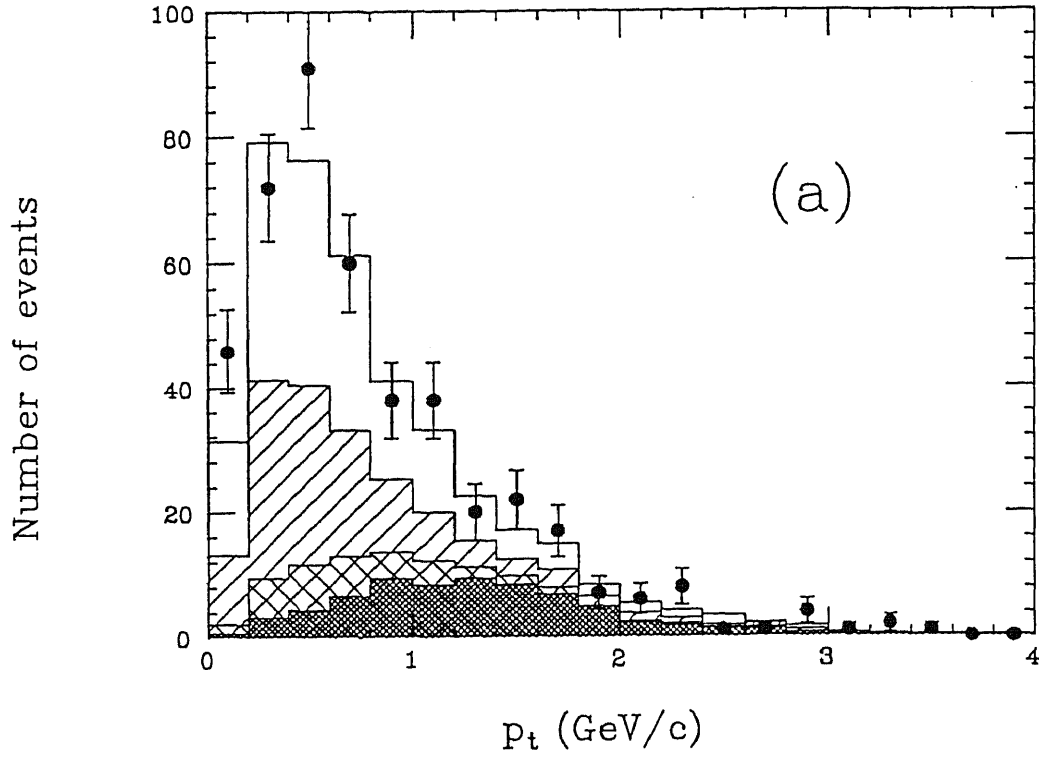


Figure 7.8: Transverse momentum of the muon candidates; (a) with respect to the thrust axis and (b) with respect to the combined axis. Shaded, cross-hatched, hatched and open histograms correspond to Monte Carlo calculations for  $b \rightarrow \mu$ ,  $b \rightarrow c \rightarrow \mu$ ,  $c \rightarrow \mu$  and decay and punchthrough backgrounds, respectively.

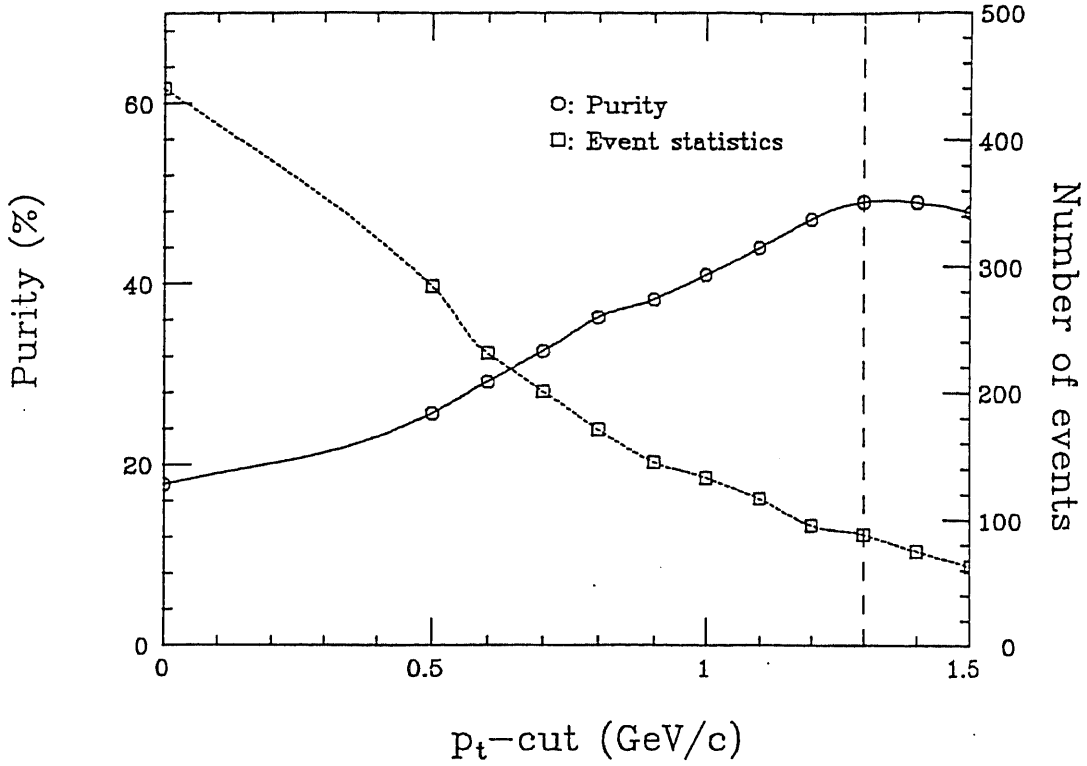


Figure 7.9:  $p_t$ -cut dependence of the prompt muon ratio and the track acceptance.

Fig. 7.10 shows the angular distribution of the represented  $b$ -quark by using the thrust axis. Background contaminations are estimated by Monte Carlo calculations and subtracted bin by bin. Points with error bars show the data and the histograms show the results from the Monte Carlo simulation. The shaded area indicates the fraction of  $b \rightarrow \mu$ , and the cross-hatched and hatched areas correspond to  $b \rightarrow c \rightarrow \mu$  and the charm contribution ( $c \rightarrow \mu$ ), respectively.

### 7.3 Differential Cross Section

The obtained angular distribution for  $e^+e^- \rightarrow b\bar{b}$  includes the effects of kinematical acceptance and radiative processes such as soft photon and soft gluon emission. They depend on the cut conditions of event selection, e.g. the fiducial volume cut and thrust value cut. In order to compare our results with the prediction of the electroweak theory or results of other experiments, the correction due to these effects must be evaluated.

The experimental values of the lowest order differential cross section for  $e^+e^-$

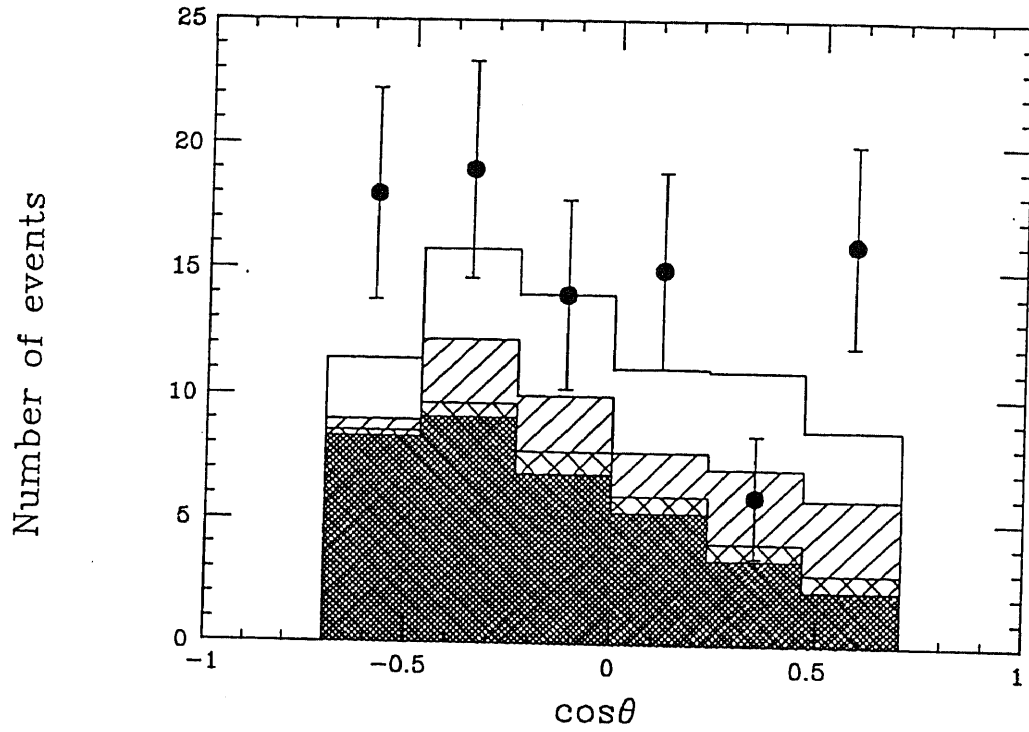


Figure 7.10: Angular distribution of the thrust axis. Shaded, cross-hatched, hatched and open histograms correspond to Monte Carlo calculations for  $b \rightarrow \mu$ ,  $b \rightarrow c \rightarrow \mu$ ,  $c \rightarrow \mu$  and decay and punchthrough backgrounds, respectively.

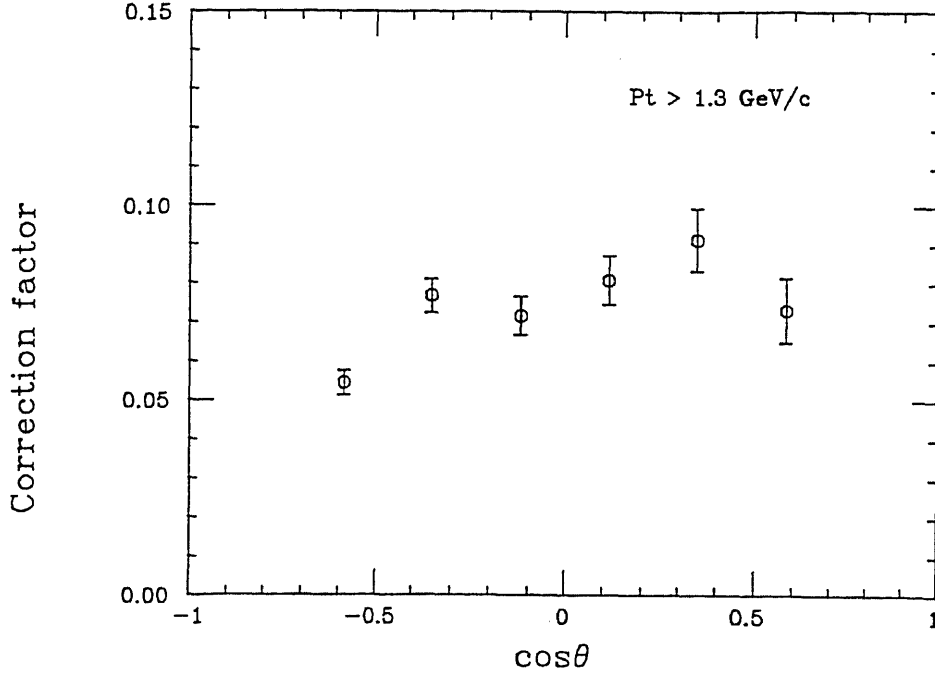


Figure 7.11: Correction factor of the differential cross section for  $e^+e^- \rightarrow b\bar{b}$ .

can be evaluated by using the following formula:

$$\left(\frac{d\sigma}{d\Omega}\right)_i = \left(\frac{1}{\epsilon Br(1+\delta)}\right)_i \frac{N_i^{obs}}{2\pi\Delta \cos \theta \cdot \mathcal{L}} \quad (7.6)$$

where the suffix  $i$  means the  $i$ -th angular bin,  $\epsilon$  is the detection efficiency,  $Br$  is the branching ratio of the semi-leptonic decay,  $\delta$  is the radiative correction factor including both photons and gluons,  $N_i^{obs}$  is the number of observed events and  $\mathcal{L}$  is the integrated luminosity.

The correction factor  $\epsilon Br(1+\delta)$  is estimated by using a Monte Carlo simulation with the effect of initial state radiation calculated by Fujimoto et al. The result can be expressed as:

$$[\epsilon Br(1+\delta)]_i = \frac{\left(\frac{d\sigma}{d\Omega}\right)_i^{MC}}{\left(\frac{d\sigma}{d\Omega}\right)_i^{GWS}} \quad (7.7)$$

where MC means the result of the Monte Carlo simulation and GWS means the lowest order prediction of the electroweak theory. Fig. 7.11 shows the behavior of the correction factor as a function of  $\cos \theta$ .

The correction factor has a slight angular dependence which is due to the higher order correction such as the radiative correction or gluon emission and the

| $\cos \theta$      | $N_{obs}$ | $\varepsilon(1 + \delta)$ | $d\sigma/d\Omega_{data}$ | $d\sigma/d\Omega_{EW}$ |
|--------------------|-----------|---------------------------|--------------------------|------------------------|
| $-0.70 \sim -0.58$ | 18        | 0.55                      | $3.06 \pm 0.87$          | 3.01                   |
| $-0.58 \sim -0.35$ | 19        | 0.77                      | $1.80 \pm 0.64$          | 2.23                   |
| $-0.35 \sim 0.00$  | 14        | 0.72                      | $1.08 \pm 0.58$          | 1.60                   |
| $0.00 \sim 0.35$   | 15        | 0.81                      | $1.28 \pm 0.54$          | 1.11                   |
| $0.35 \sim 0.58$   | 6         | 0.91                      | $-0.19 \pm 0.30$         | 0.77                   |
| $0.58 \sim 0.70$   | 16        | 0.73                      | $1.46 \pm 0.61$          | 0.57                   |

Table 7.2: Measured differential cross section for  $e^+e^- \rightarrow b\bar{b}$ .

detection efficiency of the muon detector. They reduce the asymmetry of the  $b$ -quark production process about 8 % for an angular range of  $|\cos \theta| < 0.7$  according to the Monte Carlo calculation.

The differential cross section thus obtained for  $b\bar{b}$ -production is summarized in Table 7.2 and shown in Fig. 7.12.

## 7.4 Results and Errors

### 7.4.1 Fitting procedure

To obtain the forward-backward charge asymmetry for  $b$ -quark pair production, the measured angular distribution is fitted with the following formula:

$$\frac{d\sigma^{measured}}{d\Omega} = \frac{\alpha^2}{4s} R_b \left( 1 + \cos^2 \theta + \frac{8}{3} A_b \cos \theta \right) \quad (7.8)$$

where  $R_b$  and  $A_b$  are free parameters for the  $R$ -ratio and the charge asymmetry, respectively. In this fitting procedure, the most likelihood method is used and the value of the probability  $P$  is defined by

$$P = \prod_i \frac{m_i^{x_i} e^{-m_i}}{x_i!} \quad (7.9)$$

where  $m_i$  is the number of events predicted by the electroweak theory and  $x_i$  is the observed number of events. The suffix  $i$  denotes the  $i$ -th bin in  $\cos \theta$ . The number of expected events  $m_i$  is calculated by

$$m_i = 2\pi \epsilon Br(1 + \delta)|_i \int_{z_i}^{z_i + \Delta z} \frac{d\sigma^{GWS}}{dz} dz \quad (7.10)$$

where  $\epsilon Br(1 + \delta)|_i$  is a correction factor,  $z_i$  is the lower edge of the  $i$ -th bin and  $\Delta z$  is the bin width. The  $R$ -ratio and the forward-backward charge asymmetry of



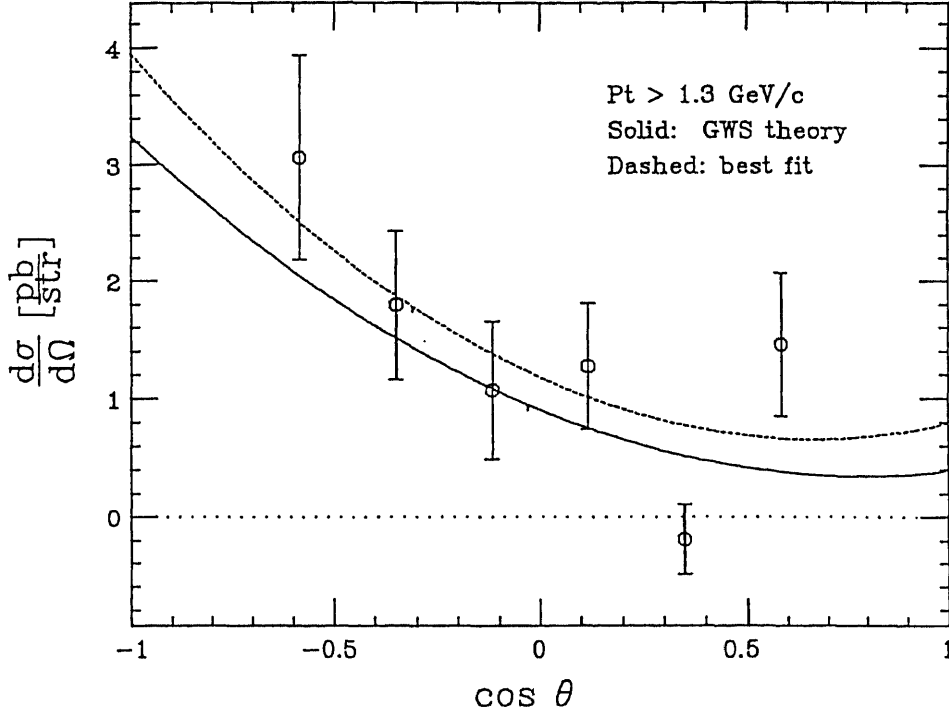


Figure 7.12: Measured differential cross section for  $e^+e^- \rightarrow b\bar{b}$ .

$b$ -quark are determined as follows:

$$R_b = 0.78 \pm 0.14 \quad (7.11)$$

$$A_b = -0.50 \pm 0.18 \quad (7.12)$$

where errors are statistical only.

#### 7.4.2 Systematic errors

The major background source is muons from decays in flight of charged pions and kaons before absorbed by the absorber materials by strong interactions. These muons amount to about 25.5 % of total muon candidates which survived all the cut criteria. The decay probability before a particle has traveled a distance  $l$  is given by

$$P(l) = 1 - \exp\left(\frac{-ml}{p\tau_0}\right) \quad (7.13)$$

where  $m$ ,  $p$  and  $\tau_0$  are the mass, momentum and lifetime, respectively. The pion and kaon decay probabilities in the VENUS detector are calculated to be  $Br(\pi \rightarrow \mu\nu) = 1.0$  and  $Br(K \rightarrow \mu\nu) = 0.64$ , respectively. The uncertainty from decay in flight is negligibly small because the lifetimes of pions and kaons are known precisely.

| Source of uncertainty     | Errors |        |
|---------------------------|--------|--------|
|                           | $R_b$  | $A_b$  |
| Fragmentation             | 0.02   | 0.05   |
| Branching ratio           | 0.04   | 0.04   |
| Charm contribution        | 0.01   | < 0.01 |
| Punch-through probability | 0.01   | 0.01   |
| Luminosity measurements   | 0.03   | 0.01   |
| Correction factor         | 0.01   | 0.04   |
| Cut-dependence of $p_t$   | 0.09   | 0.08   |
| Total (quadratic sum)     | 0.11   | 0.11   |

Table 7.3: Summary of systematic errors.

Punchthrough hadrons passing through absorber materials become a background source although the rate is not so large. The punchthrough probability of a hadron depends mainly on the absorption length of the materials. In order to evaluate the absorption length of the hadron absorber of the VENUS detector, the beam test was carried out in an absorber arrangement very close to the actual VENUS detector by using  $\pi^-$  beams of 3 and 4 GeV/c in the test channel of the 12 GeV proton synchrotron[37]. The results are  $21.2 \pm 0.3$  cm and  $24.2 \pm 0.2$  cm at 3 and 4 GeV/c, respectively. The value 22.3 cm is set for the absorption length of the iron absorber in the detector simulator VMONT without taking into account the momentum dependence. The punchthrough probability of a hadron which survived all the cuts is estimated to be about 7.0 %.

Details of systematic errors are summarized in Table 7.3. The dominant source is the cut-dependence for the muon transverse momentum with respect to the thrust axis.

The branching ratio of semi-muonic decay is varied  $\pm 10\%$  for  $D$  and  $B$  mesons. The uncertainty from the correction factor comes from the Monte Carlo statistics used in the calculation. Cut dependence of the  $b$ -flavour selection is summarized in Table 7.3. The total systematic errors are estimated to be 0.11 for both the  $R$ -ratio and charge asymmetry.

In addition, the artificial asymmetry in the VENUS detector is found to be negligible. Therefore,  $R_b$  and  $A_b$  become

$$R_b = 0.78 \pm 0.18 \quad \text{pred.}(0.58) \quad (7.14)$$

$$A_b = -0.50 \pm 0.21 \quad \text{pred.}(-0.59) \quad (7.15)$$

| $p_t$ (GeV) | $R_b$ | Errors     | $A_b$ | Errors     |
|-------------|-------|------------|-------|------------|
| 1.0         | 0.68  | $\pm 0.12$ | -0.51 | $\pm 0.19$ |
| 1.1         | 0.70  | $\pm 0.12$ | -0.55 | $\pm 0.19$ |
| 1.2         | 0.67  | $\pm 0.13$ | -0.58 | $\pm 0.19$ |
| 1.3         | 0.78  | $\pm 0.14$ | -0.50 | $\pm 0.18$ |
| 1.4         | 0.77  | $\pm 0.15$ | -0.54 | $\pm 0.20$ |
| 1.5         | 0.74  | $\pm 0.16$ | -0.61 | $\pm 0.21$ |

Table 7.4: *List of measured  $R_b$  and  $A_b$  with the various  $p_t$ -cut.*

where errors are quadratically summed. They are consistent with the predictions of the standard electroweak theory.



# Chapter 8

## $B^0$ - $\overline{B}^0$ Oscillations

### 8.1 Compilation of Heavy Quark Asymmetries

A compilation of statistically independent measurements of  $b$ -quark charge asymmetries at PEP, PETRA and TRISTAN[38] is given in Table 8.1 together with the world averages at various center-of-mass energies.  $B^0$ - $\overline{B}^0$  mixing corrections are applied to the  $b$  asymmetry measurements which are necessary for comparison with the Born term predictions of the GWS theory. The latter has been calculated fixing the coupling constants to the Standard Model values and using the mass and width of the  $Z^0$  and the weak mixing angle listed in Table 2.1 (See Chapter 2.) which are consistent with the results of the recent high precision measurements at LEP, SLC and TEVATRON[39].

Only in a few recent experiments,  $B^0$ - $\overline{B}^0$  mixing corrections have been carried out using different assumptions for the size and uncertainty of the corrections. In order to compile all the measurements given in Table 8.2, the same correction for  $B^0$ - $\overline{B}^0$  oscillations is applied based on the result for the mixing parameter of  $\chi_d$  (See Eq. 2.31.) and under the assumption of the  $B_s^0$  mixing parameter  $\chi_s$ , which has not yet been measured independently. An unbiased assumption  $\chi_s = 0.25 \pm 0.25$  and the maximal  $B_s^0$  mixing  $\chi_s = 0.50 \pm 0.25$  is assumed alternatively. The correction factor  $1/(1 - 2\chi)$  (See Eq. 2.30.) ranges from  $1.26 \pm 0.12$  to  $1.38 \pm 0.14$  for the two assumptions on  $\chi_s$ . A still rather large uncertainty in the magnitude of  $B^0$ - $\overline{B}^0$  oscillations introduces an additional error in the  $b$  asymmetry measurements. JADE gives their final corrected results at 35 and 44 GeV without taking into account this uncertainty. The applied mixing corrections are removed in the JADE results given in Table 8.1.

The correction has been applied after combining statistical and systematic errors of the observed asymmetries quadratically. The average results with  $B^0$ - $\overline{B}^0$  mixing corrections at PEP, PETRA, TRISTAN and LEP energies are given in Ta-

| Experiment | $\sqrt{s}$ (GeV) | method | $A_b^{measured}$ (%) | $A_b^{GWS}$ (%) |
|------------|------------------|--------|----------------------|-----------------|
| HRS        | 29.0             | $e$    | $-14.0 \pm 12.0$     | -17.4           |
| MAC        | 29.0             | $\mu$  | $+3.4 \pm 7.8$       | -17.4           |
| TPC        | 29.0             | $e$    | $-36.0 \pm 35.2$     | -17.4           |
| TPC        | 29.0             | $\mu$  | $-15.0 \pm 20.6$     | -17.4           |
| PEP        | 29.0             | -      | $-4.0 \pm 6.1$       | -17.4           |
| CELLO      | 35.0             | $l$    | $-22.2 \pm 8.5$      | -26.0           |
| JADE       | 35.0             | $l$    | $-11.9 \pm 6.5$      | -26.0           |
| MARK-J     | 37.0             | $\mu$  | $0.0 \pm 16.1$       | -29.3           |
| PLUTO      | 34.8             | $\mu$  | $-36.0 \pm 26.2$     | -25.7           |
| TASSO      | 34.8             | $e$    | $-20.0 \pm 11.7$     | -25.7           |
| TASSO      | 34.5             | $\mu$  | $-37.5 \pm 27.5$     | -25.3           |
| TASSO      | 35.0             | jet    | $-14.0 \pm 14.6$     | -26.0           |
| PETRA      | 35.0             | -      | $-16.2 \pm 4.2$      | -26.0           |
| CELLO      | 43.0             | $l$    | $-49.1 \pm 16.8$     | -39.7           |
| JADE       | 44.0             | $l$    | $-24.1 \pm 16.4$     | -41.5           |
| PETRA      | 43.5             | -      | $-36.5 \pm 11.6$     | -40.6           |
| AMY        | 55.2             | $\mu$  | $-72 \pm 31$         | -57.4           |
| TOPAZ      | 58.3             | $\mu$  | $-71 \pm 35$         | -58.8           |
| VENUS      | 58.4             | $\mu$  | $-50 \pm 21$         | -58.9           |
| TRISTAN    | 57.6             | -      | $-60 \pm 16$         | -58.7           |
| ALEPH      | 91.1             | $\mu$  | $12.6 \pm 3.0$       | 10.5            |
| DELPHI     | 91.1             | $\mu$  | $11.1 \pm 4.5$       | 10.5            |
| L3         | 91.1             | $\mu$  | $13.3 \pm 9.9$       | 10.5            |
| OPAL       | 91.1             | $\mu$  | $7.2 \pm 4.3$        | 10.5            |
| LEP        | 91.1             | -      | $11.0 \pm 2.1$       | 10.5            |

Table 8.1: Measurements of the  $b$ -quark asymmetry at PEP, PETRA, TRISTAN and LEP.

| Experiment | $\sqrt{s}$ (GeV) | $A_b$ (%)                          |                                | $A_b^{GWS}$ (%) |
|------------|------------------|------------------------------------|--------------------------------|-----------------|
|            |                  | unbiased $B^0-\overline{B}^0$ osc. | max. $B^0-\overline{B}^0$ osc. |                 |
| PEP        | 29.0             | $-5.0 \pm 7.7$                     | $-5.5 \pm 8.4$                 | -17.4           |
| PETRA      | 35.0             | $-19.8 \pm 5.2$                    | $-21.3 \pm 5.6$                | -26.0           |
| PETRA      | 43.5             | $-45.9 \pm 14.9$                   | $-50.0 \pm 16.3$               | -40.6           |
| TRISTAN    | 57.6             | $-76 \pm 20$                       | $-83 \pm 22$                   | -58.7           |
| LEP        | 91.1             | $13.9 \pm 3.0$                     | $15.2 \pm 3.3$                 | 10.5            |

Table 8.2: Measurements of the  $b$ -quark asymmetry at PEP, PETRA, TRISTAN and LEP with mixing correction.

ble 8.3. The MAC result with positive sign is not expected in the Standard Model even with  $B^0-\overline{B}^0$  oscillations. This measurement cannot be corrected consistently for  $B^0-\overline{B}^0$  mixing since the correction would increase the discrepancy against the prediction of the GWS theory with which the measurement should be compared. Mixing corrections to the PEP average result was obtained after the average asymmetry was calculated including the MAC result. The TASSO measurement using the lifetime tag and jet charge methods is not influenced by  $B^0-\overline{B}^0$  mixing. The AMY measurement corrected exceeds by far the limit in the magnitude of the charge asymmetry ( $\pm 75$  %) where the differential cross section starts to be negative in a part of the angular range. Fig. 8.1 shows the results for the  $b$  asymmetries without  $B^0-\overline{B}^0$  mixing correction and with unbiased  $B^0-\overline{B}^0$  mixing correction as a function of the center-of-mass energy. The solid line represents the prediction of the GWS theory.

## 8.2 Average Mixing Parameter

The measurements of  $b$ -quark charge asymmetry are sensitive for the determination of the averaged  $B^0-\overline{B}^0$  mixing parameter  $\chi$ . Combining our results with those of the other experiments listed in Table 8.1, the following weighted-mean value was obtained by using Eq. 2.30 for the averaged mixing parameter:

$$\chi = 0.105 \pm 0.051 \quad (8.1)$$

with lower limits of  $\chi > 0.022$  and  $\chi > 0.006$  at 90 % and 95 % C.L., respectively.

In order to extract information on  $B_d^0$  and  $B_s^0$  mixings, the present result was combined with the previous measurements of the mixing parameters  $\chi_d$  and  $\chi$  at

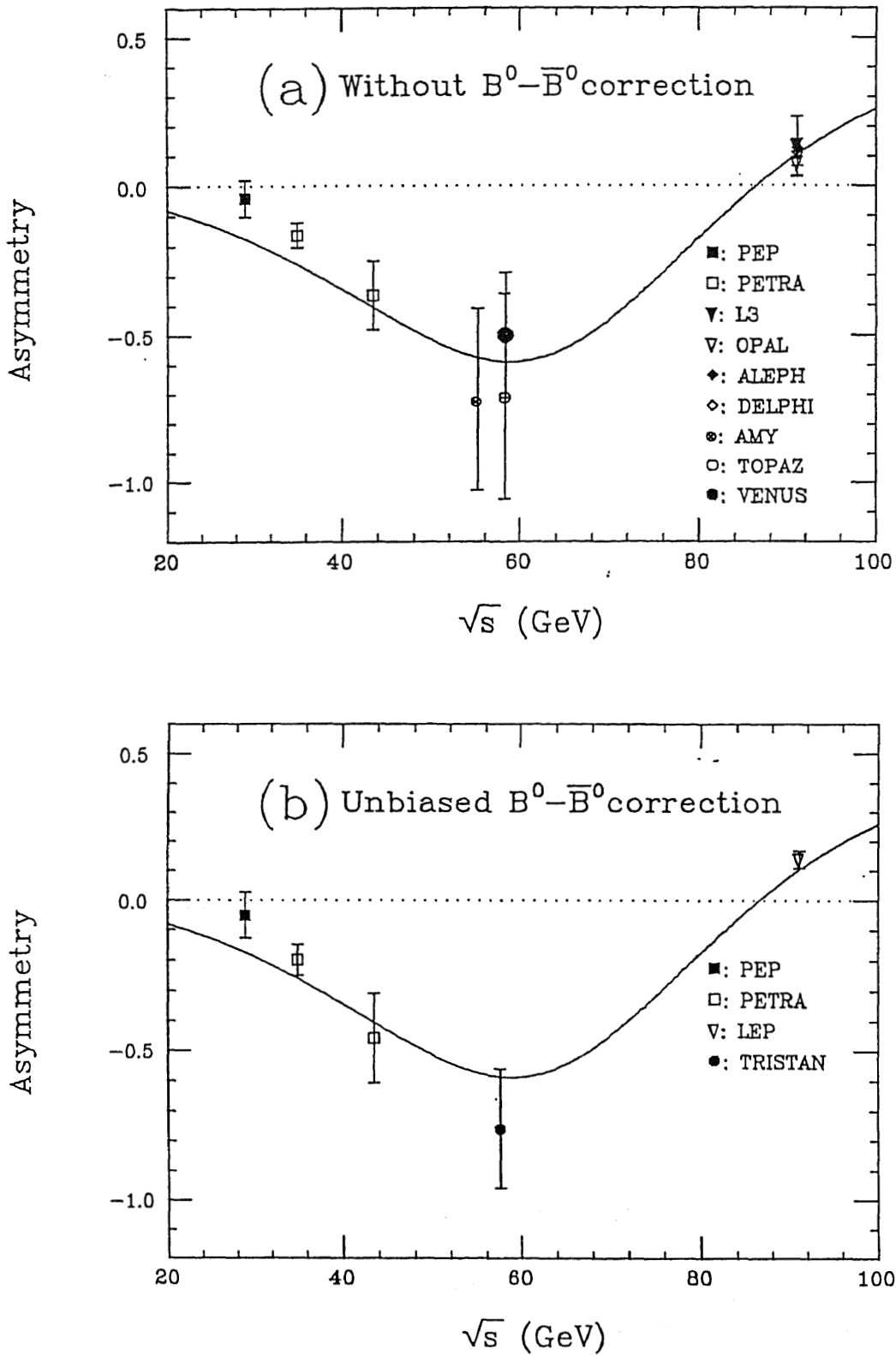


Figure 8.1: Measurements of the  $b$ -quark asymmetry at PEP, PETRA, TRISTAN and LEP; (a) without  $B^0-\bar{B}^0$  mixing and (b) with  $B^0-\bar{B}^0$  mixing.



| Experiment            | Mixing parameter              |
|-----------------------|-------------------------------|
| ARGUS                 | $\chi_d = 0.174 \pm 0.041$    |
| CLEO                  | $\chi_d = 0.154 \pm 0.056$    |
| UA1                   | $\chi = 0.121 \pm 0.047$      |
| MAC                   | $\chi = 0.21^{+0.29}_{-0.15}$ |
| MARK II               | $\chi = 0.17^{+0.15}_{-0.08}$ |
| Asymmetry measurement | $\chi = 0.105 \pm 0.051$      |

Table 8.3: *Mixing parameters of the  $B^0$ - $\overline{B}^0$  oscillation.*

$e^+e^-$  and  $\overline{p}p$  colliders. The latter results are based upon measurements of like-sign dilepton production[40,41,42]. The least  $\chi^2$  fit was performed with the following equation:

$$X^2 = \sum_{i=ARGUS,CLEO} \left( \frac{\chi_d - \chi_d^i}{\Delta\chi_d^i} \right)^2 + \left( \frac{f_d\chi_d + f_s\chi_s - \chi^{average}}{\Delta\chi^{average}} \right)^2 \quad (8.2)$$

where ‘ $X^2$ ’ is used in place of the  $\chi^2$  value to avoid a confusion with the mixing parameter  $\chi$ . The first term was summed for the ARGUS and CLEO data. The second term was summed for the UA1, MAC and MARK II data and the weighted-mean value, which are listed in Table 8.3.

The most probable values for  $\chi_d$  and  $\chi_s$  from the combined measurements are fitted to be

$$\chi_d = 0.167 \pm 0.033 \quad (8.3)$$

$$\chi_s = 0.41 \pm 0.27 \quad (8.4)$$

$$\chi = f_d\chi_d + f_s\chi_s = 0.12 \pm 0.03 \quad (8.5)$$

where  $f_d = 0.43$  and  $f_s = 0.13$ .  $\chi_d + 0.3\chi_s = 0.159$ , namely a correlation coefficient of 0.159 between  $\chi_d$  and  $\chi_s$ . Fig. 8.2 shows the 69 % and 80 % C.L. contours in the  $\chi_s - \chi_d$  plane allowed by the various measurements given in Table 8.3. The results for the parameter  $\chi_s$  give the experimental confirmation of non-zero  $B_s^0$  mixing. The zero  $B_s^0$  mixing could be excluded with 1.5 standard deviations.

The present asymmetry measurement by the VENUS detector has about 2 ~ 4 % contribution to determine the center value and its error for the  $B_s^0$  mixing parameter  $\chi_s$ . It is required to accumulate more event statistics for the precise  $\chi_s$  determination.

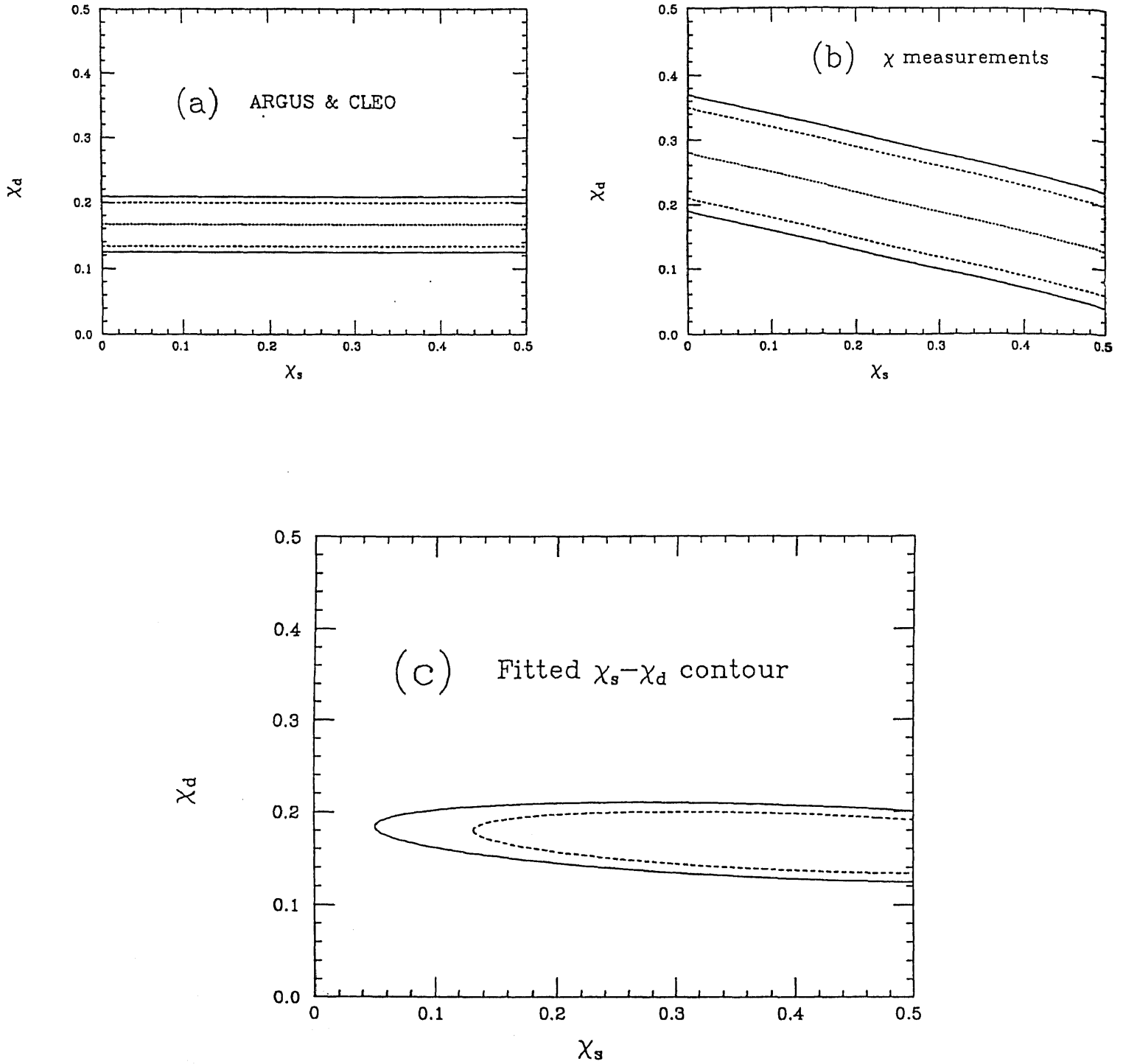


Figure 8.2: Mixing parameters in the  $\chi_s - \chi_d$  plane. Dotted curves are the central value and the dashed and solid curves represent the 69 % and 80 % C.L. contours, respectively.

# Chapter 9

## Conclusion

The forward-backward charge asymmetry and  $R$ -ratio of  $b$ -quark pair production have been measured at the center-of-mass energies between 54 and 64 GeV. The total integrated luminosity is  $60.8 \text{ pb}^{-1}$  and the average center-of-mass energy is 58.4 GeV. In the analysis,  $b$ -quark pair production events were tagged by using muons from semi-leptonic decay processes and two-jet selection was applied by using the thrust cut:  $T > 0.85$ . The obtained  $R$ -ratio and asymmetry are

$$R_b = 0.78 \pm 0.14(\text{stat.}) \pm 0.11(\text{sys.}) \quad (9.1)$$

$$A_b = -0.50 \pm 0.18(\text{stat.}) \pm 0.11(\text{sys.}) \quad (9.2)$$

These results are consistent with the Standard Model predictions, namely 0.58 for the  $R$ -ratio and  $-0.59$  for the charge asymmetry with the assignment of the iso-spin doublet of the third quark generation.

Combining our result with those of other experiments, the world averages of the mixing parameters  $\chi_d$ ,  $\chi_s$  and  $\chi$  for the  $B^0$ - $\overline{B}^0$  oscillations are obtained as follows:

$$\chi_d = 0.167 \pm 0.033 \quad (9.3)$$

$$\chi_s = 0.41 \pm 0.27 \quad (9.4)$$

$$\chi = f_d \chi_d + f_s \chi_s = 0.12 \pm 0.03 \quad (9.5)$$

where  $f_d = 0.43$  and  $f_s = 0.13$ . Thus  $\chi_d + 0.3\chi_s = 0.159$ , namely a correlation coefficient is 0.159 between  $\chi_d$  and  $\chi_s$ . The result for the parameter  $\chi_s$  gives the experimental confirmation of non-zero  $B_s^0$  mixing. The zero  $B_s^0$  mixing could be excluded with 1.5 standard deviations. The measured asymmetry is corrected by using the above results to be  $A_b = -0.66 \pm 0.28$  where the statistical and systematic errors are summed quadratically. This result is still consistent with the prediction of the standard electroweak theory.



# Bibliography

- [1] R.Brandelik et al., Phys. Rev. Lett. **B97**(1980) 453.
- [2] J. Schwinger, “*Selected Papers on Quantum Electrodynamics*”, Dover Publication, New York, 1958.
- [3] L3 Collab., B.Adeva et al., Phys. Lett. **237B**(1990) 136.  
ALEPH Collab., D.Decamp et al., Phys. Lett. **235B**(1990) 399.  
OPAL Collab., M.Akrawy et al., Phys. Lett. **231B**(1989) 530.  
DELPHI Collab., P.Aarnio et al., Phys. Lett. **240B**(1990) 271.
- [4] M.Kobayashi and K.Maskawa, Progr. Theor. Phys. **49**(1973) 652.
- [5] S. L. Glashow, Nucl. Phys. **22** (1961) 579;  
S. Weinberg, Phys. Rev. Lett. **19** (1967) 1264;  
A.Salam and J.C.Ward, Phys. Lett. **13**(1964)168;  
A. Salam, in *Elementary Particle Theory*, edited by N. Svartholm (Almqvist and Wiksell, Stockholm, 1969), p.367.
- [6] J.E.Augustin et al., Phys. Rev. Lett. **33**(1974) 1406.
- [7] M.L.Pearl et al., Phys. Rev. Lett. **35**(1975) 1489.
- [8] S.Herb et al., Phys. Rev. Lett. **39**(1977) 252.
- [9] G.Flügge, L.M.Lederman, in “*Proc. of the 19th Int. Conf. on High Energy Phys.*”, Tokyo(1978).
- [10] D.P.Barber et al., Phys. Rev. Lett. **46**(1981) 1663.
- [11] ARGUS Collab., H.Albrecht et al., Phys. Lett. **B192**(1987) 245.
- [12] I.I.Bigi, Phys. Lett. **155**(1985) 125.
- [13] ARGUS Collab., H.Albrecht et al., Phys. Lett. **192B**(1987) 245.  
M.Danilov, ARGUS Collab., Proc. 1989 Int. Symposium on Lepton and Photon Interactions at High Energies, Stanford (1989).

- [14] CLEO Collab., M.Artuso et al., Phys. Rev. Lett. **62**(1989) 2233.
- [15] TRISTAN Project Group, 'TRISTAN Electron-Positron Colliding Project', KEK report 86-14(1986).
- [16] VENUS Collaboration, KEK Report TRISTAN-EXP-001(1983).
- [17] IEEE Standard FASTBUS Modular High-Speed Data Acquisition and Control System, ANSI/IEEE Std, 960-1986
- [18] TKO Specification, KEK Report 85-10(1985);  
T.K.Ohsaka *et al.*, IEEE Trans., Nucl. Sci. **33**(1986)98;  
H.Kurashige *et al.*, *ibid.* **35**(1988)357.
- [19] R.Arai et al., Nucl. Instr. Meth. **A217**(1983)181.
- [20] T.Sumiyoshi et al., Nucl. Instr. and Meth. **A271**(1988)432;  
K.Ogawa et al., Nucl. Instr. and Meth. **A243**(1986)58.
- [21] Y. Fukushima et al., IEEE Trans. Nucl. Sci. **36**(1989) 670.
- [22] Y.Asano et al., Nucl. Instr. and Meth. **A254**(1987) 35; Nucl. Instr. and Meth. **A259**(1987) 430; Nucl. Instr. and Meth. **A259**(1987) 438.
- [23] Y.Asano et al., Jpn. J. Appl. Phys. Vol.28, No.10(1989) 1981-1988.
- [24] Y. Hemmi et al., Nucl. Instr. and Meth. **A281**(1989) 462.
- [25] Y.Hemmi et al., Jpn. J. Appl. Phys. **26**(1987)982.
- [26] H.Saito et al., Nucl. Instr. and Meth. **A270**(1988)319.
- [27] K.Amako et al., Nucl. Instr. and Meth. **A272**(1988)687.
- [28] Y. Nakagawa et al., Jpn. J. Appl. Phys. **25**(1986) 1049.
- [29] W. R. Nelson et al., SLAC-265, December 1985.
- [30] S. Brandt and H. D. Dahmen, Z. Phys. **C1** (1979) 61.
- [31] T. Sjöstrand and M. Bengtsson, Comput. Phys. Commun. **43** (1987) 367.
- [32] K.Amako et al., VENUS Offline Note 002(1987).
- [33] J.Fujimoto et al., Prog. Theo. Phys. Supplement No.100, 1990.
- [34] Particle Data Group, "*Review of Particle Properties*", Phys. Lett. **B204**(1988) 1.

- [35] R.M.Sternheimer, Phys. Rev. **177**(1980) 485.
- [36] Y.Asano et al., Nucl. Instr. and Meth. **A259**(1987) 430.
- [37] Y.Asano et al., VENUS Note 168(1987).
- [38] H.Kroha, MPI-PAE/Exp.El. 227 July 1990.  
AMY Collab., H.Sagawa et al., Phys. Rev. Lett. **63**(1989) 2341.  
JADE Collab., W.Bartel et al., Phys. Lett. **146B**(1984) 437.  
HRS Collab., C.R.Ng et al., ANL-HEP-PR-88-11, Nov. 1988.  
MAC Collab., H.R.Band et al., Phys. Lett. **218B**(1989) 369.  
TPC Collab., H.Aihara et al., Z. Phys. **C27**(1985) 39.  
TPC Collab., H.Aihara et al., Phys. Rev. **D31**(1985) 2719.  
CELLO Collab., H.J.Behrend et al., DESY 89-125, Sept. 1989.  
JADE Collab., E.Elsen et al., Z. Phys. **C46**(1990) 349.  
MARK-J Collab., see compilation in S.L.Wu, Proc. 1987 Int. Symposium  
on Lepton and Photon Interactions at High Energies, Hamburg, Nucl. Phys.  
**B**(Proc. Suppl.)**3**(1988) 39.  
C.Maxeiner, PLUTO Collab., Ph.D. thesis, DESY PLUTO-85-03, March  
1985.  
TASSO Collab., M.Althoff et al., Z. Phys. **C22**(1984) 219.  
P.Rehders, TASSO Collab., Ph.D. thesis, DESY F1-89-02, July 1989.  
J.M.Pawlak, TASSO Collab., Ph.D. thesis, DESY F1-88-01, Sept. 1988.
- [39] CDF Collab., F.Abe et al., Phys. Rev. Lett. **63**(1989) 720.  
MARK II Collab., G.S.Abrams et al., Phys. Rev. Lett. **63**(1989) 724.  
ALEPH Collab., D.Decamp et al., Phys. Lett. **231**(1989) 519.  
L3 Collab., B.Adeva et al., Phys. Lett. **231**(1989) 509.  
DELPHI Collab., P.Aarnio et al., Phys. Lett. **231**(1989)539.  
OPAL Collab., M.Z.Akrang et al., Phys. Lett. **231**(1989)530.
- [40] UA1 Collab., C.Albajar et al, Phys. Lett. **186B**(1987) 247.
- [41] MAC Collab., H.R.Band et al, Phys. Lett. **200B**(1988) 221.
- [42] MARK II Collab., A.J.Weir et al, Phys. Lett. **240B**(1990) 289.